ALMA MATER STUDIORUM
UNIVERSITÀ DI BOLOGNA

DOTTORATO DI RICERCA IN

ONCOLOGIA, EMATOLOGIA E PATOLOGIA

Ciclo XXXVIII

Settore Concorsuale: 06/D3 – MALATTIE DEL SANGUE, ONCOLOGIA E REUMATOLOGIA

Settore Scientifico Disciplinare: MED/15 – MALATTIE DEL SANGUE

CAR-T CELL BIOLOGY IN HEMATOLOGIC MALIGNANCIES: CAR$^+$ EXTRACELLULAR VESICLES AS PREDICTIVE BIOMARKERS OF ICANS

Presentata da: Francesco De Felice

Coordinatore Dottorato
Manuela Ferracin

Supervisore
Paolo Garagnani

Co-supervisori
Francesca Bonifazi
Gianluca Storci

Esame finale anno 2026

TABLE OF CONTENTS

ABSTRACT

Predicting immune effector cell-associated neurotoxicity syndrome (ICANS) in patients receiving CAR-T cell therapy remains an unmet challenge. This complication, traditionally attributed to CAR-T cell activation, typically emerges several days after infusion, when circulating CAR-T cells are scarcely detectable and specific biomarkers of their in vivo activity are lacking. CAR^+ extracellular vesicle (CAR^+EV) release was assessed in human CD19.CAR-T cells cocultured with $CD19^+$ target cells. A prospective cohort of 100 patients with B-cell lymphoma infused with approved CD19.CAR-T cell products was assessed for plasma CAR^+EVs as biomarkers of in vivo CD19.CAR-T cell activation. Human induced pluripotent stem cell-derived (iPSC-derived) neural cells were used as a model for CAR^+EV-induced neurotoxicity. In vitro, CAR^+EV release occurred within one hour of target engagement. In patients, CAR^+EVs became detectable in plasma as early as one hour after infusion. A CAR^+EV concentration exceeding 132.8 EVs/µL at hour +1 and 224.5 EVs/µL at day +1 accurately predicted the onset of ICANS approximately four days in advance, with superior sensitivity and specificity compared to currently available predictive parameters. Moreover, exposure of iPSC-derived neural cells to CAR^+EVs induced the release of neuron-specific Enolase positive ($ENO2^+$) nanoparticles, which were also elevated in the plasma of patients who developed ICANS. Collectively, these data identify plasma CAR^+EVs as immediate readout of CD19.CAR-T cell activation, robust early predictors of neurotoxicity, and potential mediators of ICANS pathogenesis.

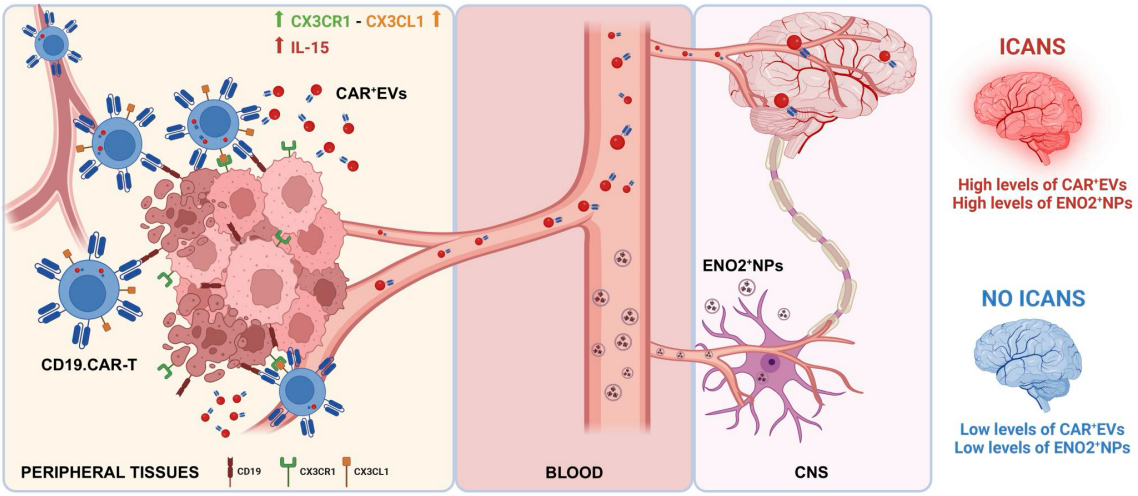

INTRODUCTION

“Adoptive cell transfer” (ACT) is a term first used to describe the infusion of lymphocytes to investigate rejection of organ allografts and to treat tumors. The first successful clinical applications of adoptive cell transfer in the 1980s were based on the use of autologous tumor-infiltrating lymphocytes in patients with metastatic melanoma and allogeneic donor lymphocyte infusions in patients with relapsed leukemia after allogeneic stem cell transplantation. During the last decades, by applying modern ex vivo culture, and recently also in vivo techniques, together with advanced cellular engineering approaches to adoptive T-cell transfer, three forms of ACT are being developed for cancer therapy: tumor-infiltrating lymphocytes (TILs), T-cell receptor (TCR) T-cells, and chimeric antigen receptor (CAR) -T cells.

CAR-T cell therapy

Genetically engineered T-cells represent a transformative class of therapeutics, offering the potential for curative approaches in patients with cancer. Chimeric antigen receptors (CARs) are synthetic constructs that reprogram lymphocyte specificity and effector function. By targeting defined antigens. - such as CD19 - CAR-T cells have demonstrated unprecedented clinical efficacy across several hematologic malignancies. Engineered T-cells hold theoretical applicability across a broad spectrum of cancers, provided that future advances enable the identification of optimal tumor-associated antigens, the circumvention of hostile tumor microenvironments, the mitigation of toxicities, and the prevention of therapeutic failure. A deeper understanding of the biological mechanisms governing CAR-T cell dynamics would enable the selection of the most functionally potent T-cell subsets, the optimization of cell manufacturing processes, and the identification of patients most likely to derive durable benefit from CAR-T cell therapy. Furthermore, elucidating the underlying principles of CAR-T cell biology could broaden their therapeutic landscape to encompass emerging frontiers such as autoimmune and infectious diseases.

CAR-T cells: design and generations

Chimeric antigen receptors are synthetic transmembrane proteins expressed on the surface of immune effector cells that are genetically reprogrammed ex vivo - or, more recently, directly in vivo - to target specific antigens (June et al. 2018). Structurally, CARs consist of distinct functional domains: (1) an extracellular antigen-recognition domain, typically composed of a single-chain variable fragment (scFv) derived from an antibody, which confers high-affinity binding to specific antigens; (2) a transmembrane region that anchors the receptor and critically influences CAR stability, conformation, and antigen-binding efficacy; and (3) an intracellular signaling module that integrates activation and costimulatory signals to orchestrate T-cell effector functions. The CD3ζ chain derived from the T-cell receptor complex constitutes the fundamental activation motif, whereas additional costimulatory domains - such as CD28, 4-1BB (CD137), ICOS, or OX40 (CD134) - are incorporated to enhance persistence, proliferation, and cytokine production (**Figure 1**; Sadelain et al. 2017). These design refinements led to the development of second- and third-generation CARs, which contain one or two costimulatory motifs, respectively, and form the backbone of all currently approved CAR-T products (e.g., axicabtagene ciloleucel [axi-cel] and brexucabtagene autoleucel [brexu-cel], CD28-based; tisagenlecleucel [tisa-cel] and lisocabtagene maraleucel [liso-cel], 4-1BB-based). More recently, fourth-generation CAR-T cells, also termed “T-cells redirected for universal cytokine-mediated killing (TRUCKs)”, have been engineered to secrete immunomodulatory cytokines, ligands, or chemokines upon antigen engagement, thereby counteracting the immunosuppressive tumor microenvironment. Fifth- and next-generation CARs (**Figure 2**) integrate additional molecular innovations - such as tunable or logic-gated signaling domains, switch-on/off safety circuits, metabolic rewiring modules, and synthetic cytokine receptor elements (e.g., IL-2Rβ/STAT3- or IL-7Rα-based) to enhance function, persistence, and safety (Wang et al. 2025). The use of antibody-derived scFv domains allows antigen recognition in a manner independent of human leukocyte antigen (HLA) restriction, distinguishing CAR-T cells from T-cell receptor-engineered T cells and broadening their applicability across diverse patient populations. Collectively, these progressive refinements in CAR design underscore a rapidly evolving field in which structure-function

optimization continues to expand the therapeutic potential of CAR-T cells across both malignant and non-malignant diseases.

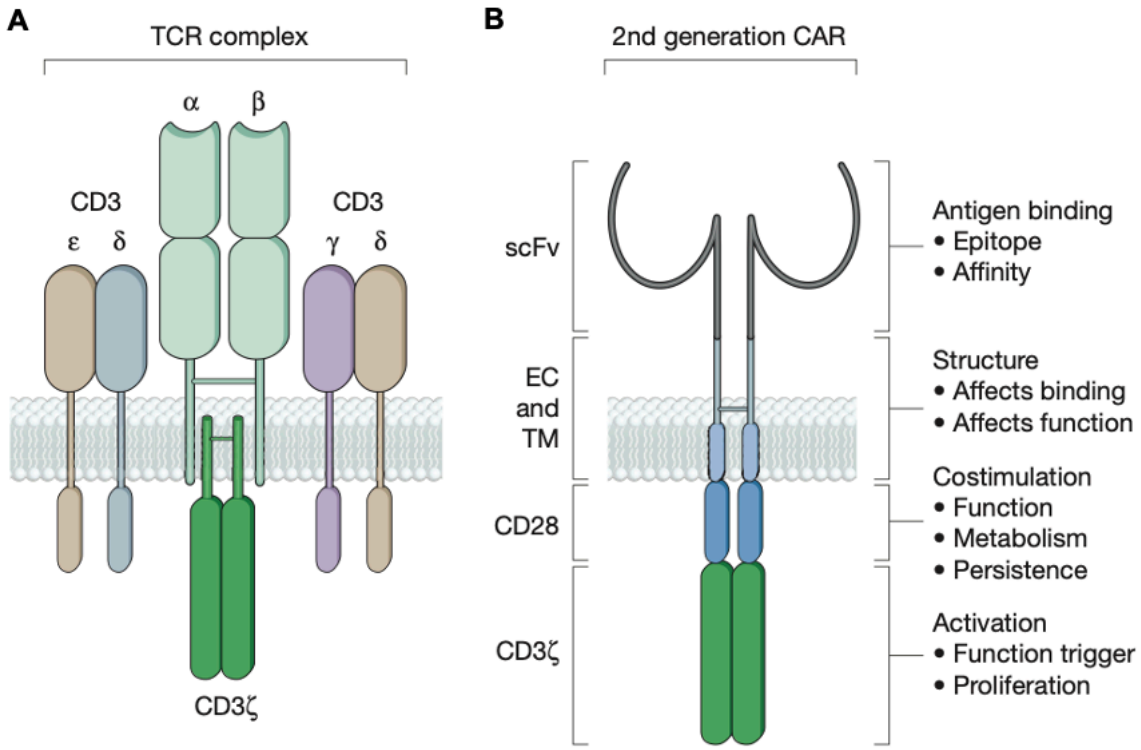

Figure 1. Receptors for antigen. *(**A**) T-cell receptor (TCR). Physiological antigen recognition is mediated by the TCR-CD3 complex, which comprises six independent gene products: the TCR α and β chains, which together bind to HLA-peptide complexes, and the CD3 γ, δ, ε and ζ chains, which initiate T-cell activation. (**B**) Chimeric antigen receptor (CAR). A prototypic second-generation CAR comprises three canonical domains for binding to antigen (unrestricted by HLA), T-cell activation (commonly via the CD3ζ cytoplasmic domain) and co-stimulation (via the CD28 cytoplasmic domain in this example). The hinge and transmembrane domain also contribute to overall CAR function.*

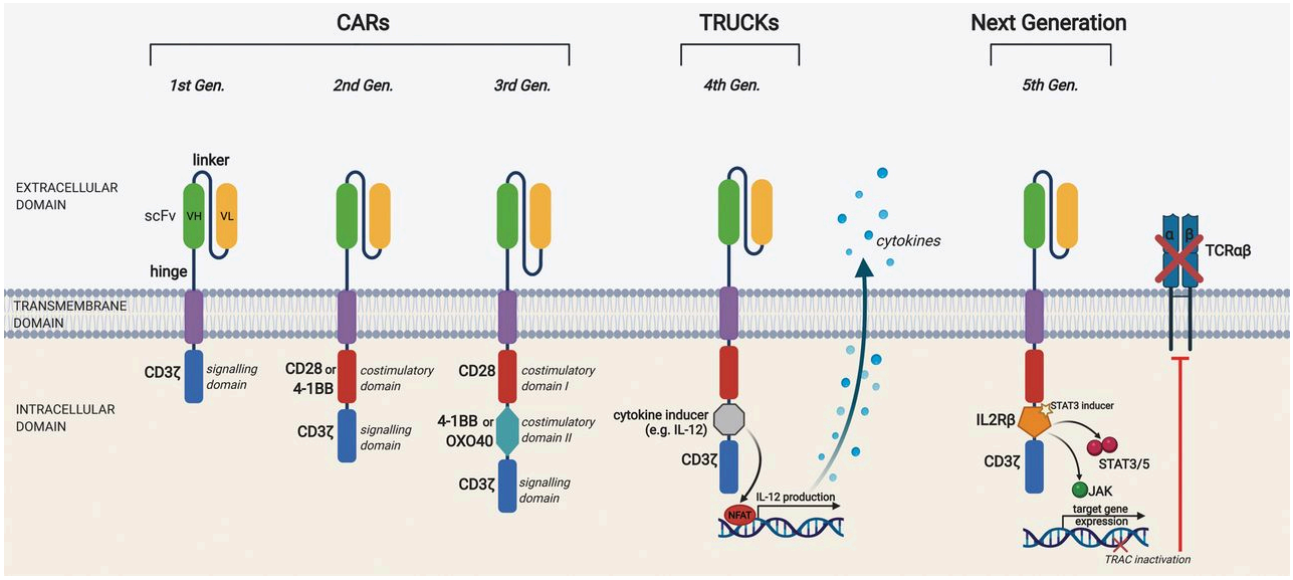

Figure 2. Generations of CAR-T-cell construct designs. *First generation CARs contained only the CD3ζ domain, the initiator of T-cell receptor intracellular signaling. However, these CARs demonstrated limited expansion and in vivo persistence due to lack of a costimulatory signal. Second generation CARs were engineered to contain CD3ζ and a costimulatory signal such as CD28 or 4-1BB, thus conferring enhanced cytotoxicity, expansion, and persistence. Third generation CARs added another costimulatory domain with the first representing CD28 or 4-1BB and the second representing CD28, 4-1BB, or OXO40. These offer superior T-cell expansion and longer persistence through increased cytokine secretion, proliferation speed and survival rate of engrafted T-cells. Fourth generation CARs, also called TRUCKs (T-cells redirected for universal cytokine-mediated killing), possess a cytokine induced domain which activates downstream transcription factor NFAT to induce cytokine production after antigen recognition, thus modulating immune effects. Fifth generation CARs, based on the second generation, require gene editing to inactivate the T-cell receptor alpha constant (TRAC) gene, leading to the removal of the TCR alpha and beta chains and the creation of a truncated cytoplasmic IL-2 receptor β-chain domain with a binding site for STAT3 transcription factor. Antigen activation triggers three synergistic signals through TCR CD3ζ, co-stimulatory CD28, and cytokine JAK-STAT3/5 signaling, which drive T-cell activation and proliferation.*

CAR-T cell journey: from apheresis to infusion

CAR-T cell manufacturing starts from a collection of mononuclear cells (MNCs, although specifically only T lymphocytes will be used for the preparation) from the patient using apheresis. Despite promising work on the development of allogeneic (Del Bufalo et al. 2023) or even random-donor, TCR-edited allogeneic CAR-T cells (Cooper et al. 2018), currently only CAR-T therapies of autologous origin are approved in the European Union. The process proceeds with the manufacturing phase, which builds upon the leukapheresis product and involves isolation of T lymphocytes from peripheral blood mononuclear cells, followed by ex vivo transduction using retroviral or lentiviral vectors encoding the CAR transgene, and subsequent expansion of the modified T-cells to achieve clinically relevant doses (Dias et al. 2024). It is a complex process conducted over approximately 8-12 days in approved cGMP clean room facilities, in a closed or functionally closed system to reduce the risk of product contamination (**Figure 3**)

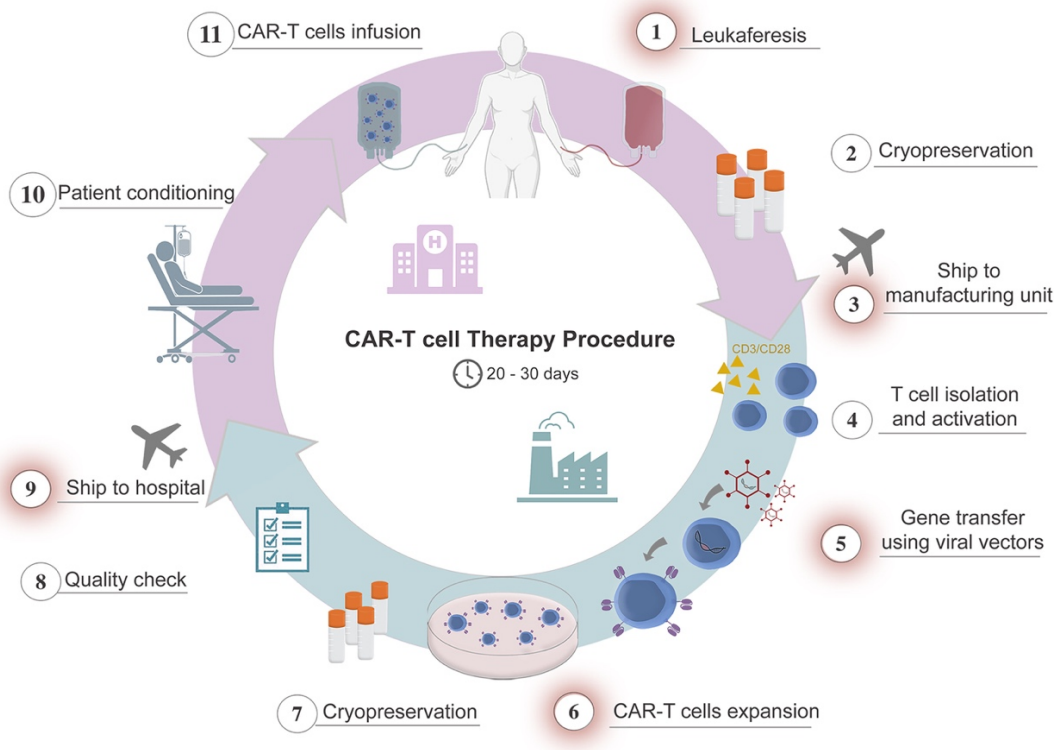

Figure 3. The CAR-T cell journey.

The final step consists of the infusion of CAR-T cells, which is preceded by lymphodepleting chemotherapy aimed at optimizing the in vivo expansion and persistence of the infused cells. Multiple studies have demonstrated that host conditioning plays a pivotal role in shaping the immunologic milieu necessary for CAR-T cell efficacy, by modulating immune-cell subsets, cytokine networks, and the availability of homeostatic cytokines that support T-cell proliferation (Neelapu 2025, **Figure 4**). The combination of fludarabine and cyclophosphamide has emerged as the standard lymphodepletion regimen, after evidence showed that the addition of fludarabine significantly enhances CAR-T expansion and clinical response (Turtle et al. 2016). In most protocols, fludarabine is administered at a standardized dose of 25-30 mg/m² daily for three consecutive days, whereas cyclophosphamide dosing remains more variable, though higher doses have been associated with improved CAR-T expansion and durability of response (Hirayama et al. 2019). Nevertheless, even with optimal lymphodepletion, some patients fail to develop a permissive cytokine milieu, underscoring the biological heterogeneity of host responses to conditioning and its influence on therapeutic outcomes (Hirayama et al. 2019). Typically, the lymphodepleting regimen is administered within seven days prior to CAR-T infusion, followed by a rest period of at least two days to prevent cytotoxic damage to the infused cells. If CAR-T administration is delayed, most clinical protocols allow a 2- to 4-week window before a new conditioning cycle must be repeated. Despite its essential role, lymphodepletion is not without toxicity: pancytopenia, prolonged immunosuppression, and increased infectious risk remain well-recognized adverse effects following CAR-T therapy. Currently, the focus is shifting towards in vivo production of CAR-T cells by targeted viral (or non-viral) transduction, with the aim to substantially reduce costs and production time for autologous therapies. The approach aims at using T cell-targeted viruses, virus-like or lipid nanoparticles packaged with CAR-encoding vector RNA (Rurik et al. 2022). After injection into the patient, the particles are endocytosed by targeted T-cells triggering CAR expression.

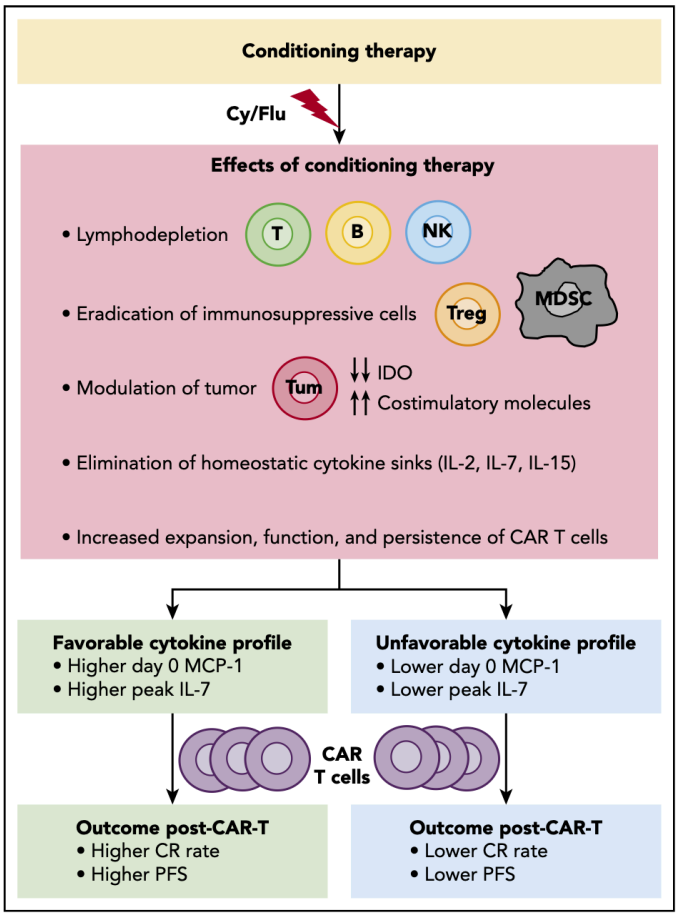

Figure 4. Effects of conditioning therapy and its impact on efficacy of CAR-T cell therapy. *IDO: indoleamine 2,3-dioxygenase; MDSCs: myeloid-derived suppressor cells; Tregs: regulatory T-cells.*

The important issue of the antigen

Compared with conventional anticancer modalities such as chemotherapy, small-molecule inhibitors, or radiotherapy, T-cell based immunotherapies provide unique advantages of antigen specificity, self-amplifying activity, and long-term persistence, features characteristic of living drugs. The functional precision of T-cells is defined by the pairing between their antigen-recognition receptor and its cognate target antigen (Bjorkman et al., 1987; Garcia et al., 1996). Unlike endogenous T-cell receptors (TCRs), which recognize intracellular peptides in an HLA-restricted manner, CARs engage extracellular, nonpolymorphic epitopes, thereby circumventing HLA limitation and enabling universal applicability across patient populations. The attributes defining an optimal CAR target antigen include: (1) extracellular localization and accessibility on the cell surface; (2) uniform expression across malignant cells to avoid immune escape; (3) functional necessity for tumor maintenance to prevent antigen loss variants; (4) expression on malignant stem or progenitor cells to ensure durable eradication; and (5) minimal or absent expression on essential normal tissues to limit on-target, off-tumor toxicity. Tumor-specific antigens (TSAs) arise from somatic mutations generating neoepitopes absent in normal tissues (Schumacher et al., 2015; Schumacher et al., 2019). They confer a low risk of on-target, off-tumor toxicity. However, no nonpolymorphic extracellular TSAs suitable for CAR recognition are currently known, as most neoantigens are peptide fragments presented by polymorphic HLA molecules. Certain oncofetal membrane proteins physiologically downregulated after embryogenesis but aberrantly re-expressed in tumors, such as glypican-3 or carcinoembryonic antigens, may serve as relatively tumor-specific targets (Mackensen et al., 2023; Du et al., 2025), although their occasional re-expression on normal tissues poses a potential safety concern. Lineage-specific and differentiation antigens remain the predominant targets for clinical CAR-T applications. B-lineage markers including CD19, CD20, CD22, and BCMA are exploited in lymphoid malignancies (Sadelain et al., 2017; June et al., 2018): these are considered “ideal” or “permissive” targets because B-cell aplasia is clinically manageable by supportive measures such as immunoglobulin replacement. For myeloid malignancies, CAR-T development has focused on CD33, CD123, and CLEC12A (CLL-1) (Gill et al., 2014; Haubner et al., 2025), although these approaches carry a substantial risk of prolonged cytopenia or marrow aplasia, necessitating hematopoietic rescue. To

mitigate these risks, next-generation CAR designs now incorporate safety switches, transient expression systems, and combinatorial targeting strategies (Loff et al., 2020; Haubner et al., 2025). Because most lineage antigens are nonessential for cell survival, antigen-loss variants and immune escape remain major causes of relapse (Ruella et al., 2023). Concurrent or sequential targeting of multiple antigens (e.g., CD19 + CD22 or BCMA + GPRC5D) has shown promise in limiting escape and improving durability (Marhelava et al., 2025). A further refinement involves polymorphic or heterogeneous lineage-associated antigens, where selective targeting (e.g., κ or λ light chains in B-cell neoplasms) can spare part of the normal compartment, reducing toxicity (Ramos et al., 2016). More recently, dual- or multi-specific CAR-T constructs that require co-expression of two or more antigens for activation have been developed to enhance tumor selectivity and mitigate off-tumor reactivity (Shah et al., 2020; Spiegel et al., 2021). These logic-gated CAR architectures can distinguish malignant cells based on combinatorial antigen signatures, although challenges remain regarding their complexity, manufacturability, and unpredictable cytokine release profiles. Collectively, the evolution of CAR-T cell targeting strategies reflects a dynamic balance between efficacy, safety, and antigen specificity. Continuous refinement of target antigen selection - through integration of multi-antigen logic, transient expression, or adaptive receptor systems - represents a key frontier for the next generation of CAR-based immunotherapies.

The paradigm of the CD19 antigen in B-cell non-Hodgkin lymphomas

Among all the target antigens explored in cellular immunotherapy, CD19 has yielded the most compelling clinical results, representing the cornerstone of CAR-T cell development and the greatest therapeutic success to date in hematologic malignancies. Its uniform expression across nearly all stages of B-cell differentiation and in most B-cell neoplasms, combined with the clinical manageability of normal B-cell aplasia, make CD19 an ideal target for CAR-based redirection of T-cell cytotoxicity. The introduction of second-generation CD19-directed CAR-T cells, incorporating either a CD28 or 4-1BB costimulatory domain fused to the CD3ζ signaling module, has radically changed the treatment landscape of relapsed or refractory B-cell non-Hodgkin lymphomas (B-NHL). These costimulatory domains confer distinct kinetic and pharmacodynamic profiles: CD28-based CARs (e.g., axi-cel, brexu-cel) induce rapid T-cell expansion and potent early tumor clearance, whereas 4-1BB-based constructs (e.g., tisa-cel, liso-cel) provide slower expansion but enhanced persistence and a more favorable safety profile. In aggressive large B-cell lymphoma (LBCL), the pivotal ZUMA-1 trial first demonstrated the efficacy of axi-cel, achieving an overall response rate (ORR) of 83% and complete remission (CR) rate of 58%, with durable remissions in a heavily pretreated population (Neelapu et al., 2017). With 5-year follow-up, axi-cel maintained an estimated 5-year overall survival (OS) of 43% and median duration of complete response of 62 months, confirming long-term disease control in a subset of patients (Neelapu et al., 2023). Similarly, tisa-cel in the JULIET study achieved an ORR of 53% and CR rate of 39%, with sustained complete responses over time (Schuster et al., 2019). The TRANSCEND-NHL-001 trial evaluating liso-cel reported ORR 73% and CR 53% (Abramson et al., 2024). In mantle cell lymphoma, brexu-cel demonstrated similarly robust efficacy in ZUMA-2 study, with reported ORR 93%, CR 67% and median PFS of 25 months, establishing this product as standard of care (Wang et al., 2023). The therapeutic reach of CAR-T therapy has since expanded to indolent B-NHL: the recent phase II ZUMA-5, ELARA and TRANSCEND FL trials evaluated axi-cel, tisa-cel and liso-cel, respectively, in relapsed or refractory indolent lymphomas (follicular and marginal zone lymphoma), reporting impressive results and unprecedented durability of remission (Neelapu et al., 2024; Dreyling et al., 2024; Morschhauser et al., 2024). More recently, CAR-T cells have demonstrated superiority in

earlier treatment lines. The randomized ZUMA-7 and TRANSFORM trials established axi-cel and liso-cel, respectively, as the preferred second-line therapy for LBCL refractory to or relapsing within 12 months of first-line chemoimmunotherapy. In ZUMA-7, axi-cel significantly improved median PFS (14.7 months vs 3.7 months), and 4-year OS (55% vs 46%) compared to standard salvage therapy followed by autologous stem-cell transplantation (Westin et al., 2023). TRANSFORM trial confirmed these findings for liso-cel, showing better 3-year PFS (51% vs 26%) and 3-year OS (63% vs 52%), leading to regulatory approval in the second-line setting (Kamdar et al., 2025). In contrast, the BELINDA study of tisa-cel failed to demonstrate benefit over standard therapy, likely due to longer manufacturing times and higher disease burden at infusion (Bishop et al., 2022). Collectively, extended follow-up across pivotal trials confirms the durable efficacy of CD19-targeted CAR-T cells across both aggressive and indolent B-NHL (**Table 1**). The long-term survival plateaus observed in some of above reported studies support a disease-modifying potential, with CAR-T therapy as a new standard of care. The clinical performance of each product reflects its distinct CAR architecture, particularly the costimulatory domain and manufacturing platform, which together dictate expansion kinetics, persistence, and safety-actors that continue to inform rational design and future optimization of next-generation CAR constructs.

Product	Indication (B-NHL)	Median follow-up	ORR/CR (%)	PFS (%)	OS (%)	Median PFS (m)	Median OS (m)
Axicabtagene ciloleucel (CD28)	**LBCL ≥3L (ZUMA-1)**	≈ 5 y	83/58	5 y: 32	5 y: 43	5.9	25.8
	LBCL 2L (ZUMA-7)	≈ 47 m	83/65	4 y: 42	4 y: 55	14.7	NR
	FL/MZL ≥2L (ZUMA-5)	≈ 5 y	90/75	5 y: 50	5 y: 69	62.2	NR
Tisagenlecleucel (4-1BB)	**LBCL ≥3L (JULIET)**	≈ 40 m	53/39	/	/	2.9	11.1
	FL ≥2L (ELARA)	≈ 29 m	86/68	2 y: 57	2 y: 88	NR	NR
Lisocabtagene maraleucel (4-1BB)	**LBCL ≥3L (TRANSCEND)**	≈ 20 m	73/53	/	5 y: 38	6.8	27.5
	LBCL 2L (TRANSFORM)	≈ 34 m	87.0	3 y: 51	3 y: 63	NR	NR
	FL ≥2L (TRANSCEND FL)	≈ 18 m	97/94	1 y: 81	1 y: 92	NR	NR
Brexucabtagene autoleucel (CD28)	**MCL ≥3L (ZUMA-2)**	≈ 5 y	93/64	/	5 y: 38	25.3	46.5

Table 1. Clinical data from pivotal trials of CD19.CAR-T cells in B-NHL. *2L: second line; 3L: third line; CR: complete response; DOR: duration of response; FL: follicular lymphoma; LBCL: large B-cell lymphoma; MCL: mantle cell lymphoma; MZL: marginal zone lymphoma; m: months; B-NHL: B-cell non-Hodgkin lymphomas; NR: not reached; ORR: overall response rate; OS: overall survival; PFS: progression-free survival; y: year/years.*

CAR-T cell toxicities

CAR-T cell therapy efficacy is counterbalanced by a complex and multifactorial toxicity profile, largely reflecting the supraphysiologic immune activation and systemic inflammation elicited by the infused cellular product. The toxicities associated with CAR-T cells are mechanistically distinct from those induced by cytotoxic or antibody-based therapies and encompass both immune-mediated and tissue-specific adverse events. Cytokine release syndrome (CRS) and immune effector cell-associated neurotoxicity syndrome (ICANS) constitute the prototypical and most extensively characterized complications, resulting from cytokine storm and endothelial activation. Beyond these, an increasingly recognized spectrum of secondary toxicities - including immune effector cell-associated hematotoxicity (ICAHT), non-ICANS neurotoxicity, immune dysregulation-driven infections, coagulopathies, and metabolic or cardiovascular perturbations - contributes to morbidity and delayed recovery of patients underwent to CAR-T cell therapy (Hayden et al., 2022; Morris et al., 2022).

Cytokine Release Syndrome (CRS)

Cytokine Release Syndrome (CRS) represents the most frequent and distinctive toxicity of CAR-T cell therapy, arising from a rapid and sometimes massive release of pro-inflammatory cytokines by activated immune effector cells. Following CAR engagement, macrophages, monocytes, and T-cells release IL-6, IFN-γ, TNF-α, and other mediators that drive systemic inflammation, endothelial activation, and multiorgan dysfunction. The incidence and severity of CRS vary across CAR-T products and disease indications, ranging from 37% to 93% for any grade and 1% to 23% for grade ≥3 events (Neelapu et al., 2017; Maude et al., 2018; Schuster et al., 2019; Abramson et al., 2020; Wang et al., 2020). The consensus grading system proposed by ASTCT (Lee et al., 2019) has since become the standard framework for CRS assessment in both clinical trials and routine practice. Clinically, CRS typically begins with fever - often the first and most sensitive indicator - followed by constitutional symptoms (malaise, rigors, headache, myalgia) and, in more severe cases, hypotension, tachycardia, hypoxia, and progressive organ dysfunction culminating in distributive shock or respiratory failure. Laboratory findings are nonspecific but may reflect systemic inflammation and end-organ injury. Because the clinical presentation closely resembles sepsis, especially in neutropenic patients, a full infectious work-up and empiric antimicrobial therapy remain mandatory. Differential diagnoses include tumor lysis syndrome and rapid disease progression. Several risk factors have been associated with severe CRS, including high tumor burden, elevated baseline C-reactive protein (CRP) and lactate dehydrogenase (LDH) levels, and higher CAR-T cell dose. Patients should undergo continuous or closely scheduled monitoring in an appropriate inpatient or outpatient setting according to institutional policy, disease burden, and comorbidities. CRS grading is based on temperature, cardiovascular status, and oxygen saturation. Grade 1 CRS - fever alone - can initially be observed; however, if symptoms persist beyond 24 hours, early intervention with tocilizumab is recommended. Higher grades require prompt escalation with tocilizumab and corticosteroids, with intensive-care monitoring from grade 2 onward. Supportive measures include intravenous fluids, antipyretics, vasopressors when needed (defining grade ≥3), and broad-spectrum antibiotics. Tocilizumab, an anti-IL-6 receptor monoclonal antibody, is approved by both the FDA and EMA for CRS treatment. Prophylactic or pre-emptive administration can

attenuate severe CRS without compromising CAR-T efficacy, although it does not prevent neurotoxicity; routine prophylaxis is not currently recommended (Locke et al., 2017; Gardner et al., 2019; Kadauke et al., 2021; Locke et al., 2024). Data on other anti-cytokine agents such as siltuximab (anti-IL-6) or anakinra (IL-1 receptor antagonist) remain limited. Short courses of corticosteroids - once feared to impair CAR-T expansion - are now known to have minimal impact on efficacy; in ZUMA-1 cohort 4, early intervention with tocilizumab and dexamethasone reduced grade ≥3 CRS to 2% (Topp et al., 2021), being a strategy now widely adopted. Given the overlap between CRS and infection, most centers initiate empiric antibiotics for neutropenic fever. Recent evidence supports the early use of G-CSF from day +2, which lowers the risk of febrile neutropenia without increasing severe CRS, whereas GM-CSF administration should be avoided as it may exacerbate inflammatory toxicity (Lievin et al., 2022). Collectively, CRS exemplifies both the power and the inflammatory cost of CAR-T cell therapy. Advances in early recognition, and timely cytokine blockade have transformed CRS management, allowing safe delivery of these highly potent cellular therapies while preserving their antitumor efficacy.

Parameter	Grade 1	Grade 2	Grade 3	Grade 4
Fever *	Temperature ≥ 38°C	Temperature ≥ 38°C	Temperature ≥ 38°C	Temperature ≥ 38°C
		With		
Hypotension	None	Not requiring vasopressors	Requiring a vasopressor with / without vasopressin	Requiring multiple vasopressors (excluding vasopressin)
		And/or †		
Hypoxia	None	Low-flow nasal cannula ‡ or blow-by	High-flow nasal cannula ‡, facemask, nonrebreather mask, or Venturi mask	Positive pressure (CPAP, BiPAP, intubation, mechanical ventilation)

Table 2. ASTCT CRS Consensus Grading. *Organ toxicities associated with CRS may be graded according to CTCAE v5.0 but they do not influence CRS grading.*

** Fever is defined as temperature 38°C not attributable to any other cause. In patients who have CRS then receive antipyretic or anticytokine therapy such as tocilizumab or steroids, fever is no longer required to grade subsequent CRS severity. In this case, CRS grading is driven by hypotension and/or hypoxia.*

† CRS grade is determined by the more severe event: hypotension or hypoxia not attributable to any other cause. For example, a patient with temperature of 39.5°C, hypotension requiring 1 vasopressor, and hypoxia requiring low-flow nasal cannula is classified as grade 3 CRS.

‡ Low-flow nasal cannula is defined as oxygen delivered at 6 L/minute. Low-flow also includes blow-by oxygen delivery, sometimes used in pediatrics. High-flow nasal cannula is defined as oxygen delivered at >6 L/minute.

Immune effector cell HLH-like syndrome (IEC-HS)

Haemophagocytic lymphohistiocytosis-like toxicities following CAR-T cell infusion can occur across patient populations and CAR-T constructs and are not directly associated with CRS. ASTCT proposed diagnostic criteria (Hines et al. 2023) and proposed the term immune effector cell HLH-like syndrome (IEC-HS). Treatment of IEC-HS is focused on early identification and intervention with corticosteroids and anakinra.

Category	Criterion
Definition of IEC-HS	The development of a pathological and biochemical hyperinflammatory syndrome independent from CRS and ICANS that (1) manifests with features of macrophage activation/HLH, (2) is attributable to IEC therapy, and (3) is associated with progression or new onset of cytopenias, hyperferritinemia, coagulopathy with hypofibrinogenemia, and/or transaminitis
Criteria for Identifying IEC-HS *	**Clinical/Laboratory Manifestations**
Most common manifestations †	Required: elevated ferritin (>2 × ULN or baseline (at time of infusion)) and/or rapidly rising (per clinical assessment)
	Onset with resolving/resolved CRS or worsening inflammatory response after initial improvement with CRS-directed therapy ‡
	Hepatic transaminase elevation § (>5 × ULN (if baseline was normal) or >5 × baseline if baseline was abnormal)
	Hypofibrinogenemia (<150 mg/dL or <LLN) ‖
	Hemophagocytosis in bone marrow or other tissue ‖
	Cytopenias (new onset, worsening, or refractory ¶)
Other manifestations that may be present	Lactate dehydrogenase elevations (>ULN)
	Other coagulation abnormalities (eg, elevated PT/PTT)
	Direct hyperbilirubinemia
	New-onset splenomegaly
	Fever (new # or persistent) ‖
	Neurotoxicity
	Pulmonary manifestations (eg, hypoxia, pulmonary infiltrates, pulmonary edema)
	Renal insufficiency (new onset)
	Hypertriglyceridemia (fasting level, >265 mg/dL ‖)

Table 3. IEC-HS: Definition and Identification. *LLN: lower limit of normal; ULN: upper limit of normal.*

******* *Diagnosis was made only when not attributable to alternative etiologies, including CRS, infection and/or disease progression.*

† Constellation of findings typically simultaneously (e.g., all within 72 hours).

‡ *Although most cases of IEC-HS have been seen with antecedent CRS, this may not always be the case, and emerging experience will shed light on how IEC-HS may present.*

§ *Consistent with grade 3 hepatic transaminase elevations according to Common Terminology for Adverse Events version 5.0.*

‖ *According to HLH-2004.*

¶ *Generally at least 1 lineage will be a grade 4 cytopenia (platelets, neutrophils, hemoglobin).*

As distinguished from CRS onset or recrudescence.

Immune Effector Cell-Associated Neurotoxicity Syndrome (ICANS)

Immune Effector Cell-Associated Neurotoxicity Syndrome (ICANS) occurs in 20-60% of CAR-T patients, of whom 12-30% develop severe manifestations (grade ≥3). Moreover, severe steroid-refractory ICANS is associated with a worse prognosis. The underlying mechanism driving the syndrome is not fully understood, but there is evidence for the release of inflammatory cytokines, increasing vascular permeability and endothelial activation leading to blood brain barrier breakdown. The onset of ICANS is, on average, around 5 days following CAR-T cell infusion, sometimes concurrently with or shortly after CRS. However, about 10% of patients present more than 3 weeks after CAR-T cell infusion, known as delayed ICANS. Risk factors include high disease burden, patient age, CAR-T expansion and the specific CAR-T-cell product. Patients experience mild tremor and confusion, which can proceed to agitation, seizures and cerebral oedema. A prominent and early feature of ICANS is hesitancy of speech and deterioration in handwriting, which can progress to aphasia with both expressive and receptive components, whereby the patient is alert but mute. The most devastating consequence of ICANS is the occurrence of status epilepticus, fatal cerebral oedema and occasionally intracerebral haemorrhage. ICANS is a clinical diagnosis: MRI brain scans and CSF studies are rarely helpful in ruling out alternative diagnoses such as central nervous system (CNS) infection; the EEG recording can be normal, but can also demonstrate a pattern of variable abnormalities, including non-convulsive status epilepticus. All patients should be proactively monitored for subtle changes in cognition, using the 10-point Immune Effector Cell Encephalopathy (ICE) score (**Table 3**), which evaluates orientation, attention, writing and language. This score is then integrated into an overall assessment of neurological function incorporating seizure activity, change in conscious level, motor findings and elevation in intracerebral pressure/cerebral oedema to give an ICANS grade. (**Table 4**; Lee et al., 2019). Any patient with an ICE score less than 2 or with seizures is classified as severe (grade 3 or 4) and should be transferred to Intensive Care Unit. Factors associated with a higher risk of ≥ grade 3 ICANS include low platelet count, increasing ferritin, and the development of early and severe CRS. There is no specific treatment for ICANS. Management is supportive for grade 1; for grade ≥2 ICANS, corticosteroid therapy should be given until symptoms have improved. Seizures are treated with levetiracetam and the status with

benzodiazepines. Most cases resolve with supportive care and early intervention with corticosteroid therapy. Steroid-refractory ICANS can be defined as occurring when there is no improvement of grade 4 ICANS after 3 days of high-dose steroids (Velasco et al. 2023). There are no high-quality studies to guide treatment of this condition and possible treatment options (Velasco et al. 2023; Ferreri et al., 2024) include: anakinra (Gazeau et al. 2023), an IL-1 receptor antagonist; intrathecal hydrocortisone and/or triple-therapy with methotrexate and cytarabine (Zurko et al. 2022); dasatinib, a tyrosine kinase inhibitor; siltuximab, an IL-6 inhibitor; ruxolitinib, a janus-kinase inhibitor. The most abundant safety and efficacy data for steroid-refractory ICANS are available for anakinra, which is associated with an overall response rate of 77% (Gazeau et al. 2023). Despite promising preclinical data, larger case series confirming clinical efficacy of dasatinib, siltuximab and ruxolitinib are not yet available (Ferreri et al., 2024).

Immune Effector Cell Encephalopathy (ICE)
• **Orientation**: orientation to year, month, city, hospital (4 points) • **Naming**: ability to name 3 objects (eg, point to clock, pen, button) (3 points) • **Following**: commands: ability to follow simple commands (1 point) • **Writing**: ability to write a standard sentence (1 point) • **Attention**: ability to count backwards from 100 by 10 (1 point)

Table 4. Immune Effector Cell Encephalopathy (ICE) Score.

Neurotoxicity Domain	Grade 1	Grade 2	Grade 3	Grade 4
ICE score *	7-9	3-6	0-2	0 (patient is unarousable and unable to perform ICE)
Depressed level of consciousness †	Awakens spontaneously	Awakens to voice	Awakens only to tactile stimulus	Patient is unarousable or requires vigorous or repetitive tactile stimuli to arouse. Stupor or coma
Seizure	N/A	N/A	Any clinical seizure focal or generalized that resolves rapidly or nonconvulsive seizures on EEG that resolve with intervention	Life-threatening prolonged seizure (>5 min); or Repetitive clinical or electrical seizures without return to baseline in between
Motor findings ‡	N/A	N/A	N/A	Deep focal motor weakness such as hemiparesis or paraparesis
Elevated ICP/cerebral edema	N/A	N/A	Focal/local edema on neuroimaging §	Diffuse cerebral edema on neuroimaging; decerebrate or decorticate posturing; or cranial nerve VI palsy; or papilledema; or Cushing's triad

Table 5. ASTCT ICANS Consensus Grading for Adults. *N/A: not applicable.*

** A patient with an ICE score of 0 may be classified as grade 3 ICANS if awake with global aphasia, but a patient with an ICE score of 0 may be classified as grade 4 ICANS if unarousable.*

† Depressed level of consciousness should be attributable to no other cause (e.g., no sedating medication).

‡ Tremors and myoclonus associated with immune effector cell therapies may be graded according to CTCAE v5.0, but they do not influence ICANS grading.

§ Intracranial hemorrhage with or without associated edema is not considered a neurotoxicity feature and is excluded from ICANS grading. It may be graded according to CTCAE v5

Other complications of CAR-T cell therapy

As expected, infectious complications remain a major source of morbidity and mortality even after CAR-T cell infusion (Cordas Dos Santos et al., 2024). Patients are at increased risk for opportunistic infections due to profound and durable lymphopenia, B-cell aplasia, hypogammaglobulinemia, and delayed immune reconstitution (Hayden et al., 2022). The risk profile evolves over time: early post-infusion infections are typically bacterial and related to neutropenia or mucosal damage, whereas late infections are predominantly viral or fungal and often correlate with immune reconstitution deficits or ongoing corticosteroid and tocilizumab exposure. Vaccination strategies, antimicrobial prophylaxis, and intravenous immunoglobulin replacement are therefore key components of long-term supportive care in CAR-T recipients. Beyond the well-known immune-mediated toxicities such as CRS, IEC-HS and ICANS, a heterogeneous group of less frequent yet clinically relevant complications have been increasingly recognized following CAR-T cell therapy. Among these, immune effector cell-associated hematotoxicity (ICAHT) represents a distinct and often sustained form of bone marrow dysfunction, manifesting as persistent or biphasic cytopenias that extend beyond the expected recovery phase after lymphodepleting chemotherapy. Its pathogenesis appears multifactorial, involving cytokine-driven myelosuppression, microenvironmental damage, immune dysregulation, and possible clonal hematopoiesis or, rarely, secondary myeloid neoplasms (Rejeski et al., 2023; Rejeski et al., 2024). Prolonged cytopenias have been associated with increased transfusion requirements, and a higher incidence of severe infections and mortality, thereby representing an unmet need in CAR-T survivorship management. Moreover, non-ICANS neurotoxicity is increasingly described and may include peripheral neuropathies, demyelinating disorders, cranial nerve palsies, and myelitis (Graham et al., 2025). Unlike ICANS, these events often present later, may not correlate with systemic inflammation, and are hypothesized to arise from on target-off tumor mechanisms, immune reconstitution-related autoimmunity, or infections-related mechanisms. Recognition of these patterns is crucial, as their management differs from standard ICANS-directed interventions and may require prolonged immunosuppressive therapy or targeted neurologic evaluation (Graham et al., 2025). Overall, these less frequent but consequential complications - encompassing ICAHT and non-ICANS neurotoxicity - underscore the complex

interplay between immune activation, tissue injury, and delayed immune recovery after CAR-T cell therapy. A comprehensive understanding of their mechanisms and natural history is essential to optimize patient outcomes, improve risk stratification, and inform next-generation CAR design aimed at reducing off-target and delayed toxicities.

Extracellular vesicles

Extracellular vesicles (EVs) have emerged as central regulators of immune communication, providing a conserved mechanism for the transfer of molecular information between immune and non-immune cells. These membrane-enclosed nanoparticles are released by virtually all cell types and encompass heterogeneous populations that differ in size, biogenesis and molecular composition, including small EVs (~30-150 nm), microvesicles (approximately 100-1,000 nm) and larger vesicular structures generated during apoptosis. EVs carry complex cargos of proteins, lipids, metabolites and nucleic acids that reflect the functional state of their parental cells. Phenotypically, EVs are enriched in membrane proteins associated with their cellular origin and intracellular trafficking pathways. Common markers include tetraspanins such as CD9, CD63 and CD81, while lineage-specific molecules - including antigen receptors or co-stimulatory ligands - can be selectively incorporated depending on the cell subtype releasing the vesicles. This phenotypic plasticity allows EVs to function as both messengers and modulators between cells in immune responses, but also introduces significant analytical challenges related to heterogeneity and standardization. A major immunological function of EVs involves antigen presentation and the orchestration of adaptive immune responses. Early studies demonstrated that B cells and dendritic cells release EVs carrying peptide–MHC complexes capable of stimulating T cells either directly or indirectly through cross-presentation pathways. EV-mediated transfer of antigens, costimulatory molecules and regulatory microRNAs contributes to the maturation of antigen-presenting cells, the activation of cytotoxic lymphocytes and the shaping of germinal center reactions. These findings support the concept that EVs act as mobile immunological platforms extending the communication range of immune synapses. Beyond antigen presentation, EVs exert broad immunoregulatory functions in innate and adaptive immunity. Vesicles released by neutrophils, platelets, macrophages and T lymphocytes can modulate inflammatory cascades, regulate cytokine networks and influence leukocyte recruitment. Depending on their cargo and cellular origin, EVs may amplify immune activation or promote immunosuppressive pathways, thereby contributing to immune homeostasis as well as pathological conditions such as autoimmunity, allergy and cancer. Notably, T cell-derived vesicles released at the

immunological synapse have been shown to transport T cell receptor–associated molecules and effector proteins, highlighting their role as active participants in cytotoxic and helper T cell responses. Chimeric antigen receptor (CAR) T cell-derived EVs have also attracted significant attention recently (**Figure 5**; Möller A et al., 2020). These EVs express high levels of perforin and granzyme B as well as CARs, and thus can induce the death of tumor cells expressing their cognate antigen. Importantly, they have therapeutic potential even in the case of solid tumors, where the efficacy of CAR T cell therapy is limited by the poor penetration of the tumors by CAR T cells. Recent technological advances have further expanded the translational relevance of EV research. High-resolution imaging, single-vesicle phenotyping and multi-omics profiling now enable detailed characterization of EV heterogeneity, cargo selection and functional dynamics. Such approaches are expected to improve our understanding of immune communication networks and to facilitate the development of EV-based biomarkers for monitoring immune activation, treatment response and toxicity. Despite these advances, several challenges remain. The diversity of EV subtypes, overlapping size distributions and the absence of universally specific markers complicate classification and functional interpretation. Overall, EVs are increasingly recognized as fundamental components of immune regulation, bridging innate and adaptive responses through the transfer of functional molecular cargo. Their nanoscale dimensions, dynamic phenotypic signatures and capacity to mediate long-distance signaling position them at the intersection of basic immunology and translational research (Buzas et al., 2023).

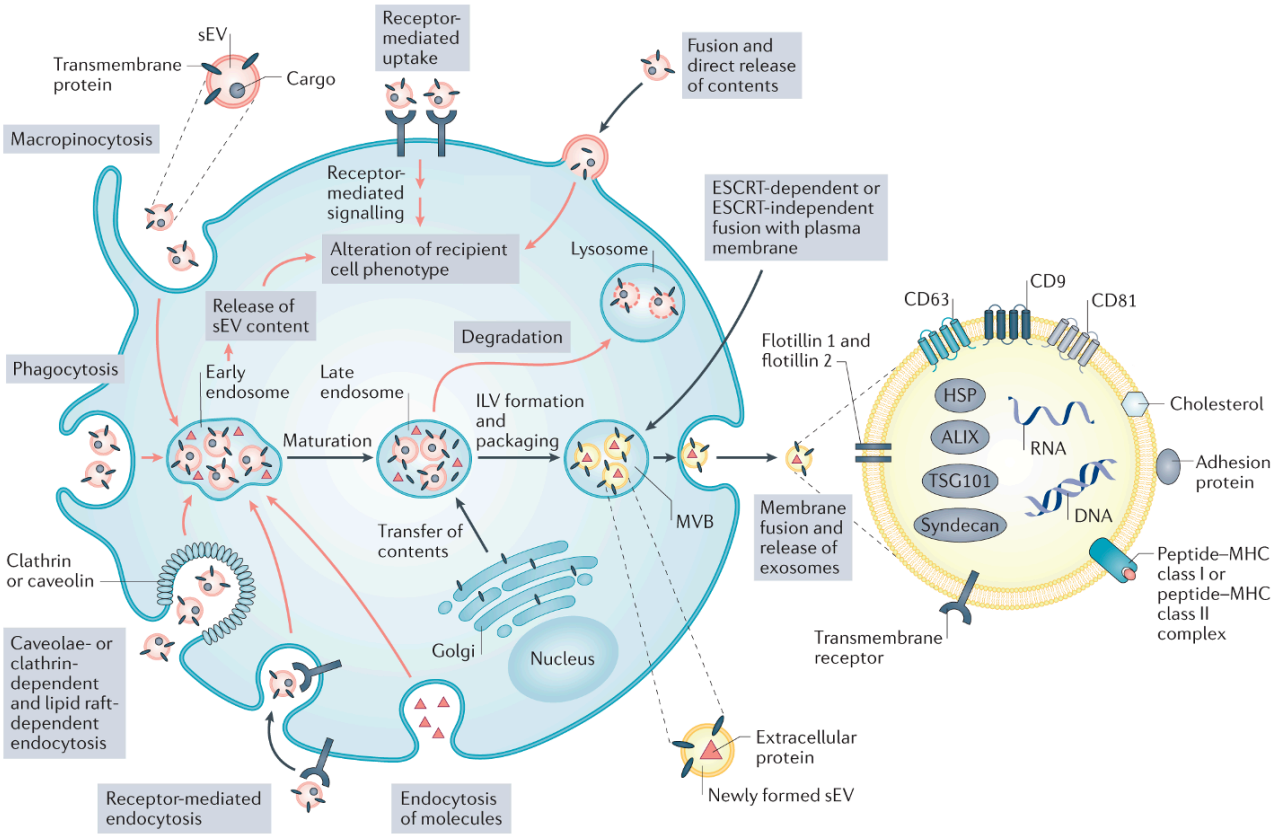

Figure 5. Small extracellular vesicles (sEVs) biogenesis and release. *Adapted from Möller A et al., 2020.*

AIM OF THE STUDY

Although CAR-T cell therapy has revolutionized the treatment of B-cell non-Hodgkin lymphomas with remarkable efficacy, it should be emphasized that this approach is not devoid of adverse effects. The most common adverse events in CD19.CAR-T therapies are CRS and ICANS (Santomasso et al., 2021). ICANS is clinically characterized by encephalopathy, cognitive impairment, language disturbances, seizures, and, rarely, cerebral edema (Gust et al., 2017; Santomasso et al., 2018; Karschnia et al., 2019; Strati et al., 2020). Several factors have been reported to be associated with ICANS: age, performance status, disease burden, disease type, infused CAR-T cell dosage, presence and severity of CRS and its shorter time to onset, and presence of preexistent neurological comorbidities (Wudhikarn et al., 2020; Greenbaum et al., 2021; Pensato et al., 2023). Although ICANS is rarely fatal (1%-2%), its management requires high-dose steroids and immunosuppressive therapies, which potentially affect CAR-T cell activity and therapy efficacy, as well as non-relapse mortality (Hayden et al., 2022; Cordas Dos Santos et al., 2024). The pathogenesis of ICANS has been associated with endothelial damage, blood-brain barrier disruption, and glial cell injury (Morris et al., 2022). High C-reactive protein and serum ferritin levels (i.e., baseline inflammatory status), as well as IL-2, IL-3, IL-6, IL-10, IL-15, MCP-1, GM-CSF, and IFN-γ levels measured after CAR-T cell infusion, have been reported to be associated with increased risk of ICANS (Gust et al., 2017; Santomasso et al., 2018; Locke et al., 2020). Owing to the lack of tissue specificity, these biochemical parameters can only presumably be related to the functional dynamics of infused CAR-T cells. The latter can be assessed by the direct examination of lymph nodes and tumor tissues after CAR-T cell infusion, which are, however, not easily accessible in clinical practice. This issue is particularly relevant, even for the demonstration of CNS involvement during ICANS, given that CAR-T cells have been found both in the parenchyma and in the cerebrospinal fluid (Gust et al., 2017; Santomasso et al., 2018). Plasma/serum extracellular vesicles (EVs) are nano-sized structures released from all cell types, which can mirror the cell-of-origin membrane phenotype (Théry et al., 2009; Buzas et al., 2023). Importantly, EVs mediate cell-cell crosstalk and take part in a variety of biological processes, such as immune and inflammatory responses (Théry et al., 2009). In this regard, it has been

previously reported that CAR-T cells are capable of releasing EVs that carry the CAR construct (Fu et al., 2019; Aharon et al., 2021). Following this observation, the aims of this study were:

- to demonstrate the existence of CAR^+ extracellular vesicles (CAR^+EVs) and their release by CD19-directed CAR-T cells;
- to characterize plasma CAR^+EVs both quantitatively and qualitatively, including their concentration, size distribution and phenotypic profile;
- to assess the ability of CAR^+EVs to provide information on CD19-directed CAR-T cell in vivo function and trafficking;
- to evaluate CAR^+EVs as potential plasma biomarkers predictive of immune effector cell–associated neurotoxicity syndrome (ICANS) in patients with relapsed or refractory B-cell non-Hodgkin lymphoma treated with CD19-directed CAR-T cell therapy.

METHODS

Study design

This prospective, observational tissue-based study was designed to identify biomarkers predictive of treatment-related complications in patients with relapsed or refractory B-cell lymphoma undergoing CD19-directed CAR-T cell therapy. All participants received CAR-T products approved by the Italian Medicines Agency (AIFA), including tisagenlecleucel, axicabtagene ciloleucel, and brexucabtagene autoleucel. Eligible patients were consecutively treated at the IRCCS Azienda Ospedaliero-Universitaria di Bologna (IRCCS AOU di Bologna) after providing written informed consent. The study protocols were reviewed and approved by the local Ethics Committee, conducted in accordance with the principles of the Declaration of Helsinki.

Sampling and biochemical assessment

Peripheral blood samples were obtained by venipuncture and collected into 10 mL EDTA tubes. Sampling followed a schedule including pre-lymphodepletion (at ward admission) and 1 hour as well as 1, 3, 5, 7, 9, 11, 13, 21, and 30 days after CD19.CAR-T cell infusion. Plasma was separated by centrifugation at 1500*g* for 15 minutes at room temperature. Plasma and whole-blood aliquots were immediately processed and stored at -80 °C until analysis. Biochemistry assessments were performed by the clinical laboratory service at IRCCS AOU di Bologna.

Molecular tracking of CAR-DNA by droplet digital PCR (ddPCR)

Genomic DNA was extracted from 200 µL of whole blood using the QIAamp DNA Mini and Blood Mini Kit (Qiagen, Cat. No. 51104, Hilden, Germany) and quantified with a NanoDrop™ One spectrophotometer (Thermo Fisher Scientific, Waltham, MA, USA). Quantification of circulating CAR-DNA copies was performed using droplet digital PCR (ddPCR) technology (Bio-Rad, Hercules, CA,

USA). The assay employed the Axi-Cel/Tisa-Cel CD19.CAR-T-specific Expert Design Assay (Bio-Rad, dEXD88164642; amplicon size 95 bp), duplexed with the human RPP30 Copy Number Reference Assay (Bio-Rad, dHsaCP2500350). Genomic DNA underwent digestion with HaeIII enzyme (Thermo Fisher Scientific, Cat. No. ER0151), added directly to the ddPCR reaction mix. Each 20 µL reaction contained 10 µL of 2× QX200 ddPCR Supermix for Probes (no dUTP) (Bio-Rad, Cat. No. 1863023), 1 µL of 20× CD19.CAR-T assay (labeled with a 5′ 6-FAM fluorophore and a 3′ Iowa Black® FQ quencher), 1 µL of 20× RPP30 assay (labeled with a 5′ HEX fluorophore and a 3′ Iowa Black® FQ quencher), 1 µL of HaeIII restriction enzyme (5 U/µL), and a variable amount of DNA template and nuclease-free water to reach the final reaction volume. When DNA input ranged between 20 and 80 ng, a fixed volume of 2 µL was used per reaction. Thermal cycling was performed under the following conditions: 95 °C for 10 min, followed by 40 cycles with 94 °C for 30 s and 60 °C for 1 min, and a final enzyme inactivation step at 98 °C for 10 min, with an infinite hold at 4 °C. Droplet generation and fluorescence signal acquisition were performed using the QX200 ddPCR System (Bio-Rad), and data were analyzed with QuantaSoft™ software version 1.7 (Bio-Rad, Cat. No. 1864011). Absolute number of CAR-DNA copies per mL of blood was calculated by multiplying the ddPCR-derived concentration (copies/µL) for the appropriate dilution factor and adjusting for 1 mL volume of blood.

miR-1246 plasma levels quantification by ddPCR

Total RNA, including miRNA, was purified from 200 µL of plasma from 20 patients collected at day +5, using Maxwell RSC miRNA plasma and serum kit and Maxwell RSC instrument according to manufacturer's instructions (Cat#AS1680, Promega). A volume of 3 µL of RNA was converted into cDNA by using the miRCURY LNA RT kit (Cat#339340, Qiagen). Evagreen-based Droplet Digital PCR was performed to assess miR-1246 levels. Briefly, 20 µL of PCR reaction containing 10 µL of 2X EvaGreen Supermix (Cat#186-4033, Bio-Rad), 1 µL of miRCURY LNA miRNA assay (Cat#339306, GeneGlobe ID - YP00205630, Qiagen), 1 µL of nuclease-free and 8 µL of diluted cDNA (1:50). Thermal cycling conditions were: 95°C for 5 min, 40 cycles of 95°C for 30 s and 58°C for 1

min, and three final steps at 4°C for 5 min, 90°C for 5 min and a 4°C infinite hold. Data analysis was performed using QuantaSoft™ Software version 1.7 (Cat #1864011, Bio-Rad) and the absolute level of circulating miR-1246 was obtained by multiplying the ddPCR concentration (copies/µL) for the dilution factor.

Multiparametric flow cytometry (MFC) for CAR$^+$T cell tracking and sorting

Tracking of circulating CAR$^+$T cells was performed on freshly collected whole blood samples at all available time points. Cells were stained with the APC-conjugated anti-CD19 CAR FMC63 idiotype antibody (Miltenyi Biotec, Cat. No. 130-127-343) and subsequently, were labeled with the following panel of fluorochrome-conjugated anti-human monoclonal antibodies: CD3-FITC, clone SK7 (BD Biosciences, Cat. No. 340851, RRID:AB_400139); CD8-PE-Cy7, clone HIT8A (BD Biosciences, Cat. No. 566858, RRID:AB_2869912); CD45-V500, clone HI30 (BD Biosciences, Cat. No. 560777, RRID:AB_1937324); CD45RA-PerCP-Cy5.5, clone HI100 (BD Biosciences, Cat. No. 563429, RRID:AB_2738199); and CD62L-BV421, clone DREG-56 (BD Biosciences, Cat. No. 563862, RRID:AB_2738455). Flow cytometric acquisition was performed on a 3-laser FACSCanto II cytometer (BD Biosciences). For each analysis, a minimum of 50,000 CD45$^+$ lymphocytes were acquired. Data were analyzed using FACSDiva software version 6.1.1 and FCS Express 7 Reader. Appropriate isotype-matched controls were included for each staining condition to ensure gating specificity. For sorting experiments, 19BBζ.CAR-T cells were first counted and stained with recombinant human CD3-FITC (clone REA613, Miltenyi Biotec, Cat. No. 130-113-697, RRID:AB_2726238), CD19 CAR FMC63 Idiotype-APC (clone REA1297, Miltenyi Biotec, Cat. No. 130-127-343), and CD45-VioGreen (clone REA747, Miltenyi Biotec, Cat. No. 130-122-311, RRID:AB_2801892). Stained cells were washed, resuspended in TexMACS medium (Miltenyi Biotec, Cat. No. 130-097-196) and loaded into a MACSQuant Tyto High-Speed Cartridge (Miltenyi Biotec). CD3$^+$CAR$^+$T cells were isolated using the MACSQuant Tyto sorter (Miltenyi Biotec). Pre- and post-sorting purity assessments were performed on a MACSQuant16 cytometer using

MACSQuantify software (Miltenyi Biotec) to confirm the efficiency and integrity of the sorting procedure.

Protein ELLA cytokine assay

Plasma concentrations of selected interleukins (e.g., IL-15, GDF15), chemokines (e.g., CX3CL1, CXCL9), and neurofilament light chain (NFL) were quantified using the high-performance automated microfluidic immunoassay platform Protein ELLA (Bio-Techne, Minneapolis, MN, USA), enabling multiplexed detection and precise measurement of low-abundance analytes.

Generation of 19BBζ.CAR-T and 19BBζ.eGFP.CAR-T cells

Replication-defective, third-generation lentiviral vectors encoding the CD19-targeting CAR constructs - 19BBζ.CAR-T (pLV[CAR]-EF1A>CD8-leader/CD19-scFv/CD8-hinge/CD8-TM/4-1BB-CD3ζ; VB220923 -1237mwu) and its eGFP-tagged variant 19BBζ.eGFP.CAR-T (pLV[CAR]-EF1A>CD8-leader/CD19-scFv/CD8-hinge/CD8-TM/4-1BB-CD3ζ:Linker:EGFP; VB230125-1128xqf) - were obtained from VectorBuilder (Chicago, IL, USA) and produced in HEK293T cells (ATCC, Manassas, VA, USA; RRID:CVCL_HA71). Briefly, 0.6×10^6 cells were seeded in 10 cm culture dishes (Corning, NY, USA) in high-glucose DMEM (Corning) and transfected 72 hours later using the Lentiviral Packaging Kit (OriGene, Rockville, MD, USA; Cat. TR30037) with 7 µg of either 19BBζ.CAR-T or 19BBζ.eGFP.CAR-T lentiviral vectors. Lipofectamine and plasmid DNA were diluted in Opti-MEM medium (Gibco, Thermo Fisher Scientific, Waltham, MA, USA). Sixteen hours post-transfection, the medium was replaced, and viral supernatants were harvested at 48 h and 72 h, then concentrated using the Lentivirus Concentration Solution (OriGene). For T-cell transduction, $CD3^+$ T cells were isolated from the peripheral blood of seven healthy donors using CD3 microbeads (Miltenyi Biotec, Bergisch Gladbach, Germany). Purified cells were cultured in TexMACS medium (Miltenyi Biotec) supplemented with IL-7 (10 ng/mL; Cat. 130-095-367) and IL-15 (10 ng/mL; Cat. 130-095-760) and stimulated for 48 hours with T Cell TransAct (Cat. 130-128-758, Miltenyi Biotec).

Activated T cells were then transduced with the 19BBζ.CAR-T or 19BBζ.eGFP.CAR-T lentiviral supernatant at a multiplicity of infection (MOI) of 20, in retronectin-coated 24-well plates (Takara Bio, Kusatsu, Japan). After 3 days, CAR expression was evaluated by flow cytometry using an APC-conjugated anti-human CD19 CAR FMC63 idiotype antibody (Miltenyi Biotec, Cat. 130-127-343), by confocal microscopy, and by direct eGFP fluorescence detection using FACSCanto II cytometer (BD Biosciences, San Jose, CA, USA).

Cell line culture conditions and engineering of KOPN8 and K562 cells

HEK293T cells (Takara Bio, Saint-Germain-en-Laye, France) were cultured in high-glucose Dulbecco's Modified Eagle Medium (DMEM; Corning) supplemented with 10% fetal bovine serum (FBS; Gibco, Thermo Fisher Scientific), 2 mM L-glutamine, and 2 mM penicillin-streptomycin (Gibco, Thermo Fisher Scientific). KOPN8 (DSMZ, Braunschweig, Germany; RRID:CVCL_1866) and K562 (DSMZ; RRID:CVCL_0004) cell lines were cultured in RPMI 1640 medium (Corning) supplemented with 10% FBS, 2 mM L-glutamine, and 2 mM penicillin-streptomycin under standard conditions (37 °C, 5% CO_2). To generate a luminescent reporter model, KOPN8 cells were transduced with the Lenti-luciferase-P2A-Neo lentiviral construct (a gift from Christopher Vakoc; Addgene plasmid #105621; RRID:Addgene_105621, Watertown, MA, USA) and selected with G418 (Thermo Fisher Scientific) for 96 hours to establish a stable luciferase-expressing line. K562 cells were genetically modified to express the human CD19 receptor using a PiggyBac transposon system containing CD19 cDNA linked to a puromycin resistance cassette under the control of the mouse phosphoglycerate kinase (mPGK) promoter (VectorBuilder, plasmid pPB[Exp]-mPGK>hCD19NM_001178098.2:T2A:Puro; VB220309-1186msb). One week after thawing, 0.8 × 10^6 K562 cells were electroporated using a 2D Nucleofector system (Lonza, Basel, Switzerland) with 1 µg of transposase plasmid (VectorBuilder) and 3 µg of PiggyBac-CD19 plasmid. Seventy-two hours post-transfection, cells were selected with 3 µg of puromycin (Sigma-Aldrich, Merck Millipore, Darmstadt, Germany) for additional 72 hours. CD19 surface expression was subsequently verified

by multiparametric flow cytometry using an anti-human CD19-PE-Cy7 antibody (clone SJ25C1, BD Biosciences, Cat. No. 341113, RRID:AB_2868769) on a FACSCanto II cytometer (BD Biosciences).

Induced pluripotent stem cells (iPSCs) culture and differentiation

Previously reprogrammed and characterized healthy donor iPSCs (Messelodi et al., 2021) were maintained in feeder free conditions and cultured in six well plates (Corning) coated with Vitronectin (Thermo Fisher Scientific) in Essential 8 medium (Thermo Fisher Scientific) as previously described (Bertuccio et al., 2020). Mature midbrain neurons were obtained by first differentiating iPSCs to the neural precursor cell (NPC) stage (Reinhardt et al., 2013) and subsequently stimulating the differentiation towards the ventral central nervous system as previously described (Messelodi et al., 2023). Mature NPCs and neurons were seeded on Matrigel-coated plates for functional assays and imaging by confocal microscopy.

Cytotoxicity and MTT assays

To test the killing capacity of 19BBζ.CAR-T cells, they were co-cultured at a 1:1 ratio with CD19-engineered KOPN8 or K562 cells. The killing rate was measured by flow cytometry after 24 hours as percentage of residual $CD19^+$ living cells. 19BBζ.CAR-T cell-induced cell death in KOPN8 engineered to express luciferase was measured by luciferase assay: after 24 hours, the amount of residual KOPN8 cells was evaluated through the Steady-Glo Luciferase Assay System (Cat# E2510, Promega, Madison, Wisconsin, USA) and the luminescence plate reader (Tecan, Männedorf, Switzerland). Metabolic activity of neurons administered or not with CAR+EVs were evaluated with MTT cell proliferation assay (Roche Life science, Milan, Italy).

Flow cytometric analysis and sorting of CAR$^+$ extracellular vesicles

Extracellular vesicles isolated from patient plasma, manufacturing bag leftovers (BLs), and cell culture supernatants were analyzed and quantified by multiparametric flow cytometry (MFC) using two independent platforms: FACSLyric (BD Biosciences) and CytoFLEX (Beckman Coulter). Regarding “Protocol 1”, on the FACSLyric instrument, 5 µL of patient serum was diluted in 95 µL of 0.1 µm-filtered PBS and incubated with 95 µL of an antibody cocktail containing anti-human CD31-PE-Cy5.5 (clone WM-59; BD Biosciences, Cat. 563651, RRID:AB_2738348), CD45-BV510 (clone HI30; BD Biosciences, Cat. 563204, RRID:AB_2738067), and CD41a-PE (clone HIP8; BD Biosciences, Cat. 557297, RRID:AB_396624). FITC-conjugated phalloidin and an APC-conjugated lipophilic cationic dye (Dye Integer EV Detection Kit; BD Biosciences, Cat. 626267) were used to exclude non-vesicular events. Absolute EV counts (EVs/µL) were determined using the TruCount (BD Biosciences) system (Marchisio et al., 2020; Storci et al., 2023). Regarding “Protocol 2” (Cointe et al., 2017), Megamix-Plus FSC calibration beads of defined size (BioCytex, STAGO Group, Cat. 7802) were used to set the gating strategy and define EV subpopulations based on size distribution, following the manufacturer’s recommendations. Subsequent phenotypic analyses were performed on size-gated events. In both protocols, CAR$^+$EVs were identified using PE- or APC-conjugated anti-CD19 CAR FMC63 idiotype antibodies (Miltenyi Biotec, Cat. 130-127-342 and Cat. 130-127-343, clone REA1297). Additional staining included fluorochrome-conjugated anti-human monoclonal antibodies targeting CD63-BV510 (clone H5C6; BD Biosciences, Cat. 740182, RRID:AB_2739935), perforin-PerCP-Cy5.5 (clone δG9; BD Biosciences, Cat. 563762, RRID:AB_2738409), FAS ligand-PE (clone NOCK-1; BD Biosciences, Cat. 564261, RRID:AB_2738713), CD107a-APC-H7 (clone H4A3; BD Biosciences, Cat. 561343, RRID:AB_10644020), CD8β-PE (clone 2ST8.5H7; BD Biosciences, Cat. 641057, RRID:AB_1645747), CD19-PE-Cy7 (clone SJ25C1; BD Biosciences, Cat. 557835, RRID:AB_396893), ZAP70-FITC (clone 1E7.2; BD Biosciences, Cat. 344934, RRID:AB_647380), CD151-Alexa Fluor 488 (clone 210127; R&D Systems), and ENO2-PE (clone ENO2/1375; Novus Biologicals, Bio-Techne). Protocol 2 was applied whenever fluorochrome emission spectra overlapped with those used in Protocol 1. A representative comparison of the two protocols is shown in **Figure 1A-B**. Sorting of CAR$^+$EVs was performed using the CytoFLEX SRT

cell sorter (Beckman Coulter). The gating strategy combined the size-based regions defined by Protocol 2 with violet laser side scatter (SSC) parameters. Sorting regions were defined by fluorescent marker expression, and approximately 10^6 events were collected per sample into sterile tubes and stored at -80 °C for downstream analyses (**Figure 1C**).

EV purification by differential ultracentrifugation

Extracellular vesicles (EVs) were isolated from 1 mL of CAR-T patient plasma by sequential differential ultracentrifugation. Plasma samples were centrifuged at 1,500*g* for 15 minutes, followed by 2,500*g* for 15 minutes, 20,000*g* for 1 hour, and finally 100,000*g* for 3 hours (Beckman Coulter). The resulting EV pellet was resuspended in sterile 0.1 µm-filtered PBS and stored at -80 °C until further use.

CAR^+EV pull-down assay

CAR^+EVs were isolated from patient plasma using a customized immunoaffinity-based capture system (Hansa Biomed, Tallinn, Estonia). Briefly, 0.4 µm latex beads covalently coupled to anti-CD19 CAR FMC63 idiotype antibody (clone REA1297; Miltenyi Biotec, Cat. 130-127-983) were incubated overnight with human plasma according to the manufacturer's protocol. Bound CAR^+EVs were subsequently eluted from the immunobeads following the manufacturer's protocol. The recovered vesicles were quantified by MFC; **Figure 1D**) and their size distribution was determined by Nanoparticle Tracking Analysis (NTA).

EV purification using SmartSEC size-exclusion chromatography

Size-exclusion chromatography (SEC) was employed for the purification of extracellular vesicles (EVs) intended for flow cytometric and ExoView analyses. Following differential ultracentrifugation, EV pellets were resuspended in 100 µL of 0.1 µm-filtered PBS and applied to SmartSEC columns

(SSEC100A-1; System Biosciences, Palo Alto, CA, USA). Column separation and EV recovery were performed according to the manufacturer's instructions.

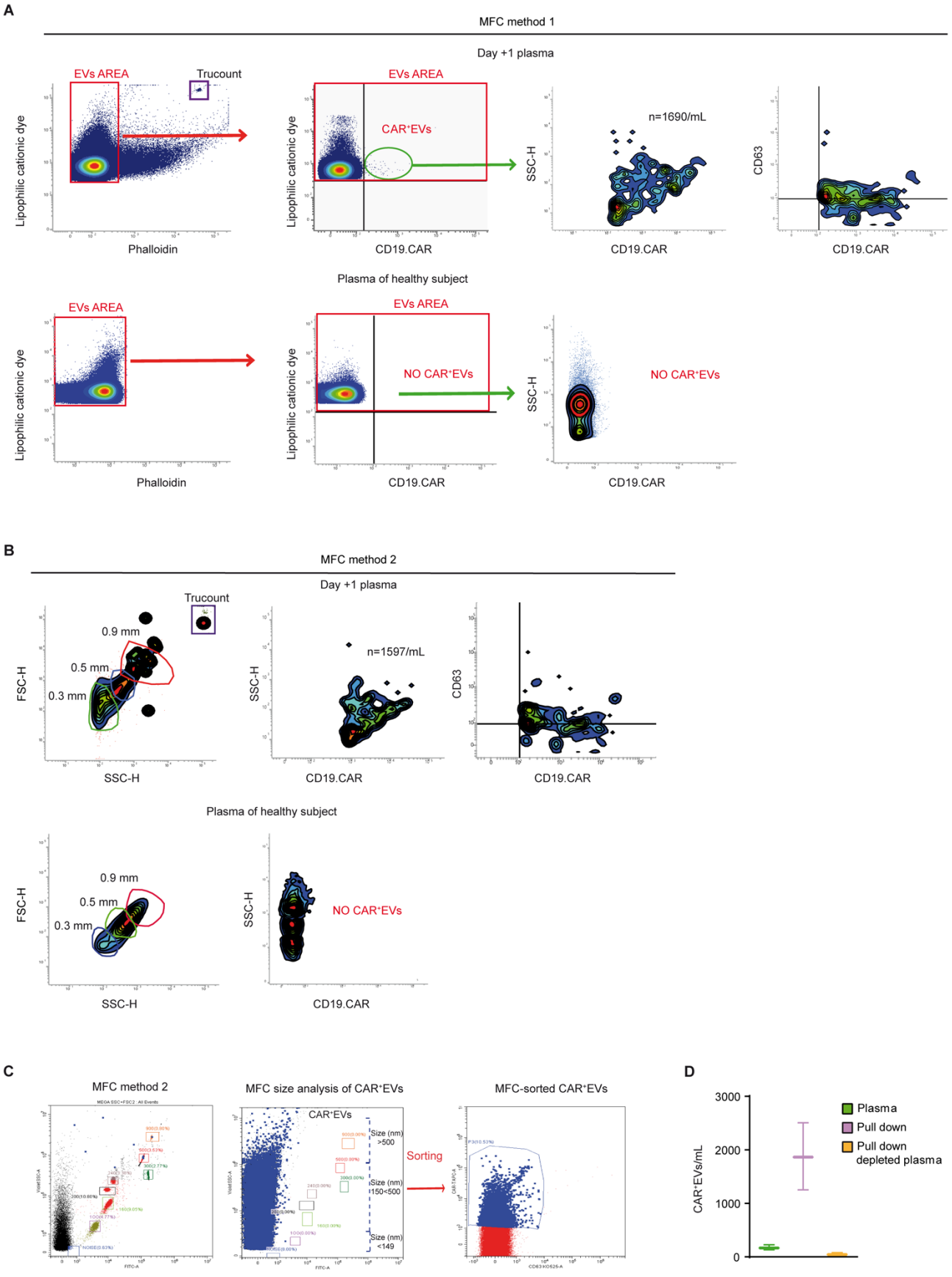

Figure 1. CAR+EV MFC analysis. *Gating strategy for (**A**) method 1 and (**B**) method 2 performed on a healthy subject plasma and on a patient plasma at day +1 after CD19.CAR-T cell infusion: number*

*of CAR$^+$EV is reported, coexpression of the CD63 exosomal marker on CAR$^+$EVs is shown. (**C**) MFC-sorting strategy of plasma CAR$^+$EVs by method 2: Megamix size distribution assessed by violet-laser side scatter (SSC) vs FITC, CAR$^+$EVs size distribution, and presence of CD63 exosomal marker on MFC-sorted CAR$^+$EVs. (**D**) MFC analysis of CAR$^+$EVs concentration in: CAR-T patient's plasma (n=3), anti-CD19.CAR Ab plasma pull down (n=3), and anti-CD19.CAR Ab pull down-depleted plasma (n=3); Data are presented as boxes and whiskers; boxes show median and IQR, whiskers represent minimum and maximum values.*

Confocal microscopy analysis

CAR-T cells and iPSC-derived neural cells were prepared for imaging by cytocentrifugation onto coverslips or by seeding onto Matrigel-coated glass coverslips (Corning), respectively. Cells were fixed with 4% paraformaldehyde for 15 minutes at room temperature, washed twice with PBS, and permeabilized and blocked with 1% bovine serum albumin (BSA) in 0.1% Triton X-100 for 1 hour. Nonspecific binding sites were then saturated with 4% BSA in PBS for 20 minutes before incubation with primary-labeled or click-conjugated antibodies for 1 hour at room temperature. For CAR-T cell staining, the following reagents were used: Zenon Alexa Fluor 555 Mouse IgG1 Labeling Kit (Thermo Fisher Scientific, Cat. Z25005, RRID:AB_2736948) and Zenon Alexa Fluor 647 Human IgG Labeling Kit (Thermo Fisher Scientific, Cat. Z25408, RRID:AB_2736958). Primary antibodies included anti-perforin (clone eBioBOR21; Thermo Fisher Scientific, Cat. 14-9993-82, RRID:AB_468675), anti-CD63 (clone TS63; Thermo Fisher Scientific, Cat. 10628D, RRID:AB_2532983), anti-CD19 CAR FMC63 idiotype (clone REA1297; Miltenyi Biotec, Cat. 130-127-983), and DAPI (Thermo Fisher Scientific, Cat. 62247) for nuclear counterstaining. For iPSC-derived neural precursor cells and differentiated neurons, the following primary antibodies were used: Pax6 (Thermo Fisher Scientific, Cat. 42-6600, RRID:AB_2533534), nestin (Thermo Fisher Scientific, Cat. MA1-110, RRID:AB_2536821), NeuN (Abcam, Cat. ab190565, RRID:AB_2732785), βIII-tubulin (Abcam, Cat. ab78078, RRID:AB_2256751), and tyrosine hydroxylase (GeneTex, Cat. GTX113016, RRID:AB_1952230). After three PBS washes, samples were incubated with secondary fluorochrome-conjugated antibodies for 2 hours at room temperature: Alexa Fluor 488-conjugated goat anti-rabbit (Abcam, Cat. ab150077, RRID:AB_2630356), Alexa Fluor 555-conjugated goat anti-

mouse (Abcam, Cat. ab150114, RRID:AB_2687594), and Alexa Fluor 647-conjugated donkey anti-mouse (Abcam, Cat. ab150107, RRID:AB_2890037). Samples were then mounted using an anti-fade reagent (Molecular Probes, Life Technologies, Milan, Italy). Confocal imaging was performed on a Nikon A1R laser-scanning confocal microscope equipped with an Eclipse Ti-E inverted microscope and four laser lines (405, 488, 561, and 638 nm). Z-stacks were acquired at 0.3 µm intervals using a 100× total internal reflection fluorescence (TIRF) objective (NA 1.49). Laser power and detector gain were kept constant across all experimental sets. Image deconvolution was performed using the Richardson-Lucy algorithm, and image processing, 3D reconstruction, and colocalization analyses were carried out using NIS-Elements software (version 5.31, Nikon), as previously described (Vignoli et al., 2021). For time-lapse imaging, fluorescence image series were acquired using the same Nikon A1R system equipped with a 20× Plan Apo VC objective (NA 0.75). All experiments were conducted at 37 °C and 5% CO_2 using an OkoLab stage incubator and the Nikon Eclipse Ti-E inverted microscope with perfect focus system. Excitation was achieved using 489.1 nm and 561 nm diode lasers (set below 10% intensity) for PKH26 Red Fluorescent Cell Linker-labeled cells (Sigma-Aldrich, Cat. PKH26GL) and Sytox Green nucleic acid stain (Thermo Fisher Scientific, Cat. S7020) or eGFP, respectively. The pinhole diameter was set to 2 Airy units (59 µm) to acquire a single thick optical section through the cell center. Sequential images (1,024 × 1,024 pixels, 12-bit depth, 4,096 gray levels) were collected every 5 minutes for at least 16 hours. Transmission and fluorescence channels were merged and rendered using NIS-Elements Advanced Research software (Nikon).

STORM and combined confocal/STORM microscopy analysis

Single-molecule super-resolution imaging of the CD19.CAR antigen was performed as previously described (Pesce et al., 2022). Single-channel acquisitions were carried out on a Nikon N-STORM microscope equipped with a DU-897 EM-CCD camera (Andor Technology) and a 100× total internal reflection fluorescence (TIRF) objective (NA 1.49). Excitation was achieved using a 10 mW, 647 nm laser (CrystaLaser) operated at 80% power. For both 2D and 3D-STORM modes, 10,000

consecutive frames were collected per field at a constant TIRF angle, with frame exposures ranging between 10 and 20 milliseconds. Super-resolution image reconstruction was performed using the STORM module of the NIS-Elements software (version 5.31; Nikon). Samples were stained with Alexa Fluor 647-conjugated recombinant human CD19.CAR FMC63 idiotype antibody (Miltenyi Biotec), incubated overnight at 4 °C, and washed thoroughly with PBS. Prior to image acquisition, samples were mounted in a blinking buffer for direct STORM (dSTORM) imaging and covered with high-precision 1.5H coverslips. When combined confocal/STORM acquisition was required, the antifade mounting medium was replaced with the dSTORM buffer. Dual color dSTORM imaging was performed using an Olympus IX83 inverted microscope (Evident) equipped with a 100× TIRF objective (NA 1.5) integrated with the Abbelight SAFe MN360 platform, featuring 405 nm, 488 nm, 561 nm, and 640 nm excitation lasers (Oxxius). 19BBζ.eGFP.CAR-T cells were cytocentrifuged onto glass coverslips, fixed as described above, and stained with Alexa Fluor 568-conjugated anti-CD63 antibody (EV Profiler Kit, ONI) and Alexa Fluor 647-conjugated CD19.CAR FMC63 idiotype antibody (Miltenyi Biotec). Multicolor dSTORM acquisition was conducted with 640 nm (300 mW) and 561 nm (165 mW) laser lines for 10,000 frames per acquisition at a fixed HiLo illumination angle and 50 ms exposure time. The eGFP signal was acquired as a wide-field channel using 488 nm excitation (40 mW, 500 ms exposure). For EV imaging, both $eGFP^+$ and $eGFP^-$ vesicles were captured on tetraspanin antibody-coated coverslips using the Smart EV Kit protocol (Abbelight). $eGFP^+$ EVs were stained with a pool of Alexa Fluor 647-conjugated anti-CD63, anti-CD9, and anti-CD81 antibodies (Abbelight) and imaged in monochromatic 2D-STORM mode (640 nm laser at 300 mW; 405 nm laser gradient from 0-40 mW across 10,000 frames, 50 ms exposure per frame, constant HiLo illumination angle). Plasma-derived CAR^+EVs were labeled with Alexa Fluor 647-conjugated anti-CD19.CAR FMC63 idiotype antibody (Miltenyi Biotec) and CF680-conjugated anti-CD63 recombinant antibody (clone EPR21151, Abcam) and analyzed using spectral-demixing dSTORM (640 nm, 300 mW; 405 nm, gradient 0-40 mW; dichroic T700; 10,000 frames; 50 ms exposure). Single-molecule blinking sequences were super-localized using NEO_analysis software (Abbelight) to generate coordinate-based super-resolution datasets. Channel alignment and spectral-demixing corrections were performed within NEO_analysis. Segmentation of single EVs was conducted using the DBSCAN

algorithm in NEO_analysis. EV sizing and color classification were performed using custom Python scripts.

ExoView platform analysis

EVs derived from patient plasma, infusion bag leftovers (BLs), and SmartSEC column-purified fractions were analyzed using the ExoView platform (NanoView Biosciences, Boston, MA, USA) following the manufacturer's protocol. EV immunocapture and phenotyping were performed with the following antibodies: recombinant human PE-conjugated anti-CD19 CAR FMC63 idiotype antibody (Miltenyi Biotec); fluorochrome-conjugated anti-human antibodies CD107a-APC-H7 (clone H4A3, BD Biosciences, Cat. 561343, RRID:AB_10644020) and perforin-Alexa Fluor 647 (clone δG9, BioLegend, Cat. 308110, RRID:AB_493254); and tetraspanin antibodies CD9-Alexa Fluor 488, CD81-Alexa Fluor 555, and CD63-Alexa Fluor 647 (NanoView Biosciences). In addition, recombinant human CD19 Fc Chimera Alexa Fluor 647 protein (Bio-Techne, Cat. AFR9269) and Alexa Fluor 488-conjugated wheat germ agglutinin (Invitrogen, Thermo Fisher Scientific) were employed. All analyses were performed using the ExoView R200 reader equipped with the ExoView Scanner software (version 3.0; NanoView Biosciences) according to the manufacturer's instructions.

Nanoparticle Tracking Analysis (NTA) of EVs

Extracellular vesicle (EV) size distribution and concentration were measured by Nanoparticle Tracking Analysis (NTA) using the NanoSight NS300 system (Malvern Panalytical, Malvern, UK). Samples were diluted 1:100 in 0.1 µm-filtered PBS prior to measurement. Data acquisition was performed at a constant syringe pump flow rate of 30. For each sample, three 60-second videos were recorded and analyzed to obtain the mean particle size and concentration (particles/mL). Data processing was performed using NTA software version 3.2.

Statistical analysis

Descriptive statistics were generated for the entire study population as appropriate. All tests were two-tailed, and p values <0.05 were considered statistically significant. Associations between clinical or laboratory variables and ICANS occurrence were evaluated using Pearson's χ^2 test for categorical variables, the Mann-Whitney U test for non-normally distributed continuous variables, and one-way ANOVA for normally distributed data. Variables significantly associated with ICANS ($P \leq 0.05$) were further analyzed using multivariable logistic regression models. For longitudinal analyses, Student's t test was applied to log-transformed fold-change (logFC) values at each time point, with significance determined after Benjamini-Hochberg correction for multiple comparisons. Paired or one-sample t tests were used when appropriate. Median time to CAR^+T-cell expansion peak (TTP) was estimated using the Kaplan-Meier method. Correlations among quantitative variables were assessed using either Spearman's or Pearson's correlation coefficients, as appropriate. Colocalization analyses from confocal and STORM microscopy were quantified using Manders' overlap coefficient, as previously described (Riccio et al., 2004). All statistical analyses were performed using SPSS (IBM Corp.; RRID:SCR_002865), GraphPad Prism (Dotmatics; RRID:SCR_002798), and R software, freely available from the Comprehensive R Archive Network (r-project.org).

Study approval

The study was approved by the institution: Comitato Etico di Area Vasta Emilia Centro della Regione Emilia-Romagna (approval 319/2021/Sper/AOUBo and EM714-2022_319/2021/Sper/AOUBo).

RESULTS

Patient's characteristics

This study enrolled 100 patients with relapsed/refractory B-NHL (**Table 1**) and a median age of 60 years (19-76). Lymphoma subtypes were distributed as follows: 67 (67%) Diffuse Large B-Cell Lymphoma (DLBCL or transformed-DLBCL), 12 (12%) Primary Mediastinal B-Cell Lymphoma (PMBCL), 6 (6%) High-Grade B-Cell Lymphoma (HGBCL), 1 (1%) Grey Zone Lymphoma (GZL), and 14 (14%) Mantle Cell Lymphoma (MCL). Regarding CAR-T products, 28 patients (28%) received tisa-cel, 58 (58%) axi-cel, and 14 (14%) brexu-cel, following a median of 3 prior treatment lines (1-11). No patient had CNS involvement at the time of CD19.CAR-T cell infusion. All patients received standard lymphodepleting chemotherapy with cyclophosphamide (250-500 mg/m²/day) and fludarabine (25-30 mg/m²/day) administered intravenously on days -5, -4, and -3, before CAR-T cell infusion, and according to institutional practice.

Baseline characteristics		**Total (n=100)**
Age, median (range)		60 years (19-76)
Sex, n (%)	Female	33 (33)
	Male	67 (67)
ECOG, n (%)	0	85 (85)
	≥ 1	15 (15)
BMI, n (%)	< 25	47 (47)
	≥ 25	53 (53)
Disease characteristics		
Diagnosis, n (%)	DLBCL	44 (44)
	t-DLBCL	23 (23)
	PMBCL	12 (12)
	HGBCL	6 (6)
	GZL	1 (1)
	MCL	14 (14)
Disease status, n (%)	PD	62 (62)

	NO PD (CR/PR/SD)	38 (38)
Prior therapies		
Previous therapies, median (range)		3 (1-11)
Previous ASCT, n (%)	Yes	31 (31)
	No	69 (69)
Bridging therapy, n (%) *		81 (81)
	Chemo-based	25 (25)
	Steroids	16 (16)
	Radiotherapy	12 (12)
	Immune Checkpoint Inhibitors	9 (9)
	BTKi	7 (7)
CAR-T cell therapy		
CAR-T cell product, n (%)	Tisa-cel	28 (28)
	Axi/Brexu-cel	72 (72)
CAR-T cells, median × 10^6/kg (range)		2.00 (1.96 - 5.92)
Toxicities		
CRS	Grade 0-1	72 (72)
	Grade ≥2	28 (28)
ICANS	Grade 0	71 (71)
	Grade 1	9 (9)
	Grade 2	10 (10)
	Grade 3	5 (5)
	Grade 4	3 (3)
	Grade 5	2 (2)

Table 1. Patient's characteristics. **23 patients underwent miscellaneous bridging therapies. ASCT: autologous stem cell transplantation; BMI: body mass index; BTKi: Bruton tyrosine kinase inhibitors; CR: complete response; CRS: cytokine release syndrome; DLBCL: diffuse large B-cell lymphoma; ECOG: Eastern Cooperative Oncology Group performance scale; GZL: grey zone lymphoma; HGBCL: high grade B-cell lymphoma; ICANS: immune effector cell-associated neurotoxicity syndrome; MCL: mantle cell lymphoma; PD: progressive disease; PMBCL: primary*

mediastinal B-cell lymphoma; PR: partial response; SD: stable disease; t-DLBCL: transformed diffuse large B-cell lymphoma.

CRS after CD19.CAR-T cell infusion

CRS of any grade occurred in 90 patients (90%), with 28 patients (28%) experiencing grade ≥2 CRS; no fatal CRS events were reported (**Table 2**). The median time to CRS onset was 1 day (0-11) after infusion. CRS was managed with tocilizumab as first-line therapy according to Hayden et al., 2022. In univariate analyses, only the CAR-T product (CD28-based costimulation) was significantly associated with CRS (p=0.045; see **Table 2**).

Baseline characteristics		**Total (n=100)**	**NO CRS (n=10)**	**CRS (n=90)**	**p value**
Age, median (range)		60 years (19-76)	63.5 years (27-70)	59 years (19-76)	0.196
Sex, n (%)	Female	33 (33)	2 (20)	31 (34)	0.571
	Male	67 (67)	8 (80)	59 (66)	
ECOG, n (%)	0	85 (85)	10 (100)	75 (83)	0.351
	≥ 1	15 (15)	0 (0)	15 (17)	
BMI, n (%)	< 25	47 (47)	3 (30)	44 (49)	0.423
	≥ 25	53 (53)	7 (70)	46 (51)	
PLD LDH, median (range)		220 (76 - 8,365)	201 (155 - 389)	220.5 (76 - 8,365)	0.498
PLD CRP, median (range)		0.425 (0.02 - 22.93)	0.37 (0.10 - 2.29)	0.44 (0.02 - 22.93)	0.667
PLD Ferritin, median (range)		191 (8 - 7,493)	168 (13 - 1,538)	196 (8 - 7,493)	0.913
Disease characteristics					
Diagnosis, n (%)	DLBCL	44 (44)	4 (40)	40 (44)	1.000
	t-DLBCL	23 (23)	5 (50)	18 (20)	0.081
	PMBCL	12 (12)	0 (0)	12 (13)	0.473
	HGBCL	6 (6)	0 (0)	6 (7)	0.888
	GZL	1 (1)	0 (0)	1 (1)	1.000
	MCL	14 (14)	1 (10)	13 (15)	1.000
Disease status, n (%)	PD	62 (62)	5 (50)	57 (63)	0.631
	NO PD (CR/PR/SD)	38 (38)	5 (50)	33 (37)	
Prior therapies					
Previous therapies, median (range)		3 (1-11)	3 (2-11)	3 (1-7)	0.073

Previous ASCT, n (%)	Yes	31 (31)	5 (50)	26 (29)	0.313
	No	69 (69)	5 (50)	64 (71)	
Bridging therapy, n (%) *		81 (81)	7 (70)	74 (82)	0.610
	Chemo-based	25 (25)	5 (50)	20 (22)	0.124
	Steroids	16 (16)	0 (0)	16 (18)	0.317
	Radiotherapy	12 (12)	0 (0)	12 (13)	0.473
	Immune Checkpoint Inhibitors	9 (9)	0 (0)	9 (10)	0.641
	BTKi	7 (7)	1 (10)	6 (7)	1.000
CAR-T cell therapy					
CAR-T cell product, n (%)	Tisa-cel	28 (28)	6 (60)	22 (24)	**0.045**
	Axi/Brexu-cel	72 (72)	4 (40)	68 (76)	

Table 2. CRS after CD19.CAR-T cell infusion. **23 patients underwent miscellaneous bridging therapies. ASCT: autologous stem cell transplantation; BMI: body mass index; BTKi: Bruton tyrosine kinase inhibitors; CR: complete response; CRP: C-reactive protein; CRS: cytokine release syndrome; DLBCL: diffuse large B-cell lymphoma; ECOG: Eastern Cooperative Oncology Group performance scale; GZL: grey zone lymphoma; HGBCL: high grade B-cell lymphoma; LDH: lactate dehydrogenase; MCL: mantle cell lymphoma; PD: progressive disease; PLD: pre-lymphodepletion; PMBCL: primary mediastinal B-cell lymphoma; PR: partial response; SD: stable disease; t-DLBCL: transformed diffuse large B-cell lymphoma.*

ICANS after CD19.CAR-T cell infusion

Within 30 days of CD19.CAR-T cell infusion, ICANS of any grade (G) occurred in 29 of 100 patients (29%). Specifically, 9 patients (9%) developed G1 ICANS, 10 (10%) G2, 5 (5%) G3, 3 (3%) G4, and 2 (2%) experienced G5 ICANS with exitus due to diffuse cerebral edema (**Table 3**). The median time to ICANS onset was 5 days (3-13). All ICANS events occurred either concurrently with or after CRS, with a median interval of 4 days (0-11) between CRS and ICANS onset. The most common manifestation was encephalopathy (93%), with ideomotor slowing, inattention, disorientation, dyscalculia, and confusion. Frequently, encephalopathy displayed a frontal pattern (63%) characterized by motor, verbal and written perseveration (e.g., palilalia and paligraphia). Language disturbances (dysarthria and aphasia) were also common (69%); similarly nonspecific ICANS features were frequently observed, including postural tremor (83%) and headache (34%). One G4 and two G5 ICANS onset were marked by severe headache and vomiting due to intracranial hypertension, rapidly progressing to coma within hours. Contrast-enhanced brain MRI was performed in 25 of 29 ICANS patients (86%): no abnormalities were identified in 18 cases (72%); 7 patients (28%) displayed new radiologic findings, including focal cerebral edema with leptomeningeal enhancement (n=3), focal intraparenchymal and subarachnoid hemorrhage (n=1), and diffuse cerebral edema (n=3). Diffuse slowing of background activity was revealed by electroencephalography in nearly all ICANS patients (93%), while epileptiform abnormalities in the absence of clinical seizures were detected in 4 patients (14%). According to local protocols, ICANS management included high-dose corticosteroids as first-line treatment (dosage and duration according to Hayden et al., 2022); siltuximab and anakinra were administered in cases of G≥3; ICANS resolution was achieved in all patients except for G5 events (n=2; 7%). ECOG performance status >1, disease subtype (PMBCL), progressive disease at infusion, bridging therapy with immune checkpoint inhibitors, and G≥2 CRS were found to be associated with ICANS in univariate analysis (**Table 3**). ECOG >1 (OR=4.42; 95% CI, 1.10-19.19; p=0.038), PMBCL histology (OR=51.19; 95% CI, 6.93-1123.76; p=0.001), progressive disease at infusion (OR=10.23; 95% CI, 1.84-192.19; p=0.03), and G≥2 CRS (OR=4.55; 95% CI, 1.49-14.58; p=0.008) resulted independent clinical risk factors for ICANS also in multivariate analysis.

Baseline characteristics		**Total (n=100)**	**NO ICANS (n=71)**	**ICANS (n=29)**	**p value**
Age, median (range)		60 years (19-76)	60 years (21-76)	56 years (19-70)	0.445
Sex, n (%)	Female	33 (33)	19 (27)	14 (48)	0.065
	Male	67 (67)	52 (73)	15 (52)	
ECOG, n (%)	0	85 (85)	65 (92)	20 (69)	**0.01**
	≥ 1	15 (15)	6 (8)	9 (31)	
BMI, n (%)	< 25	47 (47)	29 (41)	18 (62)	0.087
	≥ 25	53 (53)	42 (59)	11 (38)	
Disease characteristics					
Diagnosis, n (%)	DLBCL	44 (44)	36 (51)	8 (28)	0.058
	t-DLBCL	23 (23)	19 (27)	4 (14)	0.256
	PMBCL	12 (12)	3 (4)	9 (31)	**0.001**
	HGBCL	6 (6)	3 (4)	3 (10)	0.481
	GZL	1 (1)	0 (0)	1 (3)	0.642
	MCL	14 (14)	10 (14)	4 (14)	1.000
Disease status, n (%)	PD	62 (62)	39 (55)	23 (79)	0.04
	NO PD (CR/PR/SD)	38 (38)	32 (45)	6 (21)	
Prior therapies					
Previous therapies, median (range)		3 (1-11)	2 (1-11)	3 (2-6)	0.217
Previous ASCT, n (%)	Yes	31 (31)	20 (28)	11 (38)	0.472
	No	69 (69)	51 (72)	18 (62)	
Bridging therapy, n (%) *		81 (81)	58 (82)	23 (79)	1.000
	Chemo-based	25 (25)	19 (27)	6 (21)	0.703
	Steroids	16 (16)	9 (13)	7 (24)	0.264
	Radiotherapy	12 (12)	8 (11)	4 (14)	0.989
	Immune Checkpoint Inhibitors	9 (9)	3 (4)	6 (21)	**0.026**
	BTKi	7 (7)	5 (7)	2 (7)	1.000
CAR-T cell therapy					
CAR-T cell product, n (%)	Tisa-cel	28 (28)	22 (31)	6 (21)	0.427
	Axi/Brexu-cel	72 (72)	49 (69)	23 (79)	

CAR-T cells, median × 10^6/kg (range)		2.00 (1.96 - 5.92)	2.00 (1.96 - 5.92)	2.00 (2.00 - 5.10)	0.401
Toxicities					
CRS	Grade 0-1	72 (72)	60 (85)	12 (41)	**0.00004**
	Grade ≥2	28 (28)	11 (15)	17 (59)	
ICANS	Grade 0	71 (71)	71 (100)	/	
	Grade 1	9 (9)	/	9 (31)	
	Grade 2	10 (10)	/	10 (35)	
	Grade 3	5 (5)	/	5 (17)	
	Grade 4	3 (3)	/	3 (10)	
	Grade 5	2 (2)	/	2 (7)	

Table 3. ICANS after CD19.CAR-T cell infusion. **23 patients underwent miscellaneous bridging therapies. ASCT: autologous stem cell transplantation; BMI: body mass index; BTKi: Bruton tyrosine kinase inhibitors; CR: complete response; CRP: C-reactive protein; CRS: cytokine release syndrome; DLBCL: diffuse large B-cell lymphoma; ECOG: Eastern Cooperative Oncology Group performance scale; GZL: grey zone lymphoma; HGBCL: high grade B-cell lymphoma; LDH: lactate dehydrogenase; MCL: mantle cell lymphoma; PD: progressive disease; PLD: pre-lymphodepletion; PMBCL: primary mediastinal B-cell lymphoma; PR: partial response; SD: stable disease; t-DLBCL: transformed diffuse large B-cell lymphoma.*

CAR$^+$T cell and CAR-DNA expansion kinetics

Over the first 30 days following infusion, CD19.CAR-T cell expansion was evaluated using two different approaches: quantification of circulating CAR$^+$T cells by multiparameter flow cytometry (MFC) and CAR-specific DNA (CAR-DNA) copies by droplet digital PCR (ddPCR) (**Figure 1A**). The expansion peak, expressed as median values, reached 57 CAR$^+$T cells/μL (8-1,279) of peripheral blood and 44,167 CAR-DNA copies/mL (950-1,105,000), respectively (**Figure 1B**). When the kinetics were integrated over the 30-day period, the calculated median $AUC_{0\text{-}30}$ amounted to 654 CAR$^+$T cells/μL×days (104-15,997) and 388,881 CAR-DNA copies/mL×days (7,673-12,096,513) (**Figure 1C**). The time to expansion peak (TTP) differed between the two methods, with CAR$^+$T cells peaking at a median of 13 days (7-30) and CAR-DNA copies at 9 days (3-21) (**Figure 1D**). Most expansion parameters did not differ significantly between patients stratified for ICANS occurrence: median CAR$^+$T cells at expansion peak were 81 versus 54 cells/μL (**Figure 1E**), and median $AUC_{0\text{-}30}$ values were 688 versus 620 CAR$^+$T cells/μL×days (**Figure 1F**) in ICANS versus NO ICANS patients, respectively. However, a difference emerged in the TTP, significantly shorter in ICANS patients, with CAR$^+$T cells reaching their peak as early as day +7 (7-13) compared with a median of day +13 (7-30) in NO ICANS ones (**Figure 1G**). The ddPCR results mirrored those obtained by MFC, confirming similar CAR-DNA peak and $AUC_{0\text{-}30}$ values across the two subgroups. Specifically, the expansion peak was 87,413 copies/mL in ICANS patients versus 37,000 in NO ICANS ones (**Figure 1H**), and $AUC_{0\text{-}30}$ values were almost identical (388,530 vs 389,231 copies/mL×days; **Figure 1I**). Once again, the most evident distinction was the shorter TTP in ICANS, with CAR-DNA peak at day +7 (5-11) compared with day +11 (3-21) in NO ICANS (**Figure 1J**). Analyzing the overall kinetics, on day +7, both CAR$^+$T cells and CAR-DNA copies were markedly elevated in ICANS patients compared with NO ICANS (81 vs 15 CAR$^+$T cells/μL, **Figure 1K**; 87,413 vs 4,500 CAR-DNA copies/mL, **Figure 1L**). Intriguingly, an opposite trend was observed on day +1, when CAR-DNA copies were significantly lower in patients who would later develop ICANS compared to their counterparts (0 vs 57 CAR-DNA copies/mL; **Figure 1M**). Since CAR-DNA values measured as early as 1 hour after infusion did not differ between groups (**Figure 1L**), the drop at 24 hours strongly suggested a more rapid trafficking of CD19.CAR-T cells into tumor sites and/or peripheral tissues, possibly including the CNS. Taken

together, these observations indicate that the accelerated kinetics of CD19.CAR-T cell expansion in patients who develop ICANS are likely a consequence of earlier tissue homing and activation, marked by the abrupt decrease in circulating CAR-DNA copies at day +1.

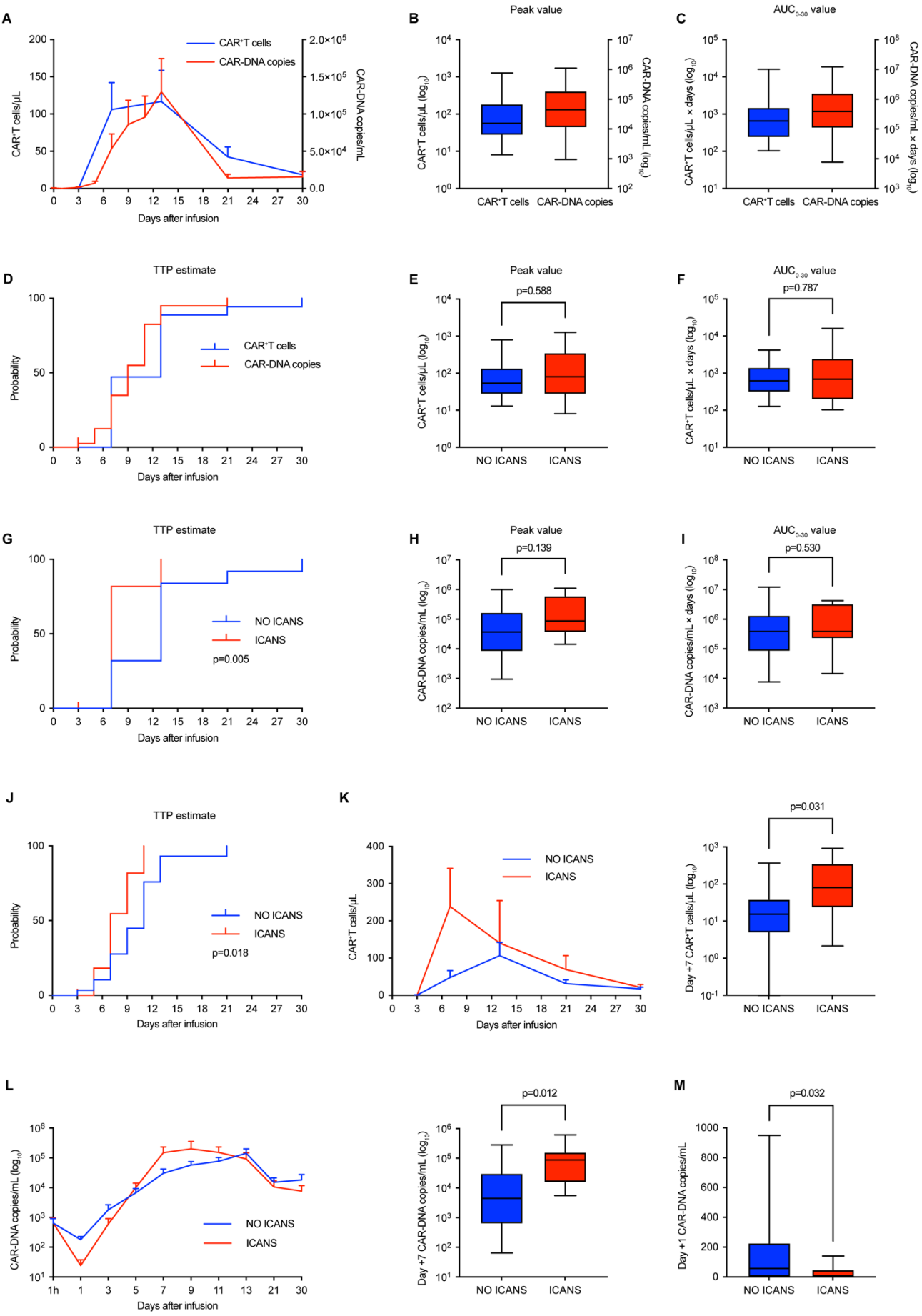
A
CAR+T cells
CAR-DNA copies
CAR+T cells/μL
CAR-DNA copies/mL
Days after infusion
B
Peak value
CAR+T cells/μL (log10)
CAR-DNA copies/mL (log10)
CAR+T cells
CAR-DNA copies
C
AUC0-30 value
CAR+T cells/μL × days (log10)
CAR-DNA copies/mL × days (log10)
CAR+T cells
CAR-DNA copies
D
TTP estimate
Probability
CAR+T cells
CAR-DNA copies
Days after infusion
E
Peak value
p=0.588
CAR+T cells/μL (log10)
NO ICANS
ICANS
F
AUC0-30 value
p=0.787
CAR+T cells/μL × days (log10)
NO ICANS
ICANS
G
TTP estimate
Probability
NO ICANS
ICANS
p=0.005
Days after infusion
H
Peak value
p=0.139
CAR-DNA copies/mL (log10)
NO ICANS
ICANS
I
AUC0-30 value
p=0.530
CAR-DNA copies/mL × days (log10)
NO ICANS
ICANS
J
TTP estimate
Probability
NO ICANS
ICANS
p=0.018
Days after infusion
K
NO ICANS
ICANS
CAR+T cells/μL
Days after infusion
p=0.031
Day +7 CAR+T cells/μL (log10)
NO ICANS
ICANS
L
CAR-DNA copies/mL (log10)
NO ICANS
ICANS
1h
Days after infusion
p=0.012
Day +7 CAR-DNA copies/mL (log10)
NO ICANS
ICANS
M
p=0.032
Day +1 CAR-DNA copies/mL
NO ICANS
ICANS

Figure 1. Kinetics of peripheral blood CAR$^+$T cells and CAR-DNA copies in CAR-T cell-infused patients. *(**A**) Peripheral blood kinetics of CAR$^+$T cells (n=37) and CAR-DNA copies (n=41), assessed by MFC and ddPCR, respectively (mean ± SEM). (**B**) Expansion peak values of CAR$^+$T cells (n=36) and CAR-DNA copies (n=40). (**C**) AUC_{0-30} value estimates for CAR$^+$T cells (n=36) and CAR-DNA copies (n=40). (**D**) Kaplan-Meier (KM) estimate of time to peak (TTP) for CAR$^+$T cells (n=37) and CAR-DNA copies (n=41). (**E**) CAR$^+$T cell expansion peak values in NO ICANS (n=25) versus ICANS (n=11); Mann-Whitney (MW) test. (**F**) CAR$^+$T cell AUC_{0-30} value estimate in NO ICANS (n=25) versus ICANS (n=11); MW test. (**G**) KM estimate of CAR$^+$T cell TTP in NO ICANS (n=25) versus ICANS (n=12); log-rank test. (**H**) Expansion peak values of CAR-DNA copies in NO ICANS (n=29) versus ICANS (n=11); MW test. (**I**) AUC_{0-30} value estimates for CAR-DNA copies in NO ICANS (n=29) versus ICANS (n=11); MW test. (**J**) KM estimate of TTP for CAR-DNA copies in NO ICANS (n=29) versus ICANS (n=12); log-rank test. (**K**) Peripheral blood kinetics of CAR$^+$T cells (mean ± SEM) in NO ICANS (n=25) versus ICANS (n=12), and day +7 CAR$^+$T cells in NO ICANS (n=25) versus ICANS (n=11); MW test. (**L**) Kinetics of CAR-DNA copies (mean ± SEM) in NO ICANS (n=29) versus ICANS (n=12), and day +7 CAR-DNA copies in NO ICANS (n=29) versus ICANS (n=7); MW test. (**M**) Day +1 CAR-DNA copies in NO ICANS (n=29) versus ICANS (n=12); MW test. Unless otherwise indicated, data are presented as boxes and whiskers; boxes show median and interquartile range (IQR), and whiskers represent minimum and maximum values.*

Key role of IL-15 and CX3CL1 in CD19.CAR-T cell tissue trafficking and activation

Building on these findings, two soluble mediators of interest were next examined: interleukin-15 (IL-15), a γ-chain cytokine previously reported to be implicated in CAR-T cell-related neurotoxicity (Gust et al., 2020; Siegler et al., 2020), and CX3CL1 (fractalkine), a membrane-bound and soluble chemokine known to orchestrate the recruitment of $CX3CR1^{+}CD8^{+}$ T lymphocytes within tissues (Zander et al., 2019). Plasma levels of both molecules were quantified at day +1 post-infusion: patients who later developed ICANS exhibited significantly higher median concentrations of IL-15 (33 vs 26 pg/mL) and, more strikingly, of CX3CL1 (2,869 vs 1,344 pg/mL) compared to NO ICANS patients (**Figures 2A-B**). Moreover, IL-15 and CX3CL1 levels were strongly correlated at this early time point ($r=0.653$, $p=0.00007$), and both also associated with multiple biomarkers mirroring systemic inflammation and/or disease burden such as low platelet count (PLTs), elevated fibrinogen (FBG), lactate dehydrogenase (LDH), ferritin (FER), C-reactive protein (CRP), cell-free DNA (cfDNA), growth differentiation factor 15 (GDF15), CXCL9, and neurofilaments (NFL), measured either at pre-lymphodepletion (PLD) time point or at day +1 (**Figures 2C-D**). Several of these parameters have already been reported to be associated with CAR-T cell-related toxicities and poor response. The source of IL-15 elevation is multifactorial and, beyond its canonical role in T-cell and NK-cell homeostasis, it can be induced by prior chemotherapy (Innamarato et al., 2020). Indeed, significantly higher median levels of IL-15 at day +1 was observed in patients who received chemo-based bridging therapy (33 vs 26 pg/mL), whereas CX3CL1 values did not vary according to this variable (**Figures 2E-F**). To further explore the contribution of the CX3CL1 axis in CD19.CAR-T cell biology, the expression of its receptor, CX3CR1, was characterized on engineered T-cells. Flow cytometric analysis revealed marked heterogeneity of CX3CR1 surface expression among both 19BBζ.CAR-T cells generated from healthy donors (n=3) and Bag Leftovers (BL; n=9) available (**Figure 2G**). Importantly, coculture experiments demonstrated a rapid upregulation of CX3CR1 readily after 1 hour when 19BBζ.CAR-T cells were exposed to $CD19^{+}$K562 target cells, but not when cultured with $CD19^{-}$K562 cells (**Figure 2H**). In the clinical setting, longitudinal monitoring confirmed a robust increase in CX3CR1 expression on CAR^{+}T cells at day +7 in a patient who developed ICANS, whereas no induction was observed in three individuals without neurotoxicity (**Figure 2I**).

Given that the CX3CL1/CX3CR1 interaction represents a well-established neurotropic signaling pathway (Limatola et al., 2014; Lee et al., 2018), these findings support the hypothesis that activated CD19.CAR-T cells may be preferentially recruited to the central nervous system and to peripheral sites characterized by CX3CL1 release. Collectively, these results define the key role of CX3CL1/CX3CR1 axis in CD19.CAR-T cell trafficking and tissue homing, and in ICANS pathogenesis.

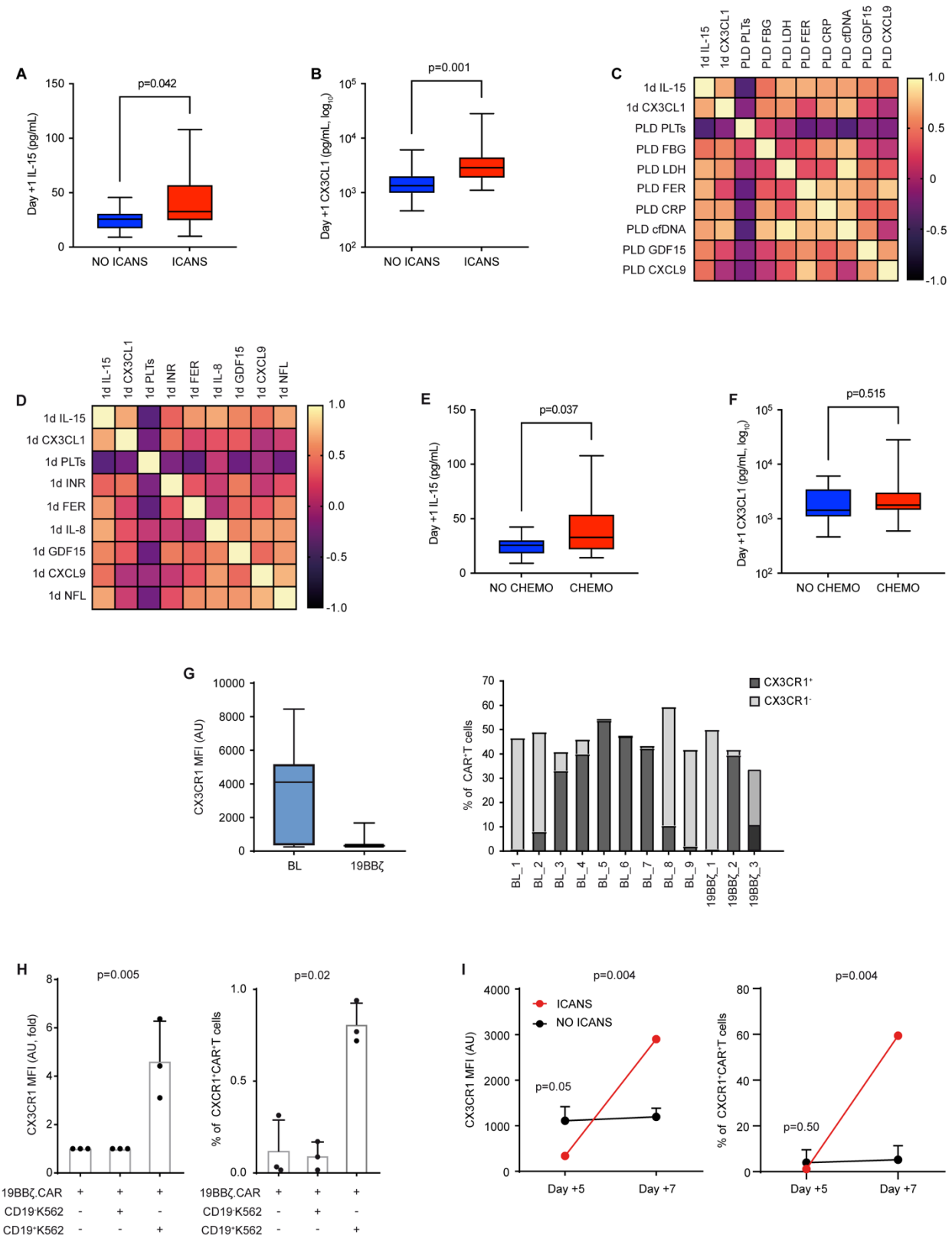

Figure 2. IL-15 and CX3CL1/CX3CR1 interplay in ICANS and NO ICANS patients. *(**A**) Day +1 IL-15 plasma levels in NO ICANS (n=21) versus ICANS (n=11); MW test. (**B**) Day +1 CX3CL1 plasma levels in NO ICANS (n=36) versus ICANS (n=17); MW test. (**C** and **D**) Heatmaps (Pearson's r coefficients) of day +1 (1d) IL-15 and CX3CL1 plasma levels and biochemical profile at pre-*

*lymphodepletion (PLD) (**C**) and 1d (**D**). (**E**) Day +1 IL-15 plasma levels in patients treated with chemotherapy as bridging therapy (CHEMO, n=13) versus others (NO CHEMO, n=19); MW test. (**F**) Day +1 plasma CX3CL1 in NO CHEMO (n=36) versus CHEMO (n=17); MW test. (**G-I**) CX3CR1 mean fluorescence intensity (MFI) and percentage of CX3CR1^{+} cells in bag leftover (BL, n=9) and 19BBζ.CAR-T cells (n=3) (**G**), 19BBζ.CAR-T cells cocultured with CD19^{+} or CD19^{-}K562 cells (n=3) for 1 hour (logFC t test and paired t test; mean ± SD) (**H**), and day +5 and day +7 peripheral blood CD19.CAR-T cells in ICANS (n=1) and NO ICANS (n=3, 1-sample t test; mean ± SD) (**I**). Unless otherwise indicated, data are presented as boxes and whiskers; boxes show median and IQR, and whiskers represent minimum and maximum values.*

In vitro CD19.CAR-T cell activation and CAR$^+$ extracellular vesicle release

The findings described above indicate that ICANS may stem, at least in part, from the early trafficking and activation of CD19.CAR-T cells readily after the infusion. Since post-infusion tumor biopsies from patients treated with CD19-directed CAR-T cells are rarely available in routine clinical practice, a circulating readout of in vivo CAR-T cell activation upon target engagement was investigated. To this end, the potential release of extracellular vesicles (EVs) that carry the chimeric antigen receptor (CAR$^+$EVs), by CD19.CAR-T cells, after CD19$^+$ target engagement, was hypothesized; moreover, if detectable in biofluids, their role as biomarkers of CAR-T cell trafficking and activity was postulated. To validate this hypothesis, both 19BBζ.CAR-T cells (n=4) and their fluorescent counterparts 19BBζ.eGFP.CAR-T cells (n=3) were generated and cultured either in the absence or in the presence of CD19$^+$ target cells (**Figures 3A-C**). The release of CAR$^+$EVs into cell-free supernatants was evaluated using MFC, relying either on direct eGFP fluorescence detection or on immunostaining with antibodies specific for the extracellular domain of the CD19.CAR construct (**Figure 3D**). In both systems, a marked and consistent increase in CAR$^+$EV concentration was observed following coculture with CD19$^+$ target cells, becoming evident within 1-4 hours (**Figures 3E-F**). High-resolution imaging confirmed these findings: combined wide-field and stochastic optical reconstruction microscopy (STORM) analysis of supernatants from 19BBζ.eGFP.CAR-T cocultures revealed the presence of putative vesicles (eGFP$^+$CAR$^+$EVs) captured on slides coated with antibodies recognizing canonical tetraspanins (CD63, CD9, CD81; **Figure 4A**). Likewise, 2D-/3D-STORM imaging of EVs derived from 19BBζ.CAR-T cell supernatants captured on poly-L-lysine-coated slides confirmed the presence of CD19.CAR protein on vesicular membranes (**Figures 4B-C**). Further ultrastructural investigation by combined confocal and STORM microscopy (**Figure 4D**) demonstrated a high density of CAR$^+$ vesicles within the cytoplasm of 19BBζ.CAR-T cells (**Figure 4E**). Further analyses showed that the majority of CD19.CAR protein was colocalized with CD63 tetraspanin (**Figures 4F-G**); of note, a similar distribution pattern was observed for Perforin (PRF1, **Figures 5A-B**). Altogether, these findings indicate that CD19.CAR-T cells harbor a substantial cytoplasmic reservoir of CD19.CAR protein within CD63$^+$ vesicular compartments, rapidly mobilized and released as CAR$^+$EVs after specific antigen engagement. This antigen-dependent release

provides a mechanistic basis for the detection of CAR^+EVs in extracellular biofluids and supports their potential use as a minimally invasive biomarker of CD19.CAR-T cell activation upon target engagement after tissue and tumor trafficking.

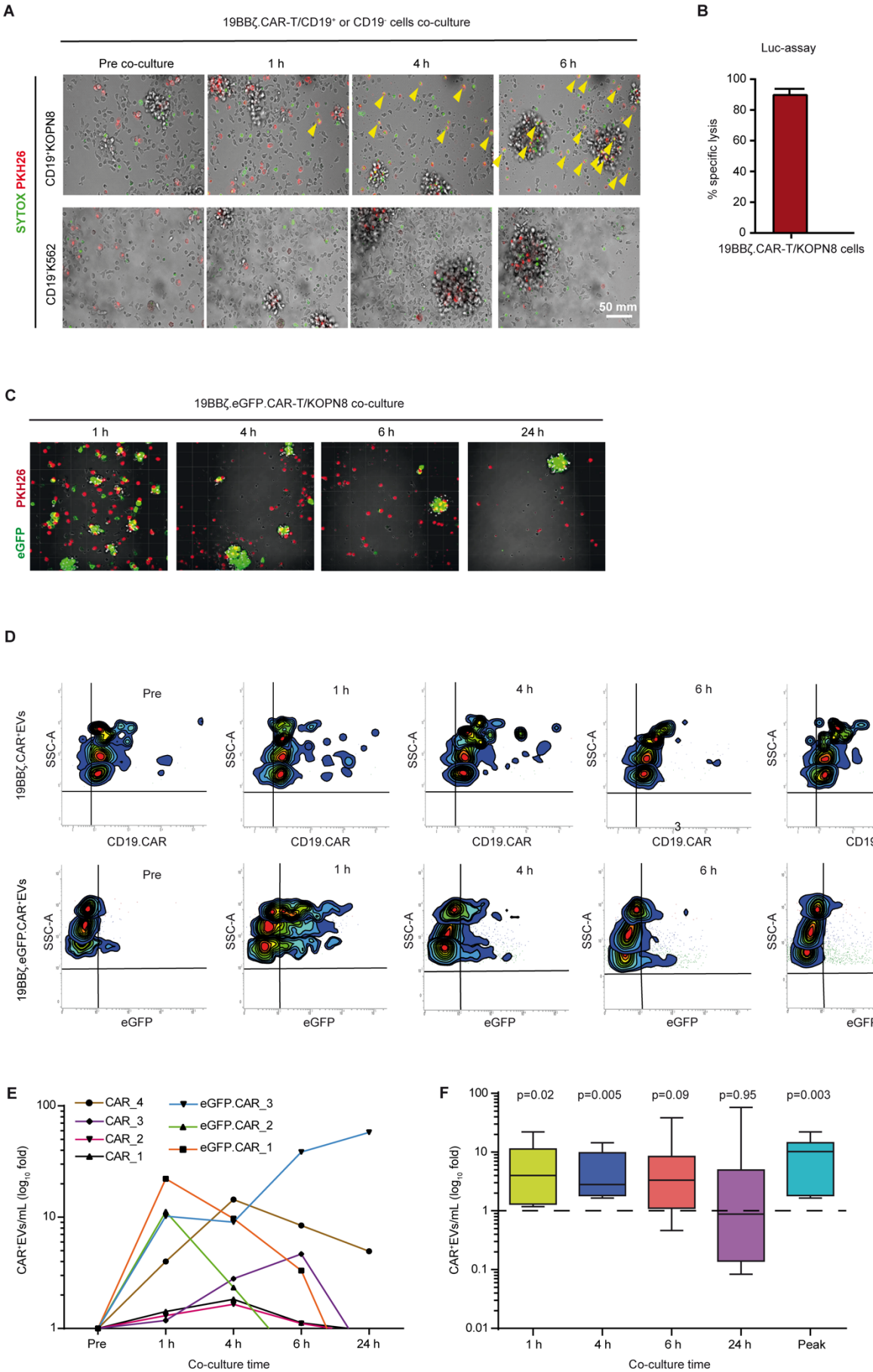
A
19BBζ.CAR-T/CD19+ or CD19- cells co-culture
Pre co-culture
1 h
4 h
6 h
SYTOX PKH26
CD19+KOPN8
CD19-K562
50 mm
B
Luc-assay
% specific lysis
100
80
60
40
20
0
19BBζ.CAR-T/KOPN8 cells
C
19BBζ.eGFP.CAR-T/KOPN8 co-culture
1 h
4 h
6 h
24 h
PKH26
eGFP
D
19BBζ.CAR+EVs
19BBζ.eGFP.CAR+EVs
SSC-A
CD19.CAR
eGFP
Pre
1 h
4 h
6 h
24 h
E
CAR_4
CAR_3
CAR_2
CAR_1
eGFP.CAR_3
eGFP.CAR_2
eGFP.CAR_1
CAR+EVs/mL (log10 fold)
Co-culture time
F
p=0.02
p=0.005
p=0.09
p=0.95
p=0.003
Peak

Figure 3. MFC analysis of CAR$^+$EVs released in vitro in coculture supernatants of 19BBζ.CAR-T or 19BBζ.eGFP.CAR-T cells with CD19$^+$ target cells. *(**A**) Representative pictures of 19BBζ.CAR-T cells cocultured with CD19$^+$KOPN8 or CD19$^-$K562 cells at different time points. Yellow arrowheads indicate dead cells. (**B**) Luciferase assay of 19BBζ.CAR-T cells-induced cell death in CD19$^+$KOPN8 cells after 24 hours of coculture (n=3, mean ± SD). (**C**) Movie snapshot of 19BBζ.eGFP.CAR-T cells cocultured with PKH26-stained CD19$^+$KOPN8 cells at different time points. (**D**) MFC analysis of supernatants from 19BBζ.CAR-T or 19BBζ.eGFP.CAR-T cells and CD19$^+$KOPN8 cells cocultures. (**E**) CAR$^+$EV kinetics for each coculture (19BBζ.CAR-T cells, n=4; 19BBζ.eGFP.CAR-T cells, n=3). (**F**) CAR$^+$EVs in 19BBζ.CAR-T and 19BBζ.eGFP.CAR-T cell cocultures (n=7) at different time points and at peak level (logFC t test; p values ≤0.02 were considered significant according to Benjamini-Hochberg correction for multiple comparisons). Unless otherwise indicated, data are presented as boxes and whiskers; boxes show median and IQR, and whiskers represent minimum and maximum values.*

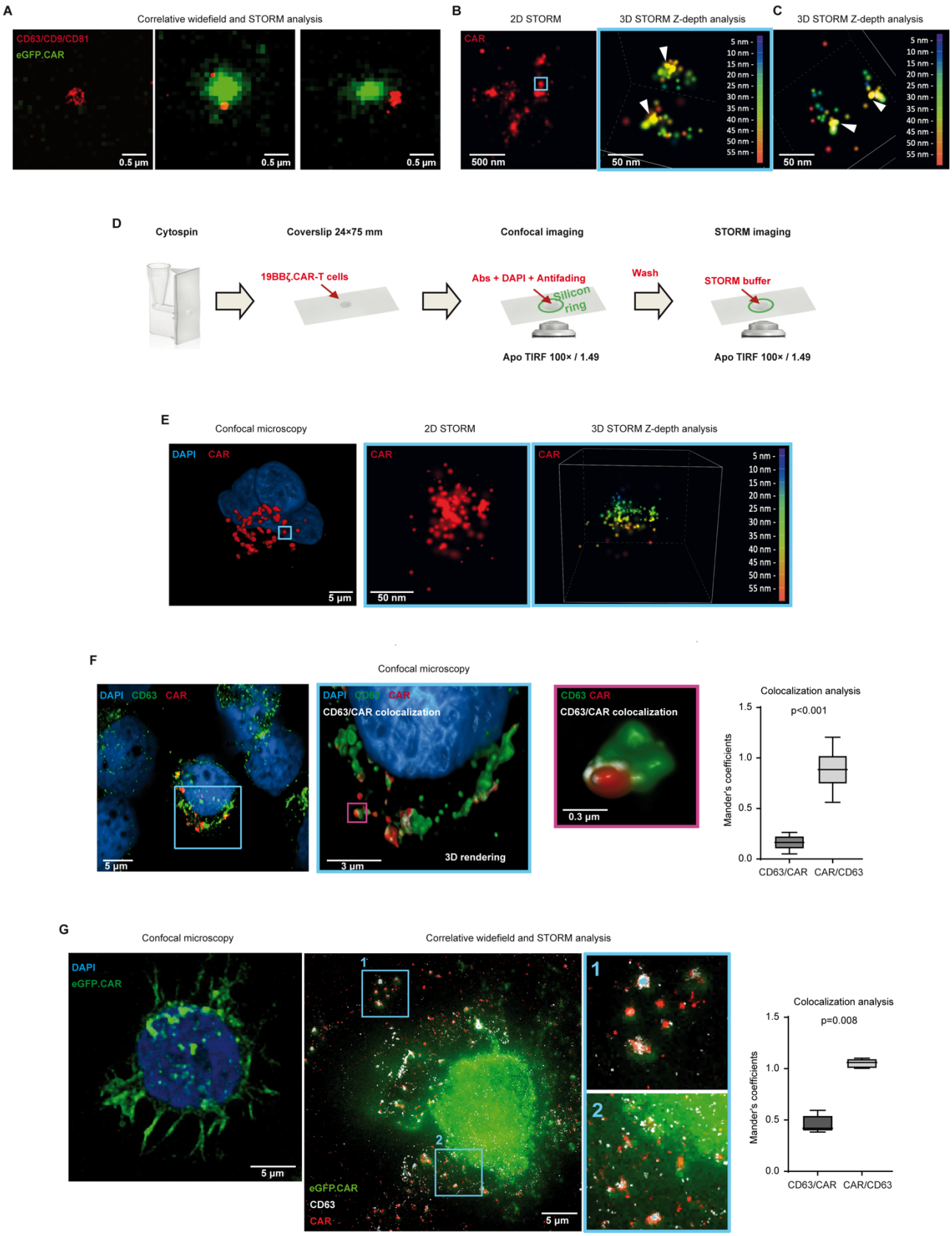

Figure 4. Combined confocal/STORM analysis of 19BBζ.CAR-T and 19BBζ.eGFP.CAR-T cells and CAR$^+$EVs. *(**A**) Analysis of 19BBζ.eGFP.CAR-T cell coculture supernatants (24 hours):*

*19BBζ.eGFP.CAR protein (eGFP.CAR; green, wide-field signal) and CD63/CD9/CD81 pool (red, STORM signal). Scale bars: 500 nm (n=6). (**B**) 19BBζ.CAR-T cell coculture supernatants (24 hours): 2D-STORM analysis of anti-CD19.CAR Ab-mediated pull-down CAR$^+$EVs (CAR; red; scale bar: 500 nm); 3D-STORM analysis of a single CAR$^+$EV (colors represent Z-depth; scale bar: 50 nm). White arrowheads highlight CD19.CAR antigen clusters on the EV (n=17). (**C**) 3D-STORM analysis (colors represent Z-depth; scale bar: 50 nm) of CAR-T cell supernatants purified by size-exclusion chromatography. White arrowheads highlight CD19.CAR antigen clusters on the EV (n=3). (**D**) Schematic representation of the combined confocal/STORM analysis workflow. (**E**) Combined confocal/STORM analysis with 3D rendering of a 19BBζ.CAR-T cell (CAR, red; DAPI, blue); detail of a CAR$^+$ intracellular vesicle observed in 2D- and 3D-STORM (blue box, magnification ×13) (n=3). Scale bars: 5 µm and 50 nm. (**F**) Confocal microscopy imaging of a 19BBζ.CAR-T cell (CAR, red; CD63, green; DAPI, blue). Colocalization details (blue box, ×3 magnification; purple box, ×22 magnification) measured by Manders' overlap coefficients (CD63 over CAR, and CAR over CD63, n=13, MW test) (n=7). Scale bars: 5 µm, 3 µm, and 0.3 µm. (**G**) Combined microscopy of 19BBζ.eGFP.CAR-T cells: confocal imaging of eGFP.CAR (green) and DAPI (blue), and correlative wide-field (eGFP.CAR, green)/STORM analysis (CD63, white, and CAR, red). Colocalization details (blue boxes, magnification ×2) measured by Manders' overlap coefficients (CD63 over CAR, and CAR over CD63, n=5, MW test) (n=2). Scale bars: 5 µm. Unless otherwise indicated, data are presented as boxes and whiskers; boxes show median and IQR, and whiskers represent minimum and maximum values.*

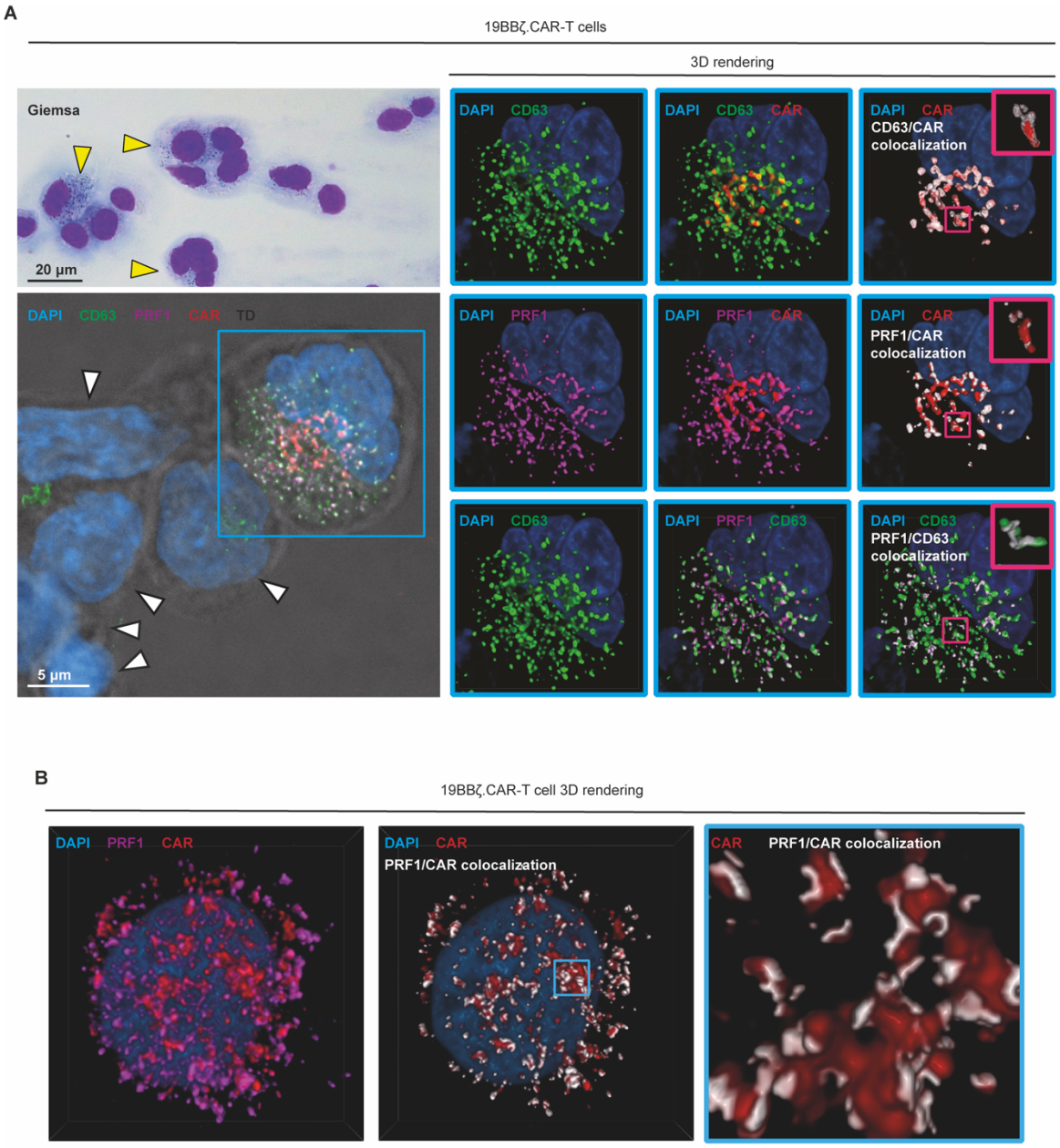

Figure 5. Confocal microscopy imaging of 19BBζ.CAR-T cell and colocalization details of CAR. *(**A**) Giemsa staining (yellow arrowheads mark T-cells with high content of cytotoxic granules, scale bar: 20 µm) and multicolor staining of 19BBζ.CAR-T cells: DAPI (blue), CD19.CAR (red), CD63 (green) and PRF1 (purple), TD (transmitted light differential interference contrast image, scale bar: 5 µm); white arrowheads mark CD19.CAR non-transduced cells; 3D rendering of 19BBζ.CAR-T cells and colocalization insets are shown, (n=3). (**B**) Confocal microscopy of DAPI (blue), CD19.CAR (red) and PRF1 (purple) staining of MFC-sorted 19BBζ.CAR-T cell (n=10).*

CAR$^+$EV detection in the plasma of patients after CD19.CAR-T cell infusion

Based on the in vitro findings, whether CAR$^+$EVs could be detected in the circulation of patients following CD19.CAR-T cell infusion, was next investigated. Plasma samples collected at day +1 from 14 patients were analyzed using the ExoView platform, which enables the immuno-capture and phenotyping of EVs immobilized onto CHIPs coated with antibodies targeting canonical exosomal tetraspanins (CD63, CD9, CD81; **Figure 6A**). CAR$^+$EVs were identified within all tetraspanin-defined subpopulations, representing 1.75% of CD63-captured EVs, 1.05% of CD9-captured EVs, and 0.26% of CD81-captured EVs (**Figure 6B**). Triple-positive CAR$^+$CD63$^+$CD9$^+$EVs accounted for 8.7%, 13.0%, and 30.7% of the CAR$^+$ fractions within the CD63-, CD9-, and CD81-captured EV subsets, respectively (**Figure 7A**). Differential ultracentrifugation confirmed the CAR$^+$EV exosome-like profile in both the large (20,000*g*) and small (100,000*g*) EV fractions (**Figures 6C-D**). Size-exclusion chromatography (SEC)-purified EVs retained identical phenotypic profiles when CAR$^+$EV fraction was identified using the recombinant CD19 protein as detection reagent (**Figure 7B**). Collectively, these results indicate that circulating CAR$^+$EVs predominantly express CD63 and CD9, similarly to CAR$^+$EVs derived from BL (**Figure 7C**). To further validate the exosomal nature of CAR$^+$EVs, they were purified through capture using anti-CD19.CAR-coated latex beads: this procedure resulted in substantial enrichment of CD63$^+$CAR$^+$EVs (27-fold), CD9$^+$CAR$^+$EVs (19.2-fold), and CD81$^+$CAR$^+$EVs (83-fold) (**Figure 6E**). In summary, plasma CAR$^+$EV pool consisted approximately of 50% CD63$^+$, 40% CD9$^+$, and <12% CD81$^+$ vesicles (**Figure 6F**). Moreover, MFC analyses yielded comparable results, revealing that most of both plasma-derived and BL-derived CAR$^+$EVs expressed the exosomal marker CD63 (**Figure 6G**). These findings were corroborated by STORM microscopy, which confirmed the presence of plasma CAR$^+$CD63$^+$EVs captured onto anti-tetraspanin antibody-coated slides (**Figure 6H**) and revealed intense clustering of CD19.CAR molecules on the vesicular surface (see **Figures 4A-B**). ExoView and MFC analyses further demonstrated that CAR$^+$EVs express PRF1, supporting their origin by cytotoxic cells (**Figures 7D-F**; Lettau et al., 2021). Conversely, these vesicles were largely devoid of the late endosomal marker CD107a/LAMP1 but displayed abundant WGA-binding surface glycoproteins, reminiscent of supra-molecular particles released by activated cytotoxic T-cells (**Figures 7G-H**; Bálint et al., 2020). In line

with previous reports (Bálint et al., 2020), the majority of CAR$^+$EVs lacked CD45 (**Figure 7I**). Nanoparticle tracking analysis of FACS-sorted and CD19.CAR-specific pull-down purified vesicles demonstrated that CAR$^+$EVs are mainly confined to the nano- (30-149 nm) and small (150-500 nm) EV size ranges (**Figures 8A-B**). A substantial subset of plasma CAR$^+$CD63$^+$EVs also carried the T-cell receptor (TCR)-associated kinase ZAP70 and the CD8β coreceptor (**Figure 8C**), while others were positive for FAS-ligand and the activation-induced tetraspanin CD151 (**Figures 9D-F**; Perez et al., 2020). In addition, MFC phenotyping of FACS-sorted CAR$^+$EVs revealed the presence of both CD4$^+$CAR$^+$EV and CD8$^+$CAR$^+$EV subsets, reflecting the CD4$^+$/CD8$^+$ composition of their parental CD19.CAR-T cell population (**Figures 9A-C**). Together, these results provide direct evidence that CAR$^+$EVs can be readily detected in the plasma of CD19.CAR-T cell-treated patients readily 1 day after infusion. Moreover, these vesicles display a composite exosomal and T-cell marker signature, harbor cytotoxic and TCR-signaling molecules, and thus likely mirror the activation state and effector polarization of their parental CD19.CAR-T cells.

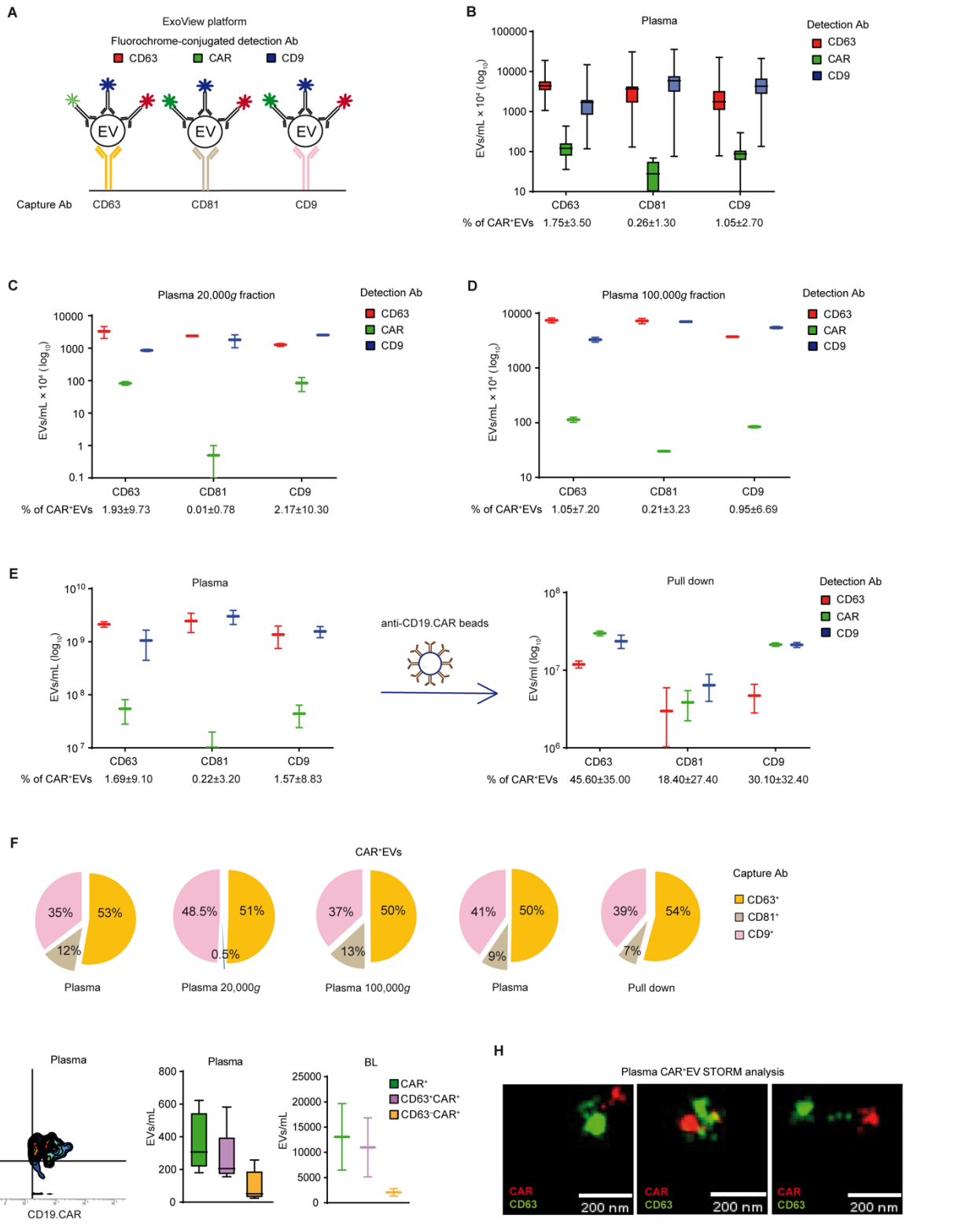

Figure 6. Plasma CAR⁺EV phenotype by ExoView, MFC, and STORM analysis. *(**A**) Schematic representation of ExoView platform analysis: CD63-, CD9-, or CD81-immunocaptured CAR⁺EVs are triple-stained by PE-anti-CD19.CAR, Alexa Fluor 647-anti-CD63, and Alexa Fluor 488-anti-CD9 Abs. (**B-D**) ExoView analysis of whole (n=14; **B**), 20,000g plasma fraction (n=2; **C**), and 100,000g plasma*

*fraction (n=2; **D**). (**E**) Anti-CD19.CAR Ab-mediated pull-down of plasma CAR$^+$EVs (n=2). (**F**) Pie charts represent the tetraspanin profile of CAR$^+$EVs analyzed in B-E, as ratio of CD63$^+$, CD81$^+$, or CD9$^+$ CAR$^+$EVs to total CAR$^+$EVs. (**G**) MFC analysis of plasma (n=5) and BL (n=2) CAR$^+$EVs. (**H**) Plasma CAR$^+$EV STORM analysis. Double-positive CAR$^+$CD63$^+$ EVs are shown (n=6). Scale bars: 200 nm. Unless otherwise indicated, data are presented as boxes and whiskers; boxes show median and IQR, and whiskers represent minimum and maximum values.*

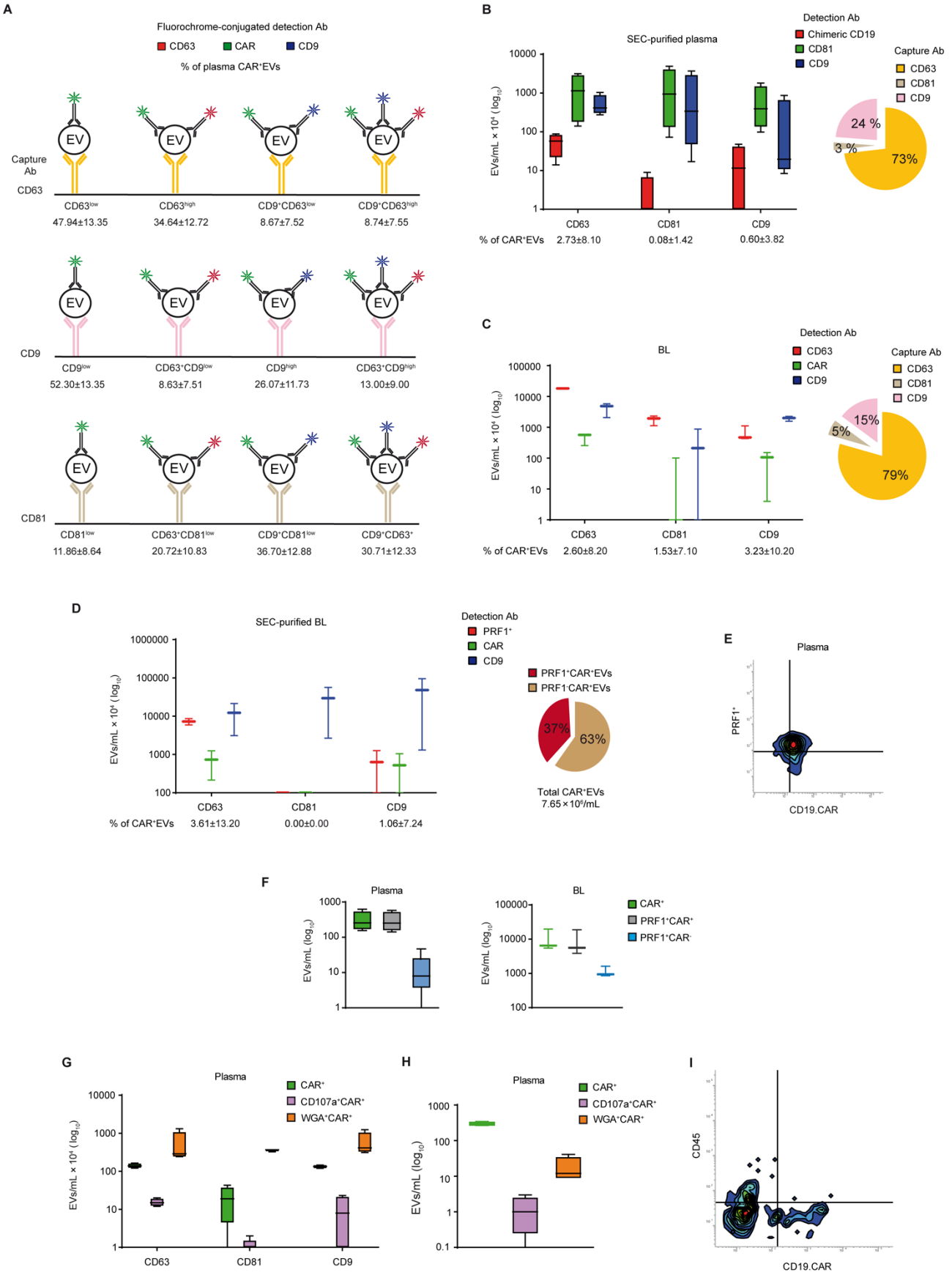

Figure 7. Plasma CAR⁺EV phenotype by ExoView and MFC. *(**A**) ExoView platform analysis of plasma CAR⁺EVs (n=14), showing CD63/CD9/CAR antigens colocalization on anti-CD9/CD63/CD81*

*Abs immuno-captured EVs (note that "low" refers to the detection of the antigen - e.g. CD63 - only by the immunocapture Ab, but not by the the fluorochrome-conjugated Ab specific for the same antigen; "high" refers to the detection of the antigen - e.g. CD63 - both by the immuno-capture Ab and by the fluorochrome-conjugated Ab specific for the same antigen. The phenomenon can be explained by the low amounts of a specific antigen (e.g. CD63) on the EVs surface, coupled with the clustering of the antigen on EVs that is likely to limit the antigen availability for immuno-detection. (**B**) ExoView platform analysis of size-exclusion chromatography (SEC)-purified EVs from CD19.CAR-T patient's plasma (n=4); pie chart represents the tetraspanin profile of CAR^+EVs. (**C**) ExoView platform analysis of EVs from BL (n=3), pie chart represents the tetraspanin profile of CAR^+EVs. (**D**) ExoView platform analysis of SEC-purified EVs from BL (n=2), pie-chart represents the % of $PRF1^+CAR^+$EVs over total CAR^+EVs. (**E**) Representative MFC analysis of $PRF1^+$ and CD19.CAR proteins in EVs from CD19.CAR-T patient's plasma. (**F**) MFC analysis of $PRF1^+CAR^+$EVs levels in CD19.CAR-T patients' plasma (n=6) and BL (n=3). (**G**) ExoView platform analysis of CD107a, WGA and CAR on plasma EVs (n=4). (**H**) MFC analysis of CD107a, WGA, CAR protein on plasma EVs (n=4); (**I**) representative MFC analysis of CD45 protein on plasma CAR^+EVs. Unless otherwise indicated, data are presented as boxes and whiskers; boxes show median and IQR, and whiskers represent minimum and maximum values.*

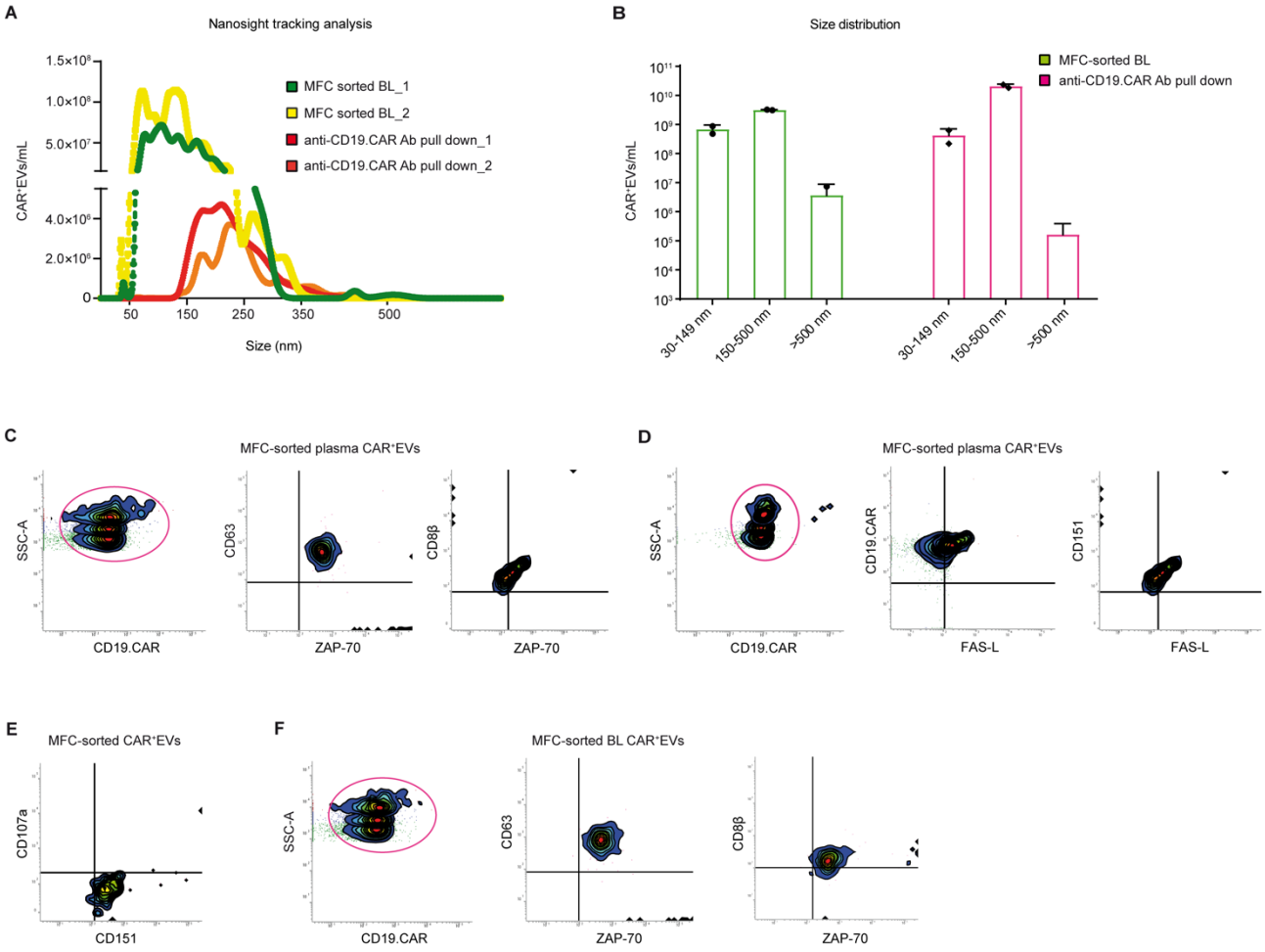

Figure 8. MFC-sorting of CAR$^+$EVs and Nanosight analysis. *(**A**) Nanosight tracking analysis (NTA) of MFC-sorted (n=2) and anti-CD19.CAR Ab pull down separated CAR$^+$EVs (n=2) from BL and plasma, respectively. (**B**) NTA assayed CAR$^+$EVs: size range classes distribution is shown. MFC analysis of MFC-sorted plasma CAR$^+$EVs for (**C**) ZAP70, CD63, CD8β proteins, (**D**) FAS-L and CD151 proteins, (**E**) CD107a and CD151 proteins. (**F**) MFC analysis of MFC-sorted CAR$^+$EVs from BL, assed for ZAP-70, CD63 and CD8β proteins.*

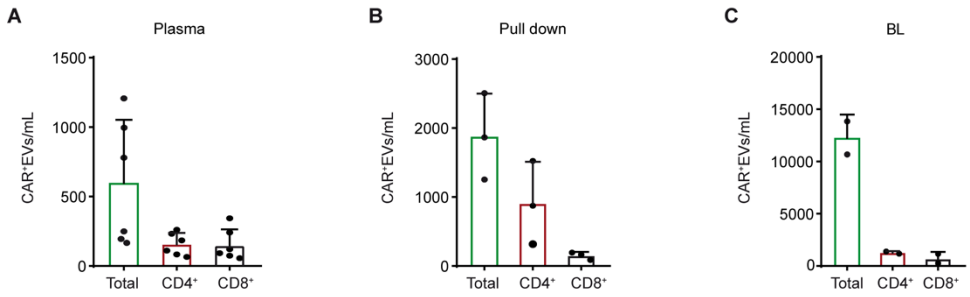

Figure 9. MFC analysis of CD4 and CD8 proteins on CAR$^+$EVs. *(**A**) Whole plasma (n=6), (**B**) anti-CD19.CAR Ab pull down (n=3) and (**C**) BLs (n=2). Data are shown as mean ± SD.*

CAR⁺EVs as early biomarkers of ICANS in patients infused with CD19.CAR-T cells

Given the identification of circulating CAR⁺EVs in patient's plasma and their strict correlation with CD19.CAR-T cell tissue or tumor trafficking, and activation upon target engagement, the next aim was to characterize their kinetics and to evaluate the potential associations with ICANS. Using ExoView analysis of day +1 plasma from 14 CD19.CAR-T cell-treated patients, a median CAR⁺EV concentration significantly higher in those who subsequently developed ICANS compared with those who did not (321 vs 207 CAR⁺EVs × 10^4/mL, **Figure 10A**) was observed. To further investigate this finding, CAR⁺EV kinetics were longitudinally assessed in an expanded cohort of 20 patients (8 with ICANS and 12 NO ICANS) by MFC (**Figure 10B**). Median $AUC_{0\text{-}21}$ values were markedly greater in ICANS patients (4,276 vs 1,672 CAR⁺EVs/μL×days, **Figure 10C**), whereas TTP values did not differ significantly (**Figure 10D**). The median peak concentration of plasma CAR⁺EVs was also significantly higher in ICANS patients (633 vs 175 CAR⁺EVs/μL, **Figure 10E**). Notably, the CAR⁺EVs peak preceded by approximately seven days the expansion peak of CD19.CAR-T cells as measured by both ddPCR and MFC (see **Figure 1**). The profiling of CAR⁺EV kinetics further revealed that differences between ICANS and NO ICANS patients were most pronounced at the earliest time points, namely at hour +1 and day +1 after infusion (see **Figure 10B**). Therefore, all available plasma samples (n=87) were analyzed at these time points by MFC. The results confirmed substantially higher median CAR⁺EV levels in ICANS patients at both hour +1 (439 vs 87 CAR⁺EVs/μL) and day +1 (1,123 vs 158 CAR⁺EVs/μL) after infusion (**Figure 10F**). Receiver Operating Characteristic (ROC) analysis demonstrated robust predictive performance, with values above 132.8 CAR⁺EVs/μL at hour +1 predicting ICANS onset with 89.3% sensitivity and 74.6% specificity, and values above 224.5 CAR⁺EVs/μL at day +1 yielding 96.6% sensitivity and 80.4% specificity (**Figure 10G**). To assess the independent predictive value of CAR⁺EV levels, multivariate logistic regression analyses were performed incorporating CAR⁺EVs (either hour +1 or day +1) alongside established clinical risk factors (see **Table 1**). Both early timepoints retained statistical significance as independent predictors of ICANS (hour +1: OR=1.02, 95% CI 1.01-1.03, p=0.00009; day +1: OR=1.01, 95% CI 1.00-1.01, p=0.00008). ECOG performance status ≥1 remained an additional independent variable (hour +1 model: OR=11.67, 95% CI 1.71-87.62, p=0.012; day +1 model: OR=11.36, 95% CI 1.70-

89.63, p=0.013). Conversely, disease type (PMBCL), progressive disease status at infusion, bridging therapy with immune checkpoint inhibitors, and G≥2 CRS lost statistical significance in multivariate models. Correlation analyses reinforced the strong association between CAR^+EV levels and neurotoxicity severity. Plasma CAR^+EV concentrations at both hour +1 ($r=0.669$, $p=1.47\times10^{-12}$) and day +1 ($r=0.725$, $p=4.46\times10^{-15}$) tightly correlated also with ICANS grade. Stratification by severity (G0-1 vs G≥2) confirmed that patients with G≥2 ICANS exhibited substantially higher median CAR^+EV levels (374 vs 97 $CAR^+EVs/\mu L$ at hour +1; 840 vs 167 $CAR^+EVs/\mu L$ at day +1; **Figure 10H)**. ROC curve analysis established cutoffs predictive of G≥2 ICANS: >181.5 $CAR^+EVs/\mu L$ at hour +1 (75.0% sensitivity, 82.1% specificity) and >372.3 $CAR^+EVs/\mu L$ at day +1 (85.0% sensitivity, 81.5% specificity) after infusion (**Figure 10I**). Early CAR^+EV levels correlated positively with CAR^+T cells and CAR-DNA as measured at day +7 after infusion, and also with the expansion peaks of $CD8^+CAR^+$ effector memory T-cells ($CD8^+CAR\text{-}T_{EM}$), supporting their origin from activated cytotoxic subsets (hour +1: $r=0.580$, $p=0.002$; day +1: $r=0.463$, $p=0.017$; **Figures 11A-B**). Importantly, total plasma EV concentrations did not differ between ICANS and NO ICANS patients at either timepoint (**Figures 11C-D**), indicating that the observed phenomenon was specific to the CAR^+EV compartment. Collectively, these data establish plasma CAR^+EVs as robust and early biomarkers of ICANS onset and severity, preceding both CAR-T cell expansion and clinical manifestation.

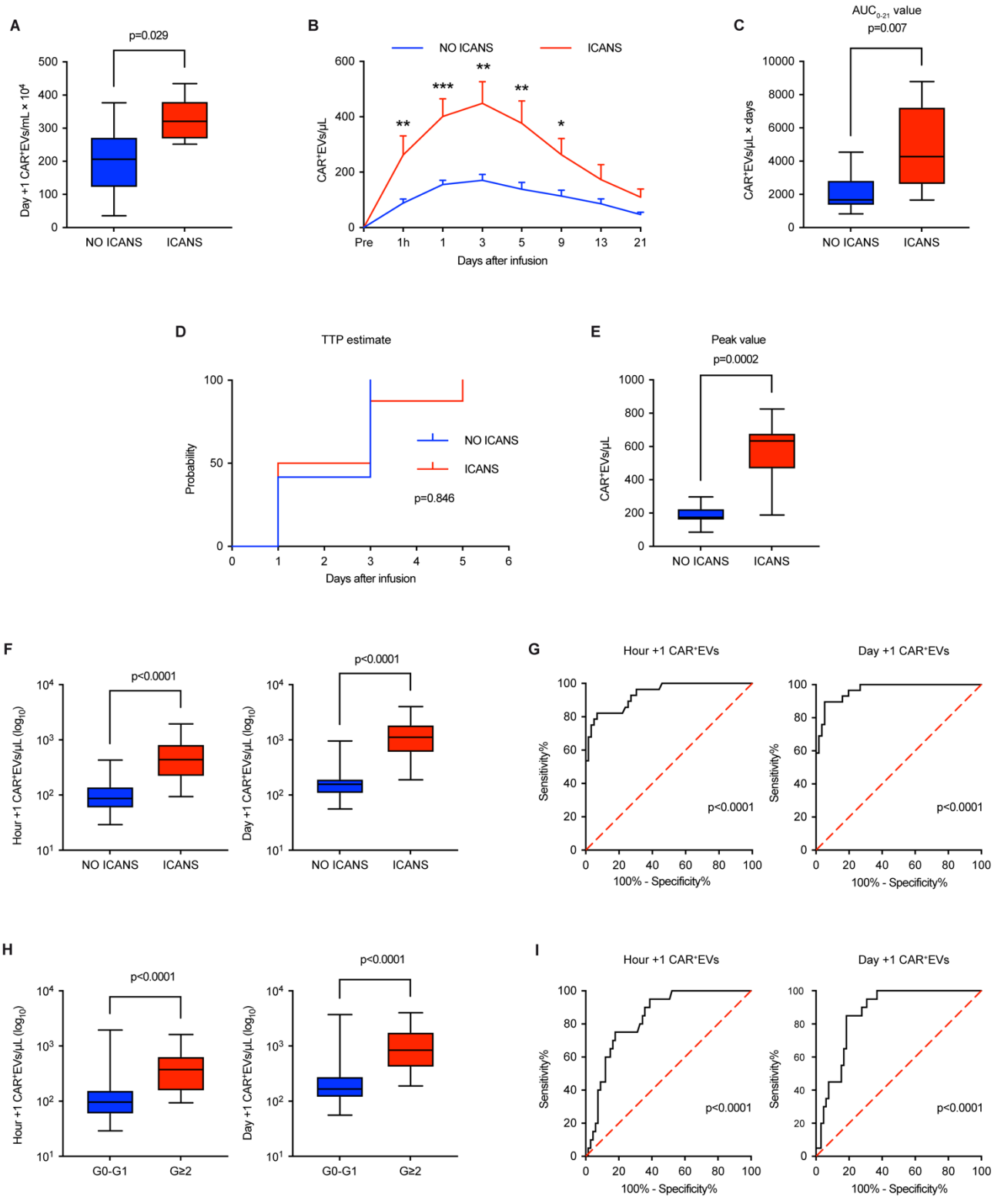

Figure 10. Plasma CAR⁺EVs: early markers of ICANS. *(**A**) Day +1 plasma CAR⁺EVs measured by ExoView in NO ICANS (n=8) versus ICANS (n=6); MW test. (**B-E**) Plasma CAR⁺EVs assessed by MFC in NO ICANS (n=12) versus ICANS (n= 8): (**B**) twenty-one-day kinetics (mean ± SEM; *p< 0.05, **p<0.01, ***p<0.001, multiple MW test); (**C**) $AUC_{0\text{-}21}$ estimate value, MW test. (**D**) KM estimate of TTP; log-rank test. (**E**) Peak value; MW test. (**F** and **G**) MFC analysis of hour +1 plasma CAR⁺EVs in NO ICANS (n=59) versus ICANS (n=28) and day +1 plasma CAR⁺EVs in NO ICANS (n=56) versus*

*ICANS (n=29), MW test (**F**), and respective ROC curve analysis (**G**). (**H** and **I**) MFC analysis of hour +1 plasma CAR$^+$EVs in grade 0 (G0) to G1 ICANS (n=67) versus G≥2 ICANS (n=20) and day +1 plasma CAR$^+$EVs in G0-G1 ICANS (n=65) versus G≥2 ICANS (n=20), MW test (**H**), and respective ROC curve analysis (**I**). Unless otherwise indicated, data are presented as boxes and whiskers; boxes show median and IQR, and whiskers represent minimum and maximum values.*

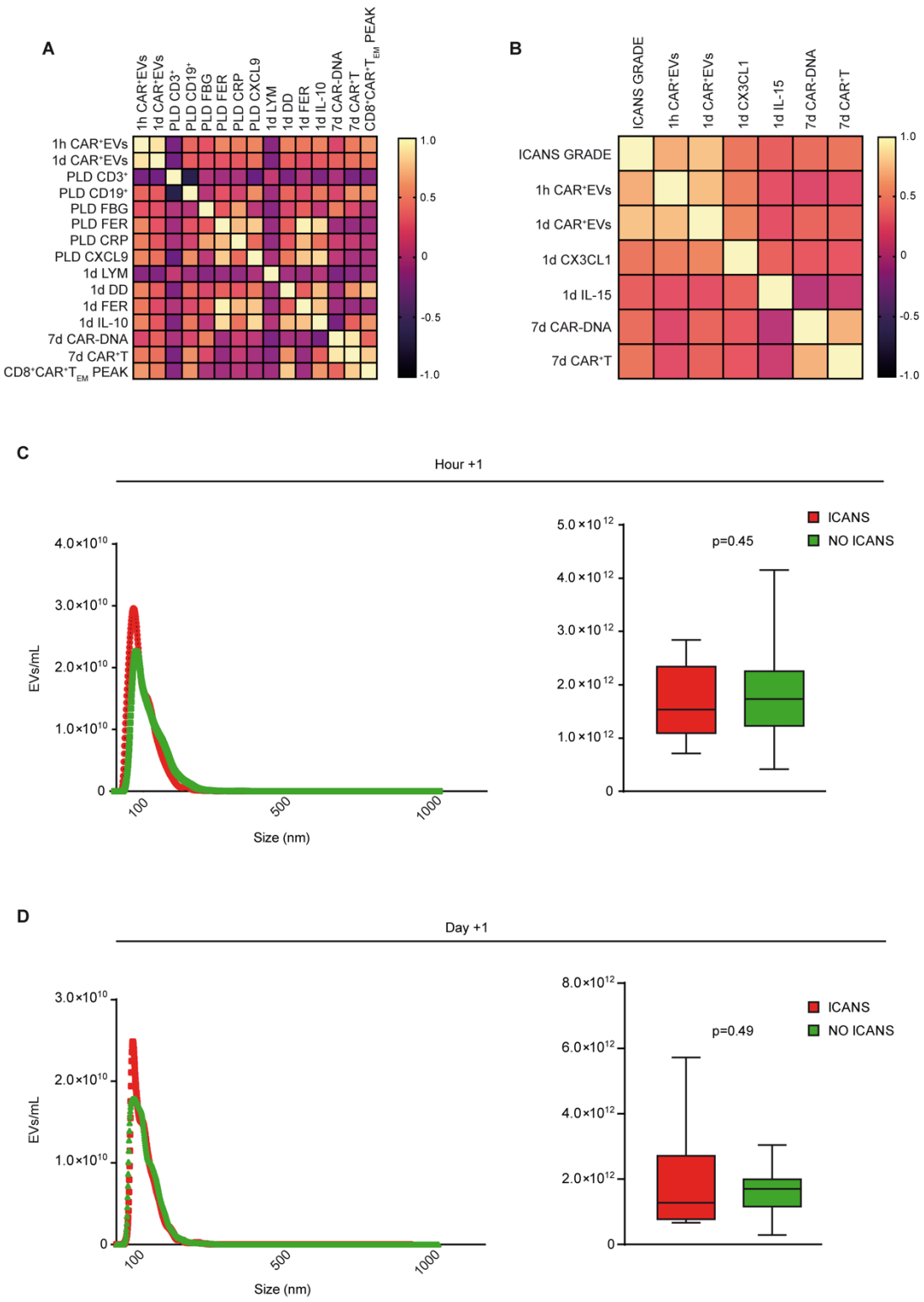

Figure 11. ***CAR⁺EV correlation and total EVs.*** *(**A**) Heatmap of Pearson's correlation coefficients for hour +1 (1h) and day +1 (1d) CAR⁺EVs with pre-lymphodepletion (PLD) and 1d biochemical parameters, day +7 (7d) CAR-DNA copies and CAR⁺T cells, and peak levels of CAR⁺CD8⁺T_{EM} cells. (**B**) Heatmap of Spearman's correlation coefficients of ICANS grade with 1h and 1d CAR⁺EVs, 1d biochemical parameters, 7d CAR⁺T cells and 7d CAR-DNA copies. NTA of 1h (**C**) and 1d (**D**) plasma total EVs in NO ICANS (n=26) vs ICANS (n=14) patients; MW test. Unless otherwise indicated, data*

are presented as boxes and whiskers; boxes show median and IQR, and whiskers represent minimum and maximum values.

Neuron-specific ENO2^{+} nanoparticles as markers of CAR^{+}EV-induced neural stress

Owing to the association of CAR^{+}EVs with ICANS, the hypothesis that CAR^{+}EVs may mediate toxic effects on neural cells was tested. To this aim, an in vitro model of human iPSC-derived neural progenitors and mature neurons was exploited (**Figure 12**). CAR^{+}EVs purified from 19BBζ.CAR-T cells and two CD19.CAR-T BLs exerted negligible effects on iPSC-derived neuron viability and/or metabolic activity (**Figure 12B**). As extracellular neuron-specific Enolase (ENO2) has been reported to be a marker of neural stress (Mustapic et al., 2017; Agliardi et al., 2020) and to be part of subcellular structures, called supermeres, characterized as extracellular nanoparticles (NPs; Zhang et al., 2021), ENO2^{+}NP release in the supernatant of iPSC-derived neurons exposed to CAR^{+}EVs was investigated. Upon 24-hour exposure to CAR^{+}EVs, measurable amounts of ENO2^{+}NPs in the iPSC supernatants, but not in the ones with untreated cultures were found (**Figure 12C**). To confirm the role of ENO2^{+}NPs as markers of ongoing CAR-T related neurotoxicity, the plasma of 8 ICANS and 12 NO ICANS patients at day +5, which represents the median day of ICANS onset, was assessed. Higher plasma levels of ENO2^{+}NPs in patients with ICANS compared with NO ICANS ones (**Figure 12C**) were found. Notably, Zhang et al. also reported that ENO2^{+}NPs carry abundant amounts of miR-1246 (Zhang et al., 2021). Indeed, higher median plasma levels of miR-1246 in ICANS than in NO ICANS patients (1,797 vs. 240.4; **Figure 12E**) were demonstrated, and a positive correlation between ENO2^{+}NPs and miR-1246 plasma levels ($r=0.521$, $p=0.018$) was found, suggesting that ENO2^{+}NPs and miR-1246 could be markers of neural stress in CD19.CAR-T cell-infused patients developing ICANS.

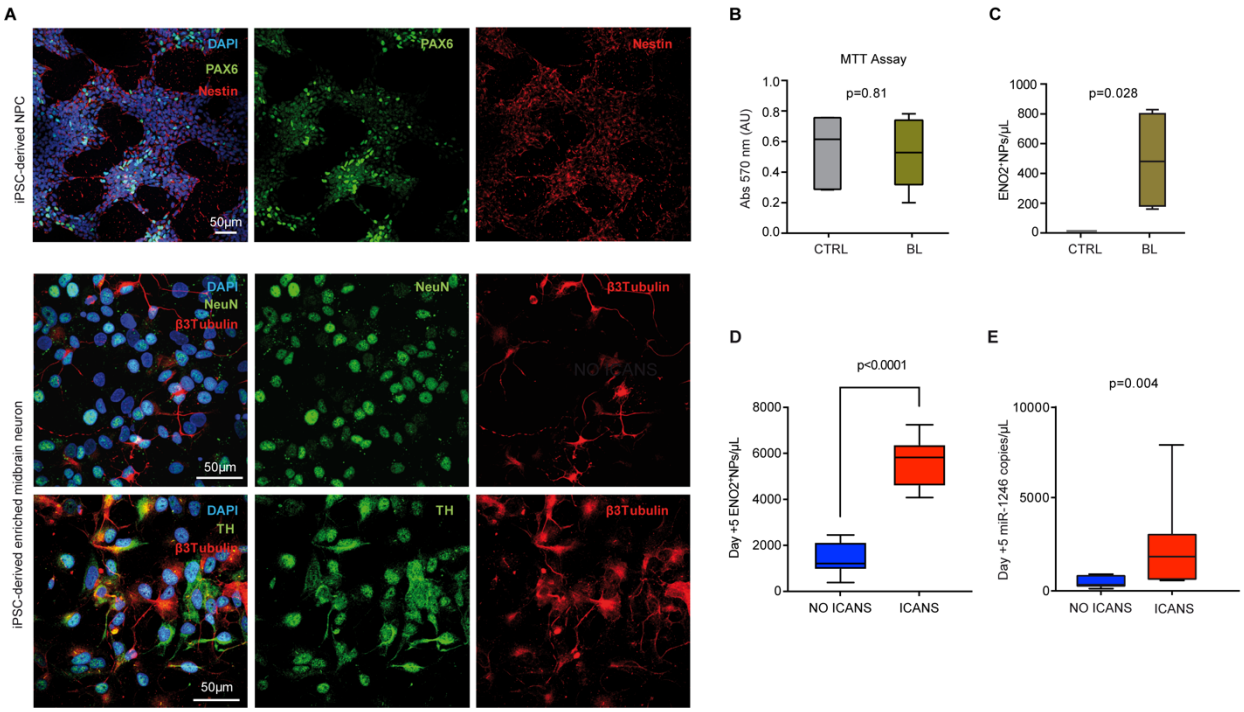

Figure 12. Neuron-specific Enolase 2-positive NPs (ENO2$^+$NPs): markers of neural damage. *(**A**) Representative pictures of healthy donor iPSC-derived neural cells: neural precursor cells (NPCs) stained with Abs against Pax6 (green) and nestin (red), and enriched midbrain neurons stained with Abs against β3-tubulin (red) and NeuN (green) or Abs against tyrosine hydroxylase (TH; green) and β3-tubulin (red). Nuclei were counterstained with DAPI (blue) (n=3). Scale bars: 50 µm. (**B**) MTT assay of iPSC-derived neural cells exposed to EVs from CD19$^+$ cell supernatants (CTRL, n=6) versus BL (n=14). (**C**) MFC analysis of Enolase 2-positive (ENO2$^+$) NP release by iPSC-derived neural cells exposed to EVs from CD19$^+$ cell supernatants (CTRL, n=4) versus BL (n=4); MW test. (**D** and **E**) Day +5 analysis of plasma ENO2$^+$NPs assessed by MFC (D) and miR-1246 assessed by ddPCR (**E**) in ICANS (n=8) versus NO ICANS (n=12); MW test. Unless otherwise indicated, data are presented as boxes and whiskers; boxes show median and IQR, and whiskers represent minimum and maximum values.*

CAR⁺EVs and CRS in patients infused with CD19.CAR-T cells

Finally, CAR⁺EV levels were also explored with regard their potential association with CRS. While no difference was observed at hour +1 between CRS and NO CRS patients (113 vs 125 CAR⁺EVs/μL), day +1 levels were significantly higher in patients who developed CRS (223 vs 151 CAR⁺EVs/μL) after infusion (**Figures 13A-B**). However, logistic regression analysis failed to confirm CAR⁺EVs as independent CRS predictors (hour +1: OR=1.004, 95% CI 0.99-1.01, p=0.26; day +1: OR=1.01, 95% CI 1.00-1.02, p=0.17). Still, in patients with G≥2 CRS, plasma CAR⁺EV levels were significantly higher compared to those with G0-G1 CRS, both at hour +1 (271.5 vs 108 CAR⁺EVs/μL) and day +1 (682 vs 177.5 CAR⁺EVs/μL) after infusion (**Figures 13C-D**). Hence, considering that the median onset of CRS occurred 1 day after infusion, these findings - unlike those observed for ICANS - suggest a marginal contribution of CAR⁺EVs as predictors of CRS onset, supporting instead their role as biomarkers of systemic inflammatory activation rather than as direct causal mediators.

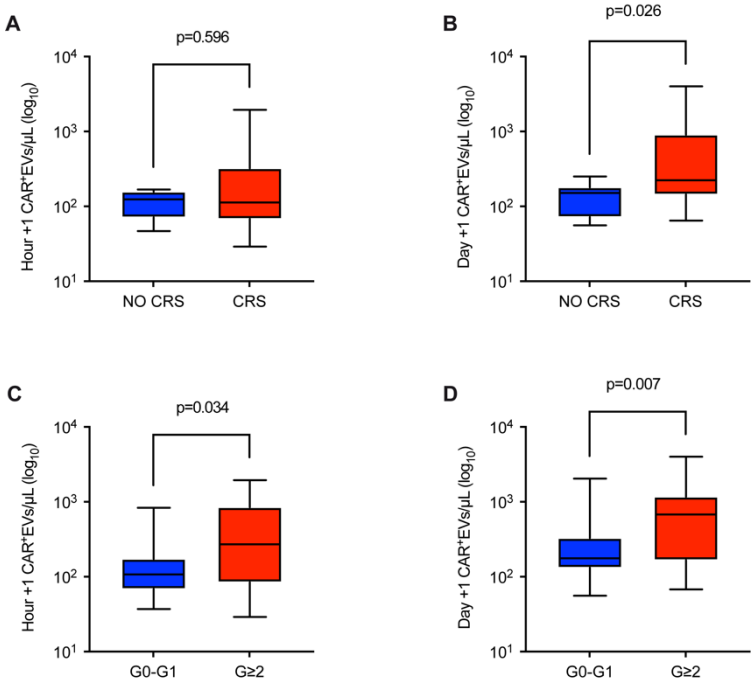

Figure 13. Plasma CAR⁺EVs and CRS. *(**A**) MFC analysis of: hour +1 plasma CAR⁺EVs in NO CRS (n=8) vs CRS (n=79); (**B**) day +1 plasma CAR⁺EVs in NO CRS (n=8) vs CRS (n=77); (**C**) hour +1 plasma CAR⁺EVs in G0-G1 CRS (n=61) vs G≥2 CRS (n=26); (**D**) day +1 plasma CAR⁺EVs in G0-*

G1 CRS (n=58) vs G≥2 CRS (n=27); MW test. Data are presented as boxes and whiskers; boxes show median and IQR, whiskers represent minimum and maximum values.

DISCUSSION

This study was driven by the compelling need to identify early biomarkers of CAR-T cell therapy-associated neurotoxicity, which might also yield novel insights into ICANS pathogenesis. The central finding of this work is the identification of CAR$^+$ extracellular vesicles (CAR$^+$EVs), released as an immediate and quantifiable hallmark of CD19.CAR-T cell activation upon target engagement. A crucial observation is that in vitro experiments demonstrated that CAR$^+$EV release occurs predominantly within the first hours following the establishment of coculture, thus representing an early event after cognate antigen recognition. Notably, CAR$^+$EVs were also detectable in the plasma of treated patients as early as one hour after infusion. Taken together, these findings indicate that target engagement is a very early in vivo event, appreciable within the first hours after infusion, thereby providing direct evidence of the precocious tissue trafficking and functional activity of CD19.CAR-T cells. These findings are consistent with previous evidences demonstrating, histologically, the early and transient tissue trafficking of CAR-T cells following their infusion (Chen et al., 2020). Such rapid redistribution has also been indirectly inferred from the prompt decline in circulating CAR-T cells (as measured by ddPCR) readily after infusion (Mueller et al., 2017). Similarly, in this study, the early rise in plasma CAR$^+$EV levels paralleled a transient reduction in circulating CD19.CAR-T cells, as evidenced by the decrease in CAR-DNA copy numbers within the first 24 hours post-infusion. The vesicular nature of CAR$^+$EVs was confirmed through a combination of complementary analytical approaches - including ExoView, MFC, confocal microscopy, and STORM imaging - which collectively confirmed both their phenotype and structural features. CAR$^+$EVs consistently express canonical exosomal markers, with CD63 emerging as the most prominent tetraspanin component (Möller et al., 2020). Confocal and STORM analyses further demonstrated that CD19.CAR-T cells harbor preassembled, CD63-rich vesicular granules within their cytoplasm, which are rapidly mobilized and secreted upon cognate antigen engagement (Lettau et al., 2021). In line with an endosomal origin, MFC analyses showed that CAR$^+$EVs lack CD45 but are enriched in T-cell receptor-associated molecules such as CD4, CD8, and the CD3ζ-associated kinase ZAP70 (Li et al., 2020). These features mirror a vesicular population derived from the

immunological synapse, closely resembling the nanoparticle released during T-cell activation (Lettau et al., 2020; Céspedes et al., 2022). Moreover, CAR^+EV levels can anticipate the in vivo CAR-T cell kinetics and phenotype: plasma CAR^+EV concentrations measured at day +1 after infusion correlated with both day +7 circulating CD19.CAR-T cell count and the expansion peaks of $CD8^+CAR^+T_{EM}$. The rapid trafficking and activation upon target engagement patterns are particularly evident in patients who subsequently develop ICANS. Interestingly, these ones also exhibit high plasma levels of IL-15 - a potent driver of CAR-T cell activation (Xu et al., 2014; Zhou et al., 2019; Alizadeh et al., 2019) - and the chemokine CX3CL1 (fractalkine), a key mediator of $CX3CR1^+$T-cell peripheral tissue and tumor homing (Imai et al., 1997). Both cytokines positively correlate with biomarkers of systemic inflammation and tumor burden, including fibrinogen, LDH, CRP, cfDNA, and CXCL9, measured prior to lymphodepletion and already reported to be linked to heightened risk of neurotoxicity (Strati et al., 2020; Locke et al., 2020). Of note, higher IL-15 and CX3CL1 levels were observed in patients who received chemotherapy-based bridging regimens, suggesting that prior cytotoxic exposure may impact subsequent CAR-T cell dynamics and toxicities. Remarkably, CAR^+EV elevation was detectable up to four days before the median onset of neurotoxicity (day +5), thereby representing a far more useful biomarker than traditional indicators such as the CAR-T cell expansion peak, which typically occurs too late to serve predictive purposes. By contrast, although higher day +1 CAR^+EV levels were observed in patients who developed CRS, their predictive value was limited due to the typically early (day +1) onset of this toxicity. Interestingly, in the subset of 20 patients with longitudinal CAR^+EV assessment up to day +21, we were unable to clearly delineate the impact of CRS- or ICANS-directed therapies on vesicle kinetics. Moreover, consistent with prior reports describing the ability of CAR-T cells to kill cells expressing their target antigen (Fu et al., 2019; Aharon et al., 2021), CAR^+EVs were found to carry substantial amounts of perforin, suggesting their potential neurotoxic activity within the CNS (Matsui et al., 2020). Notably, the absence of the endosomal marker CD107a and the presence of wheat germ agglutinin-detectable glycoproteins resemble supramolecular complexes containing perforin, which are presumed to possess autonomous extracellular cytolytic activity (Bálint et al., 2020). Consistent with the clinical observation that most ICANS cases resolve completely without persistent neurological sequelae,

CAR$^+$EVs exert negligible cytotoxic effects on iPSC-derived neural cells but induce the release of neuron-specific Enolase (ENO2), a well-established marker of neural stress (Mustapic et al., 2017; Agliardi et al., 2020). This marker was detectable by flow cytometry as nanoparticles (NPs) with EV-like morphology. These NPs were enriched in miR-1246, detectable in plasma, and potentially capable of crossing the blood-brain barrier (Zhang et al., 2021). Strikingly, elevated plasma levels of ENO2$^+$NPs and miR-1246 were observed in patients experiencing ICANS, suggesting their potential role as biomarkers of neural cell stress during ICANS. Together, these findings support a model in which ICANS arises in the context of excessive early tissue/tumor trafficking and activation of CD19.CAR-T cells, potentially driven by IL-15 and CX3CL1 axes. Although the current number of patients with available CX3CL1 and IL-15 assessments remains limited, the expansion of the cohort and the integration of CX3CL1 and IL-15 measurements into a predictive model with CAR$^+$EVs may provide a more comprehensive framework to capture both immune activation and trafficking dynamics following CAR-T cell infusion. In this study, plasma CAR$^+$EVs emerge as sensitive and minimally invasive biomarkers of CD19.CAR-T cell activation subsequently to antigen engagement and early predictors of ICANS occurrence. Experimental confirmation through animal models and ex vivo CNS systems will be required to elucidate causality and molecular mechanisms. Moreover, future investigations should explore the role of CAR$^+$EVs in the early CD19.CAR-T cell efficacy assessment. In conclusion, the identification of CAR$^+$EVs as early predictors and specific biomarker of ICANS represents a major step forward in the understanding of CAR-T related neurotoxicity. These findings reveal a new dimension of CAR-T biology linking activation kinetics, vesicular crosstalk, and neural stress, and hold the potential to reshape both monitoring strategies and “pre-emptive” therapy for ICANS, to enhance the safety of next-generation cellular immunotherapies.

REFERENCES

- Abramson JS, Palomba ML, Gordon LI, et al. Lisocabtagene maraleucel for patients with relapsed or refractory large B-cell lymphomas (TRANSCEND NHL 001): a multicentre seamless design study. Lancet. 2020;396(10254):839-852.
- Abramson JS, Palomba ML, Gordon LI, et al. Two-year follow-up of lisocabtagene maraleucel in relapsed or refractory large B-cell lymphoma in TRANSCEND NHL 001. Blood. 2024;143(5):404-416.
- Agliardi C, Meloni M, Guerini FR, et al. Oligomeric α-Syn and SNARE complex proteins in peripheral extracellular vesicles of neural origin are biomarkers for Parkinson's disease. Neurobiol Dis. 2021;148:105185.
- Aharon A, Horn G, Bar-Lev TH, et al. Extracellular Vesicles Derived from Chimeric Antigen Receptor-T Cells: A Potential Therapy for Cancer. Hum Gene Ther. 2021;32(19-20):1224-1241.
- Alizadeh D, Wong RA, Yang X, et al. IL15 Enhances CAR-T Cell Antitumor Activity by Reducing mTORC1 Activity and Preserving Their Stem Cell Memory Phenotype. Cancer Immunol Res. 2019;7(5):759-772.
- Bertuccio SN, Boudia F, Cambot M, et al. The Pediatric Acute Leukemia Fusion Oncogene ETO2-GLIS2 Increases Self-Renewal and Alters Differentiation in a Human Induced Pluripotent Stem Cells-Derived Model. Hemasphere. 2020;4(1):e319.
- Bishop MR, Dickinson M, Purtill D, et al. Second-Line Tisagenlecleucel or Standard Care in Aggressive B-Cell Lymphoma. N Engl J Med. 2022;386(7):629-639.

- Bjorkman PJ, Saper MA, Samraoui B, Bennett WS, Strominger JL, Wiley DC. The foreign antigen binding site and T cell recognition regions of class I histocompatibility antigens. Nature. 1987;329(6139):512-518.
- Buzas EI. The roles of extracellular vesicles in the immune system. Nat Rev Immunol. 2023;23(4):236-250.
- Bálint Š, Müller S, Fischer R, et al. Supramolecular attack particles are autonomous killing entities released from cytotoxic T cells. Science. 2020;368(6493):897-901.
- Chen PH, Lipschitz M, Weirather JL, et al. Activation of CAR and non-CAR T cells within the tumor microenvironment following CAR T cell therapy. JCI Insight. 2020;5(12):e134612.
- Cointe S, Judicone C, Robert S, et al. Standardization of microparticle enumeration across different flow cytometry platforms: results of a multicenter collaborative workshop. J Thromb Haemost. 2017;15(1):187-193.
- Cooper ML, Choi J, Staser K, et al. An "off-the-shelf" fratricide-resistant CAR-T for the treatment of T cell hematologic malignancies. Leukemia. 2018;32(9):1970-1983.
- Cordas Dos Santos DM, Tix T, Shouval R, et al. A systematic review and meta-analysis of nonrelapse mortality after CAR T cell therapy. Nat Med. 2024;30(9):2667-2678.
- Céspedes PF, Jainarayanan A, Fernández-Messina L, et al. T-cell trans-synaptic vesicles are distinct and carry greater effector content than constitutive extracellular vesicles. Nat Commun. 2022;13(1):3460.

- Del Bufalo F, Becilli M, Rosignoli C, et al. Allogeneic, donor-derived, second-generation, CD19-directed CAR-T cells for the treatment of pediatric relapsed/refractory BCP-ALL. Blood. 2023;142(2):146-157.
- Dias J, Garcia J, Agliardi G, Roddie C. CAR-T cell manufacturing landscape-Lessons from the past decade and considerations for early clinical development. Mol Ther Methods Clin Dev. 2024;32(2):101250.
- Dreyling M, Fowler NH, Dickinson M, et al. Durable response after tisagenlecleucel in adults with relapsed/refractory follicular lymphoma: ELARA trial update. Blood. 2024;143(17):1713-1725.
- Du B, Qin J, Lin B, Zhang J, Li D, Liu M. CAR-T therapy in solid tumors. Cancer Cell. 2025;43(4):665-679.
- Ferreri CJ, Bhutani M. Mechanisms and management of CAR T toxicity. Front Oncol. 2024;14:1396490.
- Fu W, Lei C, Liu S, et al. CAR exosomes derived from effector CAR-T cells have potent antitumour effects and low toxicity. Nat Commun. 2019;10(1):4355.
- Garcia KC, Degano M, Stanfield RL, et al. An alphabeta T cell receptor structure at 2.5 A and its orientation in the TCR-MHC complex. Science. 1996;274(5285):209-219.
- Gardner RA, Ceppi F, Rivers J, et al. Preemptive mitigation of CD19 CAR T-cell cytokine release syndrome without attenuation of antileukemic efficacy. Blood. 2019;134(24):2149-2158.
- Gazeau N, Liang EC, Wu QV, et al. Anakinra for Refractory Cytokine Release Syndrome or Immune Effector Cell-Associated Neurotoxicity Syndrome after Chimeric Antigen Receptor T Cell Therapy. Transplant Cell Ther. 2023;29(7):430-437.

- Gill S, Tasian SK, Ruella M, et al. Preclinical targeting of human acute myeloid leukemia and myeloablation using chimeric antigen receptor-modified T cells. Blood. 2014;123(15):2343-2354.
- Graham CE, Velasco R, Alarcon Tomas A, et al. Non-ICANS neurological complications after CAR T-cell therapies: recommendations from the EBMT Practice Harmonisation and Guidelines Committee. Lancet Oncol. 2025;26(4):e203-e213.
- Greenbaum U, Strati P, Saliba RM, et al. CRP and ferritin in addition to the EASIX score predict CAR-T-related toxicity. Blood Adv. 2021;5(14):2799-2806.
- Gust J, Hay KA, Hanafi LA, et al. Endothelial Activation and Blood-Brain Barrier Disruption in Neurotoxicity after Adoptive Immunotherapy with CD19 CAR-T Cells. Cancer Discov. 2017;7(12):1404-1419.
- Gust J, Ponce R, Liles WC, Garden GA, Turtle CJ. Cytokines in CAR T Cell-Associated Neurotoxicity. Front Immunol. 2020;11:577027.
- Haubner S, Subklewe M, Sadelain M. Honing CAR T cells to tackle acute myeloid leukemia. Blood. 2025;145(11):1113-1125.
- Hayden PJ, Roddie C, Bader P, et al. Management of adults and children receiving CAR T-cell therapy: 2021 best practice recommendations of the European Society for Blood and Marrow Transplantation (EBMT) and the Joint Accreditation Committee of ISCT and EBMT (JACIE) and the European Haematology Association (EHA). Ann Oncol. 2022;33(3):259-275.
- Hines MR, Knight TE, McNerney KO, et al. Immune Effector Cell-Associated Hemophagocytic Lymphohistiocytosis-Like Syndrome. Transplant Cell Ther. 2023;29(7):438.e1-438.e16.

- Hirayama AV, Gauthier J, Hay KA, et al. The response to lymphodepletion impacts PFS in patients with aggressive non-Hodgkin lymphoma treated with CD19 CAR T cells. Blood. 2019;133(17):1876-1887.
- Imai T, Hieshima K, Haskell C, et al. Identification and molecular characterization of fractalkine receptor CX3CR1, which mediates both leukocyte migration and adhesion. Cell. 1997;91(4):521-530.
- Innamarato P, Kodumudi K, Asby S, et al. Reactive Myelopoiesis Triggered by Lymphodepleting Chemotherapy Limits the Efficacy of Adoptive T Cell Therapy. Mol Ther. 2020;28(10):2252-2270.
- June, C. H. & Sadelain, M. Chimeric Antigen Receptor Therapy. New England Journal of Medicine 379, 64-73 (2018).
- Kadauke S, Myers RM, Li Y, et al. Risk-Adapted Preemptive Tocilizumab to Prevent Severe Cytokine Release Syndrome After CTL019 for Pediatric B-Cell Acute Lymphoblastic Leukemia: A Prospective Clinical Trial. J Clin Oncol. 2021;39(8):920-930.
- Kamdar M, Solomon SR, Arnason J, et al. Lisocabtagene Maraleucel Versus Standard of Care for Second-Line Relapsed/Refractory Large B-Cell Lymphoma: 3-Year Follow-Up From the Randomized, Phase III TRANSFORM Study. J Clin Oncol. 2025;43(24):2671-2678.
- Karschnia P, Jordan JT, Forst DA, et al. Clinical presentation, management, and biomarkers of neurotoxicity after adoptive immunotherapy with CAR T cells. Blood. 2019;133(20):2212-2221.
- Lee DW, Santomasso BD, Locke FL, et al. ASTCT Consensus Grading for Cytokine Release Syndrome and Neurologic Toxicity Associated with Immune Effector Cells. Biol Blood Marrow Transplant. 2019;25(4):625-638.

- Lee M, Lee Y, Song J, Lee J, Chang SY. Tissue-specific Role of CX3CR1 Expressing Immune Cells and Their Relationships with Human Disease. Immune Netw. 2018;18(1):e5.
- Lettau M, Janssen O. Intra- and Extracellular Effector Vesicles From Human T And NK Cells: Same-Same, but Different?. Front Immunol. 2021;12:804895.
- Li R, Ma C, Cai H, Chen W. The CAR T-Cell Mechanoimmunology at a Glance. Adv Sci (Weinh). 2020;7(24):2002628.
- Limatola C, Ransohoff RM. Modulating neurotoxicity through CX3CL1/CX3CR1 signaling. Front Cell Neurosci. 2014;8:229.
- Liévin R, Di Blasi R, Morin F, et al. Effect of early granulocyte-colony-stimulating factor administration in the prevention of febrile neutropenia and impact on toxicity and efficacy of anti-CD19 CAR-T in patients with relapsed/refractory B-cell lymphoma. Bone Marrow Transplant. 2022;57(3):431-439.
- Locke FL, Rossi JM, Neelapu SS, et al. Tumor burden, inflammation, and product attributes determine outcomes of axicabtagene ciloleucel in large B-cell lymphoma. Blood Adv. 2020;4(19):4898-4911.
- Locke FL, Siddiqi T, Jacobson CA, et al. Real-world and clinical trial outcomes in large B-cell lymphoma with axicabtagene ciloleucel across race and ethnicity. Blood. 2024;143(26):2722-2734.
- Loff S, Dietrich J, Meyer JE, et al. Rapidly Switchable Universal CAR-T Cells for Treatment of CD123-Positive Leukemia. Mol Ther Oncolytics. 2020;17:408-420.
- Mackensen A, Haanen JBAG, Koenecke C, et al. CLDN6-specific CAR-T cells plus amplifying RNA vaccine in relapsed or refractory solid tumors: the phase 1 BNT211-01 trial. Nat Med. 2023;29(11):2844-2853.

- Marchisio M, Simeone P, Bologna G, et al. Flow Cytometry Analysis of Circulating Extracellular Vesicle Subtypes from Fresh Peripheral Blood Samples. Int J Mol Sci. 2020;22(1):48.
- Marhelava K, Fidyt K, Pepek M, et al. LILRB1-directed CAR-T cells for the treatment of hematological malignancies. Leukemia. 2025;39(6):1395-1411.
- Matsui, T. and Yoshida, Y. (2020), Reduced perforin release from T cells as a mechanism underlying hypothermia-mediated neuroprotection. Clin Exp Neuroimmunol, 11: 57-64.
- Maude SL, Laetsch TW, Buechner J, et al. Tisagenlecleucel in Children and Young Adults with B-Cell Lymphoblastic Leukemia. N Engl J Med. 2018;378(5):439-448.
- Messelodi D, Bertuccio SN, Indio V, et al. iPSC-Derived Gaucher Macrophages Display Growth Impairment and Activation of Inflammation-Related Cell Death. Cells. 2021;10(11):2822.
- Messelodi D, Strocchi S, Bertuccio SN, et al. Neuronopathic Gaucher disease models reveal defects in cell growth promoted by Hippo pathway activation. Commun Biol. 2023;6(1):431.
- Möller A, Lobb RJ. The evolving translational potential of small extracellular vesicles in cancer. *Nat Rev Cancer*. 2020;20(12):697-709.
- Morris EC, Neelapu SS, Giavridis T, Sadelain M. Cytokine release syndrome and associated neurotoxicity in cancer immunotherapy. Nat Rev Immunol. 2022;22(2):85-96.
- Morschhauser F, Dahiya S, Palomba ML, et al. Lisocabtagene maraleucel in follicular lymphoma: the phase 2 TRANSCEND FL study. Nat Med. 2024;30(8):2199-2207.

- Mueller KT, Maude SL, Porter DL, et al. Cellular kinetics of CTL019 in relapsed/refractory B-cell acute lymphoblastic leukemia and chronic lymphocytic leukemia. Blood. 2017;130(21):2317-2325.
- Mustapic M, Eitan E, Werner JK Jr, et al. Plasma Extracellular Vesicles Enriched for Neuronal Origin: A Potential Window into Brain Pathologic Processes. Front Neurosci. 2017;11:278.
- Möller A, Lobb RJ. The evolving translational potential of small extracellular vesicles in cancer. Nat Rev Cancer. 2020;20(12):697-709.
- Neelapu SS, Chavez JC, Sehgal AR, et al. Three-year follow-up analysis of axicabtagene ciloleucel in relapsed/refractory indolent non-Hodgkin lymphoma (ZUMA-5). Blood. 2024;143(6):496-506.
- Neelapu SS, Jacobson CA, Ghobadi A, et al. Five-year follow-up of ZUMA-1 supports the curative potential of axicabtagene ciloleucel in refractory large B-cell lymphoma. Blood. 2023;141(19):2307-2315.
- Neelapu SS, Locke FL, Bartlett NL, et al. Axicabtagene Ciloleucel CAR T-Cell Therapy in Refractory Large B-Cell Lymphoma. N Engl J Med. 2017;377(26):2531-2544.
- Neelapu SS. CAR-T efficacy: is conditioning the key?. Blood. 2019;133(17):1799-1800.
- Pensato U, Amore G, Muccioli L, et al. CAR t-cell therapy in BOlogNa-NEUrotoxicity TReatment and Assessment in Lymphoma (CARBON-NEUTRAL): proposed protocol and results from an Italian study. J Neurol. 2023;270(5):2659-2673.
- Perez MD, Seu L, Lowman KE, et al. The tetraspanin CD151 marks a unique population of activated human T cells. Sci Rep. 2020;10(1):15748.

- Pesce E, Manfrini N, Cordiglieri C, et al. Exosomes Recovered From the Plasma of COVID-19 Patients Expose SARS-CoV-2 Spike-Derived Fragments and Contribute to the Adaptive Immune Response. Front Immunol. 2022;12:785941.
- Ramos CA, Savoldo B, Torrano V, et al. Clinical responses with T lymphocytes targeting malignancy-associated κ light chains. J Clin Invest. 2016;126(7):2588-2596.
- Reinhardt P, Glatza M, Hemmer K, et al. Derivation and expansion using only small molecules of human neural progenitors for neurodegenerative disease modeling. PLoS One. 2013;8(3):e59252.
- Rejeski K, Jain MD, Shah NN, Perales MA, Subklewe M. Immune effector cell-associated haematotoxicity after CAR T-cell therapy: from mechanism to management. Lancet Haematol. 2024;11(6):e459-e470.
- Rejeski K, Subklewe M, Aljurf M, et al. Immune effector cell-associated hematotoxicity: EHA/EBMT consensus grading and best practice recommendations. Blood. 2023;142(10):865-877.
- Riccio M, Dembic M, Cinti C, Santi S. Multifluorescence labeling and colocalization analyses. Methods Mol Biol. 2004;285:171-177.
- Ruella M, Korell F, Porazzi P, Maus MV. Mechanisms of resistance to chimeric antigen receptor-T cells in haematological malignancies. Nat Rev Drug Discov. 2023;22(12):976-995.
- Rurik JG, Tombácz I, Yadegari A, et al. CAR T cells produced in vivo to treat cardiac injury. Science. 2022;375(6576):91-96.
- Sadelain M, Rivière I, Riddell S. Therapeutic T cell engineering. Nature. 2017;545(7655):423-431.

- Santomasso BD, Nastoupil LJ, Adkins S, et al. Management of Immune-Related Adverse Events in Patients Treated With Chimeric Antigen Receptor T-Cell Therapy: ASCO Guideline. J Clin Oncol. 2021;39(35):3978-3992.
- Santomasso BD, Park JH, Salloum D, et al. Clinical and Biological Correlates of Neurotoxicity Associated with CAR T-cell Therapy in Patients with B-cell Acute Lymphoblastic Leukemia. Cancer Discov. 2018;8(8):958-971.
- Schumacher TN, Scheper W, Kvistborg P. Cancer Neoantigens. Annu Rev Immunol. 2019;37:173-200.
- Schumacher TN, Schreiber RD. Neoantigens in cancer immunotherapy. Science. 2015;348(6230):69-74.
- Schuster SJ, Bishop MR, Tam CS, et al. Tisagenlecleucel in Adult Relapsed or Refractory Diffuse Large B-Cell Lymphoma. N Engl J Med. 2019;380(1):45-56.
- Schuster SJ, Tam CS, Borchmann P, et al. Long-term clinical outcomes of tisagenlecleucel in patients with relapsed or refractory aggressive B-cell lymphomas (JULIET): a multicentre, open-label, single-arm, phase 2 study. Lancet Oncol. 2021;22(10):1403-1415.
- Shah NN, Johnson BD, Schneider D, et al. Bispecific anti-CD20, anti-CD19 CAR T cells for relapsed B cell malignancies: a phase 1 dose escalation and expansion trial. Nat Med. 2020;26(10):1569-1575.
- Siegler EL, Kenderian SS. Neurotoxicity and Cytokine Release Syndrome After Chimeric Antigen Receptor T Cell Therapy: Insights Into Mechanisms and Novel Therapies. Front Immunol. 2020;11:1973.
- Spiegel JY, Patel S, Muffly L, et al. CAR T cells with dual targeting of CD19 and CD22 in adult patients with recurrent or refractory B cell malignancies: a phase 1 trial. Nat Med. 2021;27(8):1419-1431.

- Storci G, Barbato F, Ricci F, et al. Pre-transplant CD69+ extracellular vesicles are negatively correlated with active ATLG serum levels and associate with the onset of GVHD in allogeneic HSCT patients. Front Immunol. 2023;13:1058739.
- Strati P, Nastoupil LJ, Westin J, et al. Clinical and radiologic correlates of neurotoxicity after axicabtagene ciloleucel in large B-cell lymphoma. Blood Adv. 2020;4(16):3943-3951.
- Théry C, Ostrowski M, Segura E. Membrane vesicles as conveyors of immune responses. Nat Rev Immunol. 2009;9(8):581-593.
- Topp MS, van Meerten T, Houot R, et al. Earlier corticosteroid use for adverse event management in patients receiving axicabtagene ciloleucel for large B-cell lymphoma. Br J Haematol. 2021;195(3):388-398.
- Turtle CJ, Hanafi LA, Berger C, et al. Immunotherapy of non-Hodgkin's lymphoma with a defined ratio of CD8+ and CD4+ CD19-specific chimeric antigen receptor-modified T cells. Sci Transl Med. 2016;8(355):355ra116.
- Velasco R, Mussetti A, Villagrán-García M, Sureda A. CAR T-cell-associated neurotoxicity in central nervous system hematologic disease: Is it still a concern?. Front Neurol. 2023;14:1144414.
- Vignoli B, Sansevero G, Sasi M, et al. Astrocytic microdomains from mouse cortex gain molecular control over long-term information storage and memory retention. Commun Biol. 2021;4(1):1152.
- Wang M, Munoz J, Goy A, et al. KTE-X19 CAR T-Cell Therapy in Relapsed or Refractory Mantle-Cell Lymphoma. N Engl J Med. 2020;382(14):1331-1342.
- Wang M, Munoz J, Goy A, et al. Three-Year Follow-Up of KTE-X19 in Patients With Relapsed/Refractory Mantle Cell Lymphoma, Including High-Risk Subgroups, in the ZUMA-2 Study. J Clin Oncol. 2023;41(3):555-567.

- Wang Z, Li P, Zeng X, et al. CAR-T therapy dilemma and innovative design strategies for next generation. Cell Death Dis. 2025;16(1):211.
- Westin JR, Oluwole OO, Kersten MJ, et al. Survival with Axicabtagene Ciloleucel in Large B-Cell Lymphoma. N Engl J Med. 2023;389(2):148-157.
- Wudhikarn K, Pennisi M, Garcia-Recio M, et al. DLBCL patients treated with CD19 CAR T cells experience a high burden of organ toxicities but low nonrelapse mortality. Blood Adv. 2020;4(13):3024-3033.
- Xu Y, Zhang M, Ramos CA, et al. Closely related T-memory stem cells correlate with in vivo expansion of CAR.CD19-T cells and are preserved by IL-7 and IL-15. Blood. 2014;123(24):3750-3759.
- Zander R, Schauder D, Xin G, et al. CD4+ T Cell Help Is Required for the Formation of a Cytolytic CD8+ T Cell Subset that Protects against Chronic Infection and Cancer. Immunity. 2019;51(6):1028-1042.e4.
- Zhang Q, Jeppesen DK, Higginbotham JN, et al. Supermeres are functional extracellular nanoparticles replete with disease biomarkers and therapeutic targets. Nat Cell Biol. 2021;23(12):1240-1254.
- Zurko JC, Johnson BD, Aschenbrenner E, et al. Use of Early Intrathecal Therapy to Manage High-Grade Immune Effector Cell-Associated Neurotoxicity Syndrome. JAMA Oncol. 2022;8(5):773-775